Superconductivity and Fermi surface of Tl:PbTe

Supraleitung und Fermifläche von Tl:PbTe
Supraconductivité et Surface de Fermi de Tl:PbTe

Master-Thesis von Lisa Franziska Buchauer aus Offenbach am Main
September 2014

TECHNISCHE
UNIVERSITÄT
DARMSTADT

Superconductivity and Fermi surface of Tl:PbTe
Supraleitung und Fermifläche von Tl:PbTe
Supraconductivité et Surface de Fermi de Tl:PbTe

Vorgelegte Master-Thesis von Lisa Franziska Buchauer aus Offenbach am Main

1. Gutachten: Dr. Kamran Behnia, Directeur de Recherche
2. Gutachten: Prof. Dr. Rudolf Feile

Tag der Einreichung:

Abstract

Lead telluride (PbTe) is a narrow-gap semiconductor which exhibits metallic character and a clear Fermi surface even in the absence of controlled doping. The Fermi surface of p-type PbTe for carrier concentrations p below 10^{19} holes per cm^3 is known to consist of four ellipsoidal pockets at the L-points of the fcc-Brillouin zone. Furthermore, upon doping with thallium (Tl) PbTe becomes a superconductor above a critical carrier concentration of $p = 5 \cdot 10^{19}\,cm^{-3}$, corresponding to a critical doping-level of $x_{Tl} \approx 0.4\%$.
In this work, the evolution of the Fermi surface of Tl-doped PbTe for $p > 10^{19}\,cm^{-3}$ was explored in order to look for a possible link between emerging superconductivity and a change in Fermi surface topology. Paying particular attention to the critical doping range around $x_{Tl} = 0.4\%$, a series of seven samples with carrier concentrations between $1.5 \cdot 10^{19}\,cm^{-3}$ and $9 \cdot 10^{19}\,cm^{-3}$ was analysed using the Shubnikov - de Haas effect (quantum oscillations in resistivity) as a probe.
Evidence was found that the emergence of a superconducting ground state at a critical carrier concentration is concomitant with the observation of an additional oscillation frequency which we attribute to a new set of twelve ellipsoidal Fermi surface pockets at the Σ-points of the Brillouin-zone with the help of theory. This has implications for the mechanism of superconductivity in Tl:PbTe.

Bleitellurid (PbTe) ist ein Halbleiter mit schmaler Bandlücke, der selbst in Abwesenheit von Fremddotierung metallischen Charakter und eine klar definierte Fermifläche aufweist. Diese besteht im p-dotierten Fall für Ladungsträgerdichten bis $p = 10^{19}\,cm^{-3}$ aus vier ellipsoidförmigen Taschen an den L-Punkten der fcc-Brillouin-Zone. Des Weiteren wird das Material zum Supraleiter, wenn es mit Thallium (Tl) zu Ladungsträgerdichten oberhalb eines kritischen Werts von $p = 5 \cdot 10^{19}\,cm^{-3}$ dotiert wird, was einer kritischen Dotierung von $x_{Tl} \approx 0.4\%$ entspricht.
In dieser Arbeit wurde die Evolution der Fermifläche von Tl-dotiertem PbTe für $p > 10^{19}\,cm^{-3}$ untersucht, um einen möglichen Zusammenhang zwischen dem Auftauchen des supraleitenden Grundzustandes und einer Veränderung der Topologie der Fermifläche zu erforschen. Eine Reihe von sieben Proben mit Ladungsträgerdichten zwischen $1.5 \cdot 10^{19}\,cm^{-3}$ und $9 \cdot 10^{19}\,cm^{-3}$ wurde mit Hilfe des Shubnikov - de Haas-Effektes (Quantenoszillationen des spezifischen Widerstands) analysiert, wobei dem Bereich der kritischen Dotierung um $x_{Tl} = 0.4\%$ besondere Aufmerksamkeit zukam.
Hierbei wurden Indizien für das simultane Auftreten eines supraleitenden Grundzustandes und einer zusätzlichen Oszillationsfrequenz, welche wir mit theoretischer Hilfe einem neuen Satz von zwölf Fermiflächen-Taschen an den Σ-Punkten der Brillouin-Zone zuordnen, bei derselben kritischen Ladungsträgerdichte entdeckt. Dies hat Konsequenzen für den supraleitenden Mechanismus in Tl:PbTe.

Le tellurure de plomb (PbTe) est un semiconducteur à petit gap qui est de charactère métallique avec une surface de Fermi clairement définie même en l'absence d'un dopage contrôlé. Celle-ci est constituée de quatre poches ellipsoïdales aux points L de la zone de Brillouin de la maille cfc dans le cas du dopage de type p pour des concentrations de porteurs inférieures à $p = 10^{19}\,cm^{-3}$. En outre, le matériau devient un supraconducteur quand il est dopé au thallium (Tl). L'apparition de la supraconductivité nécessite un nombre critique de porteurs de $p = 5 \cdot 10^{19}\,cm^{-3}$ qui correspond à un dopage critique de $x_{Tl} \approx 0.4\%$.
Dans ce travail l'évolution de la surface de Fermi de PbTe dopé au Tl pour $p > 10^{19}\,cm^{-3}$ a été analysée afin d'explorer un lien possible entre l'apparition d'un état supraconducteur et un changement de la topologie de la surface de Fermi. Une série de sept échantillons avec des densités de porteurs entre $1.5 \cdot 10^{19}\,cm^{-3}$ et $9 \cdot 10^{19}\,cm^{-3}$ a été étudiée en utilisant l'effet Shubnikov - de Haas (oscillations quantiques de la résistivité). Une attention particulière a été accordé à la gamme de dopage autour du niveau critique $x_{Tl} = 0.4\%$.
Des indices de l'apparition simultanée d'un état de base supraconducteur et d'une nouvelle fréquence d'oscillations quantiques au même dopage critique ont été découverts. Avec l'aide de la théorie, ces fréquences sont attribuées à un set de douze poches ellipsoïdales aux points Σ de la zone de Brillouin. Cela nous renseigne sur le mécanisme supraconducteur dans Tl:PbTe.

Contents

1 Motivation

Superconductivity has lost nothing of the fascination it exerted when first discovered in 1911 by Heike Kamerlingh Onnes: a mercury wire, cooled below 4.1 K, lost all measurable electrical resistance and current began to flow without dissipation [1]. Interest in the community was awoken and within a few years following the initial discovery, this extremely high conductivity - "superconductivity" as it was baptised by Onnes - was observed in several other pure metals such as tin, lead [2], tantalum, thorium and niobium [3] as well. Following these findings in pure systems, research ventured further into the area of alloys and compounds and in 1929 a solution of 4% bismuth in gold [4] and copper sulfide [5] were found to be superconductors even though none of the ingredients of either of the two systems shows the behaviour itself. In 1933, Walther Meißner and Robert Ochsenfeld discovered that during a superconducting transition all magnetic flux is expulsed from the substance. This leads to the widely known phenomenon that this sample, when placed on a ferromagnetic surface at room temperature, will take off and start to levitate once cooled below the critical temperature, similar to what is shown in figure 1.1. It was puzzling properties like these that fuelled research activities on both experimental and theoretical side during the decades following Onnes' discovery, and it was as a theoretical response to the Meissner effect that the first successful phenomenological description of superconductivity was derived by the London brothers in 1935 [6] and improved and extended by soviet physicists Vitaly Ginzburg, Lev Landau and Alekseï Abrikosov [7]. What happens on a microscopic scale upon the phase transition between normal and superconducting states remained unexplained until the 1950s, when Leon Neil Cooper had the ground-breaking idea of electrons traveling through the superconductor in pairs as opposed to independent electrons in the normal state. Together with John Bardeen and John Robert Schrieffer he developed this into the very successful BCS-Theory.

As theoretical understanding improved and the list of known superconducting materials became longer, applied research interest in dissipation-free electrical transport and related phenomena grew. As a result, SQUIDs (superconducting quantum interference devices) and superconducting magnet coils - to name two examples - are widely used in science today. The former make use of Josephson junctions which consist of two superconductors separated by a thin normal-conducting or insulating layer and allow for the measurement extremely low magnetic fields which are of interest for example in neuroscience. The development of the latter gave scientists the opportunity to make use of higher magnetic fields on larger experimental scales, prominently employed today in solid state and

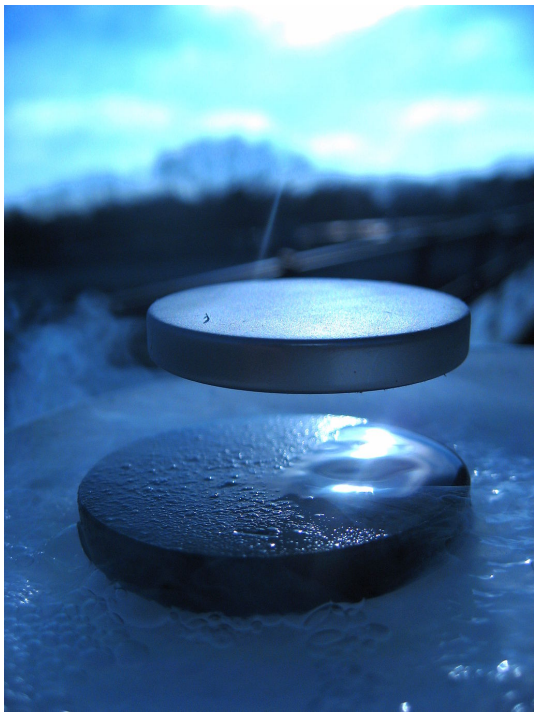

Figure 1.1.: A magnet levitating above a YBCO substrate at liquid nitrogen temperature [8].

particle physics. On the road to superconducting magnets a major obstacle had to be overcome - even though they were proposed in the early days of the field, again by Onnes [9], it was not until 1954 that the first superconducting coil was constructed [10], producing a field of 0.7 T. This delay occurred because most superconductors discovered in the early years were of type I, and comparatively small magnetic fields of magnitudes below 1 T are sufficient to destroy the resistance-free state. With the discovery of type II superconductors that partly allow magnetic flux to pass through, this critical magnetic field could be raised significantly and reaches the order of several tens of Tesla in some high-temperature superconductors. One of the most important civil uses of superconductivity today is found in medicine, where superconducting coils provide the magnetic fields needed for nuclear magnetic resonance spectroscopy. As these examples show, most of the applications of superconductivity in use at present are confined to the laboratory or clinical environment because the superconducting state of the materials used can only be reached at very low temperatures and liquid helium is needed to bring it about. This makes the devices difficult to handle and produces high operating costs.

By 1973, the highest known critical temperature for superconductivity (T_c) had reached 22 K in Nb_3Ge [11], still far away from the next landmark in temperature hierarchy: the boiling point of nitrogen at 77 K. Any ideas of making superconducting wires available for large grid applications in electrical transport were hence far from reality. Then, a major breakthrough occurred in 1986 when Georg Bednorz and Alexander Müller discovered the first superconductor with a critical temperature above 30 K, an oxygen deficient Ba-La-Cu-O-compound [12]. Shortly after, T_c was pushed beyond the nitrogen limit by Y-Ba-Cu-O (YBCO) [13]. The highest transition temperature found as yet is 133 K in Hg-Ba-Ca-Cu-O [14]. These findings have put the discussion of potential applications of a room temperature superconductor back on the agenda. The lossless transport of sustainably produced electricity from places where it is readily available such as sunny deserts or windy shores to urban centres where it is consumed is the best example for this. However, the last advance in T_c is now more than twenty years in the past and satisfactory theoretical description and understanding of high-T_c superconductors is still lacking [15]. Most known high-T_c superconductors are cuprates, but more recently a new family of iron-based superconductors was discovered, albeit with a maximum T_c somewhat lower than those of the cuprates. All of them have in common that phonons are widely suspected no to be the glue of their Cooper pairs and they are hence often called "unconventional" superconductors. The material with the highest critical temperature known where pair formation is believed to be due to phonons is MgB_2 with $T_c = 40$ K [16]. This makes clear that the route via novel types of superconductors, where unconventional pairing mechanisms are involved, is much more likely to lead to the ultimate goal of room temperature superconductivity and that better understanding of its fundamentals is vital.

As the superconducting phase is essentially an instability of the normal phase, a good knowledge of of its electronic structure is desirable when attempting to explain superconductivity. The Fermi surface of such a system in particular should contain clues about superconducting properties such as the existence of a superconducting state, the corresponding critical temperature or possible pairing mechanisms. In general, high-T_c superconductors, like the ones named above, are doped Mott insulators and the calculation of their band structures is beyond most of the common methods of band structure calculation. Because of this theoretical difficulty it remained unknown for some time after the discovery of the first cuprate superconductors whether these had in fact a distinct Fermi service or not. Experimental methods of probing the Fermi surface such as angle-resolved photoemission spectroscopy (ARPES) or quantum oscillation measurements like the ones used in this work encounter difficulties as well. The former has contributed much information about the general distribution of the carriers in **k**-space [17,18] but lacks the power to resolve small pockets and fine structures. The latter, generally better suited for probing small Fermi surface elements, suffers from the low mobility of carriers associated with complicated systems [19]. It was not until 2007 that quantum oscillations were observed in YBCO for the first time, revealing small carrier pockets in the underdoped regime [20]. The general result of these efforts is that the Fermi surfaces of high-T_c superconductors are complicated structures consisting of several electron and hole pockets and sheets of very different sizes, evolving greatly between underdoped and overdoped regimes [21].

However, it is not only in complicated high-T_c systems that the relationship between Fermi surface and superconductivity is poorly understood. As an example, a dependency of T_c on the topology of the Fermi surface has been observed in $SrTiO_3$ where the Fermi surface consists of one, two or three almost spherical electron pockets around the Γ-point depending on carrier number. In order to further explore the relationship between Fermi surface and superconducting properties, suitable model systems that are easily accessible to experiment need to be identified. Candidates are found in the family of IV-VI semiconductors, notably the narrow-gap systems PbTe, SnTe and GeTe.

These combine several advantages related to the quest. Firstly and most importantly, they are known to display a superconducting ground state under certain conditions. Secondly, their Fermi surfaces are fairly well known from both theory and experiment. Band structure calculations using different methods result in vast qualitative (if not quantitative) agreement and are confirmed by experiment, offering a good base for the search for links between Fermi surface and superconductivity. Thirdly, the Fermi surface of these systems can be changed and controlled with relative ease by adding or subtracting carriers thus allowing to follow possibly resulting changes in superconducting properties as a function of Fermi surface evolution.

A superconducting ground state has been observed in self-doped p-type SnTe and GeTe starting from carrier concentrations of about $4 \cdot 10^{20}\,\mathrm{cm}^{-3}$ and $9 \cdot 10^{20}\,\mathrm{cm}^{-3}$ respectively [22, 23]. PbTe cannot be self-doped to carrier concentrations above 10^{19} holes per cm^3 and it appears that this is not high enough to display a superconducting ground state. However, thallium-doped PbTe becomes a superconductor at about $5 \cdot 10^{19}\,\mathrm{cm}^{-3}$.
The Fermi surface of SnTe consists of a single set of small ellipsoidal pockets at lower doping which are joined by a second set of ellipsoids at higher doping. Curiously, the second set of pockets and a finite critical temperature appear around the same carrier concentration in SnTe. In PbTe, the second set of pockets has yet to be established at low temperatures. Probing the relationship between the possible appearance of a second set of Fermi surface components and the onset of superconductivity in Tl:PbTe is one part of this project. A second part is concerned with the fact that Tl is the only dopant to PbTe for which superconductivity has been observed so far. The element is known for appearing in two different valence states in the compounds it forms, which is believed to ultimately give rise to an unconventional non-phononic pairing-mechanism based on real-space interactions.
Overall, this work explores two very different aspects of the superconductivity of Tl-doped PbTe: a possible relationship between Fermi surface topology and superconductivity on one side and the effects of the valence-skipper thallium on the other. Hopes are that a very small piece of evidence can be contributed to the large puzzle showing the roots of superconductivity. This puzzle may ultimately either contain a map to the synthesis of a room-temperature superconductor or else to a sound theory showing that no such things can exist.

Following this motivation of the project, chapter 2 introduces some general concepts relevant to the subject. This includes quantum oscillations as a Fermi surface probe as well as an overview of the basics of superconductivity. Chapter 3 contains useful information more specific to thallium-doped lead telluride - its Fermi surface as currently known and suggestions for its superconducting mechanism. Two other systems are briefly introduced for comparison: STO in the field of Fermi surface and superconductivity and SnTe in the field of valence-fluctuating dopants. After a short review of the experimental methods in chapter 4, all experimental results obtained during this work are presented in chapter 5, the heart of this thesis. New calculations for comparison with the data collected in this project were performed by Alaska Subedi and the results are summarised in chapter 6. Finally, the experimental results are interpreted and possible implications discussed in chapter 7.

2 General Background

This work is about characterising the link between the electronic structure of lead telluride with different carrier concentrations and its superconducting properties. Therefore this chapter will introduce the Shubnikov - de Haas effect as a means to probe the Fermi surface and discuss the phenomenology and some basic theory of superconductivity. The latter is an abridged version of the introduction in [24].

2.1 Probing the Fermi Surface with Quantum Oscillations

In the following, the simple example of a free electron gas is used to recapitulate basics of the electronic structure of metals. Furthermore it is employed to illustrate how quantum oscillations in resistivity as a function of magnetic field come about.

2.1.1 Fermi Surface of a Free Electron Gas

The wavefunction $\Phi(\mathbf{r}_1, \mathbf{r}_2, \ldots, \mathbf{r}_N)$ describing the N conduction electrons at positions $\mathbf{r}_1, \ldots, \mathbf{r}_i, \ldots, \mathbf{r}_N$ in a perfect crystal lattice with static ions is required to fulfil the Schrödinger equation

$$\left(-\sum_i \frac{\hbar^2}{2m_\mathrm{e}} \frac{\partial^2}{\partial \mathbf{r}_i^2} + \sum_i \mathscr{U}(\mathbf{r}_i) + \sum_{i,j} \frac{\mathrm{e}^2}{|\mathbf{r}_i - \mathbf{r}_j|} \right) \Phi(\mathbf{r}_1, \mathbf{r}_2, \ldots, \mathbf{r}_N) = E\Phi(\mathbf{r}_1, \mathbf{r}_2, \ldots, \mathbf{r}_N), \tag{2.1}$$

where the first term on the left describes the kinetic energy of the electrons with mass m_e. The second term accounts for the potential energy of the electrons in the electric field of the ions at lattice positions $\mathbf{l}$: $\mathscr{U} = \sum_\mathbf{l} \mathscr{U}_a(\mathbf{r} - \mathbf{l})$, where $\mathscr{U}_a$ is the contribution of every individual ion. The Coulomb interaction between the electrons produces the third term, where e is the electron charge. Finally, E is the combined energy of the N conduction electrons.
Even though static ions and a perfect lattice are already strong approximations, this equation cannot be solved analytically. The simplest approximation, Sommerfeld's free electron model, omits both the interaction of electrons with the lattice and with each other. In this case, the remaining equation

$$\left(-\sum_i \frac{\hbar^2}{2m_\mathrm{e}} \frac{\partial^2}{\partial \mathbf{r}_i^2} \right) \Phi(\mathbf{r}_1, \mathbf{r}_2, \ldots, \mathbf{r}_N) = E\Phi(\mathbf{r}_1, \mathbf{r}_2, \ldots, \mathbf{r}_N) \tag{2.2}$$

is solved by

$$E = \sum_i \frac{\hbar^2 \mathbf{k}_i^2}{2m_\mathrm{e}} \tag{2.3}$$

and

$$\Phi(\mathbf{r}_1, \mathbf{r}_2, \ldots, \mathbf{r}_N) = \phi_1(\mathbf{r}_1) \cdot \phi_2(\mathbf{r}_2) \cdot \cdots \cdot \phi_N(\mathbf{r}_N), \tag{2.4}$$

where

$$\phi_i(\mathbf{r}_i) = \sqrt{V} \mathrm{e}^{\mathrm{i}\mathbf{k}_i \cdot \mathbf{r}_i}. \tag{2.5}$$

Here, V is the volume of the crystal and $\mathbf{k}_i$ is a vector in three dimensional momentum space. To obtain this solution, periodic boundary conditions were used resulting in allowed $\mathbf{k}$-values of $k_l \in [0, \pm\frac{2\pi}{L_l}, \pm\frac{4\pi}{L_l}, \ldots]$ for $l = x, y, z$, where L_l are the physical dimensions of the crystal (and hence $V = L_x L_y L_z$). This also means that every state occupies a volume of $W = 8\pi^3/V$ in reciprocal space.

Because of the Pauli exclusion principle, two identical fermions are not allowed to occupy the exact same energy state. In other words, their energy states may not be described by concurrent quantum numbers only. Following this principle, in the ground state of a system the N lowest electronic energy states up to a certain energy are filled while the states above are empty. This abstract boundary in reciprocal space, which separates occupied and

unoccupied energy levels, is called the Fermi surface. In the case of a free electron gas with the dispersion relation given in equation (2.3), **k**-space is filled up isotropically from the origin resulting in a spherical Fermi surface, the so-called Fermi sphere.
The simplified discussion of the free electron gas above ignores the fact that electrons also possess either positive or negative spin, and the associated spin quantum number does not appear in equation (2.3). This is why, when placing the N conduction electrons in **k**-space according to this dispersion, an additional factor of 2 accounting for the spin degeneracy of the description has to be introduced:

$$N\frac{8\pi^3}{V} = 2\frac{4\pi}{3}k_F^3, \tag{2.6}$$

where k_F is the radius of the Fermi sphere which houses the N carriers. Combining this with equation (2.3) allows us to calculate the Fermi energy for this particular case:

$$E_F = \frac{\hbar^2}{2m_\mathrm{e}}\left(\frac{3\pi^2 N}{V}\right)^{2/3}. \tag{2.7}$$

If the interactions between lattice and electrons, which were omitted in the Sommerfeld approximation, are allowed for however, the shape of the Fermi surface may deviate significantly from the simple spherical shape or even vanish completely, in which case the material in question is a band insulator. A detailed description of the Fermi surface of pure PbTe is given in chapter 3.1.

The concept of the Fermi surface is crucial for explaining transport properties of solids. Both electric and thermal transport processes involve the transmission of very small energy quantities from one carrier to another. As most of the carriers' **k**-space position is far below the Fermi surface within the Fermi sea, they cannot receive these energy quantities as the energy states that they would need to occupy after the scattering process are already filled. Only states that are very close to the Fermi level can hence participate in transport processes. Because of this intimate relationship between Fermi surface and a variety of physical properties, it is of interest to probe the electronic structure experimentally. One possible method for this is the Shubnikov - de Haas effect.

2.1.2 The Shubnikov - de Haas Effect

Oscillatory structures in physical properties as a function of magnetic field were first observed in 1930 by de Haas and van Alphen in the magnetic susceptibility [25] and by Shubnikov and de Haas in the resistivity [26] of bismuth. A few months before, Landau had published a paper on the diamagnetism of metals in which he had predicted the de Haas - van Alphen effect, but had been sceptical about the chances to observe it experimentally due to sample inhomogeneities [27]. Experiments exploiting both effects went on to be further and further refined and shed light into the fermiology of many systems in the decades following their discovery [28]. The following description of their fundamentals starts out from the free electron gas described in the previous section and continues by applying a magnetic field to this system.

Rearranging equation (2.7) gives the number of states which lie within a sphere defined by an energy E:

$$N(E) = 2\frac{\frac{4}{3}\pi k^3}{\frac{8\pi^3}{V}} = \frac{V}{3\pi^2}\left(\frac{2m_c E}{\hbar^2}\right)^{3/2}. \tag{2.8}$$

From this, the density of states $D(E)$ can be deduced directly using the relation $D(E) = \frac{\mathrm{d}N(E)}{\mathrm{d}E}$, yielding

$$D(E) = \frac{V}{2\pi^2}\left(\frac{2m_c}{\hbar^2}\right)^{3/2} E^{1/2}. \tag{2.9}$$

The situation gets slightly more complicated in an external magnetic field where the equation of motion of an electron can be expressed as follows:

$$\left[\frac{1}{2m_c}\left(\frac{\hbar}{\mathrm{i}}\nabla - \mathrm{e}\mathbf{A}\right)^2\right]\Psi = E\Psi. \tag{2.10}$$

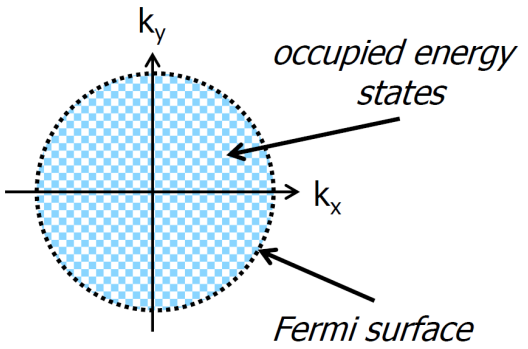

(a) Without magnetic field, the electrons occupy a quasi-continuous energy spectrum.

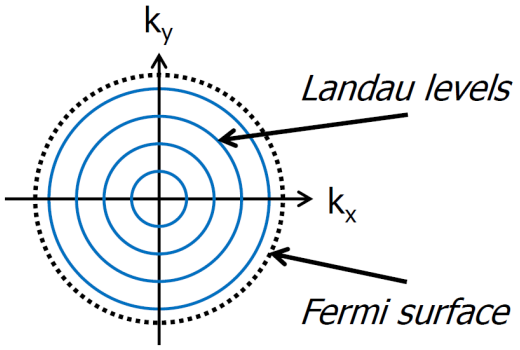

(b) In a magnetic field, the electrons condense on Landau cylinders.

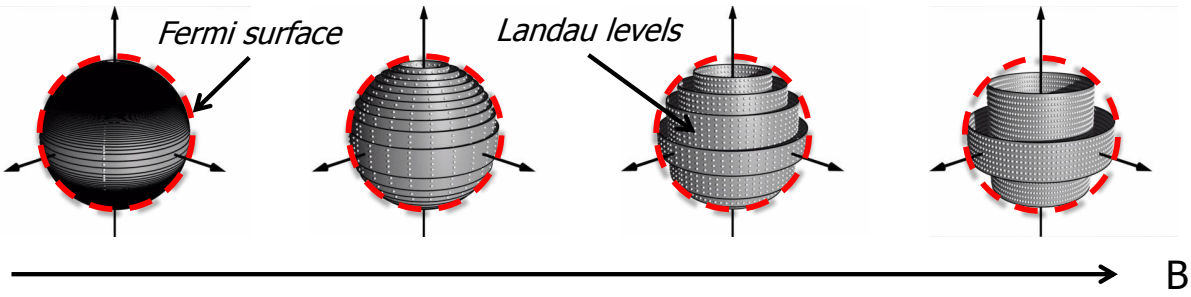

(c) As the magnetic field is increased, the cylinders' radii grow and they pass the Fermi surface one by one. Figures: Benoît Fauqué.

Figure 2.1.: k-space distribution of allowed energy states without and within an external field.

Here, $\mathbf{A}$ is the vector potential of the magnetic field $\mathbf{B} = \nabla \times \mathbf{A}$ which is parallel to the z-axis for the choice $\mathbf{A} = (0, B_y, 0)$, and m_c is the effective mass of the electrons in an applied magnetic field. The ansatz

$$\Psi(\mathbf{r}) = \mathrm{f}(x)\mathrm{e}^{\mathrm{i}(k_y y + k_z z)} \tag{2.11}$$

supplies us with the Schrödinger equation of a one-dimensional harmonic oscillator:

$$-\frac{\hbar^2}{2m_c}\frac{\partial^2 \mathrm{f}(x)}{\partial x^2} + \frac{m_c}{2}\omega_c(x - x_0)\mathrm{f}(x) = \left(E - \frac{\hbar^2 k_z^2}{2m_c}\right)\mathrm{f}(x), \tag{2.12}$$

where the cyclotron frequency $\omega_c = \frac{eB}{m_c}$ has been introduced and $x_0 = \frac{\hbar k_y}{eB}$ is the centre of the oscillating motion. The eigenvalues of this problem were calculated by Landau [27] and are known as Landau levels:

$$E_l = (l + \frac{1}{2})\hbar\omega_c + \frac{\hbar^2 k_z^2}{2m_c}. \tag{2.13}$$

The quantum number l can only assume integer values and is sufficient to describe the movement of the particle in the $k_x k_y$-plane completely.

As equation (2.3) is still valid within an external field for the allowed states, it can be compared to equation (2.13) to find the relation between k_x, k_y and l:

$$k_x^2 + k_y^2 = \left(l + \frac{1}{2}\right)\frac{2m_c\omega_c}{\hbar}. \tag{2.14}$$

This describes the condensation of the states on a cylinder of radius

$$k_l = \sqrt{\left(l + \frac{1}{2}\right) \frac{2m_c\omega_c}{\hbar}}, \tag{2.15}$$

with its axis parallel to the applied field. The difference in energy spectrum between the field-free case and the situation within an external magnetic field is illustrated in figure 2.1. All states that would be lying within the **k**-space between the cylinders for $l-1$ and l collect on the surface of cylinder l. Using the volume of the hollow cylinder between quantum numbers $l-1$ and l to count the number of states that this would contain in the field free case, $N(E)$ and $D(E)$ in an applied field can be calculated in a way similar to equations (2.8) and (2.9). Summing over all cylinders between $l=0$ and $l=l_{max}$ the overall result for the denisty of states is

$$D(E) = \frac{V}{(2\pi)^2}\left(\frac{2m_c}{\hbar^2}\right)^{3/2} \sum_{l=0}^{l_{max}} \frac{\hbar\omega_c}{\left(E - \left(l+\frac{1}{2}\right)\hbar\omega_c\right)^{1/2}}, \tag{2.16}$$

where l_{max} is given by the constraint that the radicand in equation (2.16) must stay positive. The expression for the field-free case, equation (2.9), can be retrieved for the limiting case $B \to 0$ by replacing the sum with an integral. The difference between the density of states for the cases with and without field is illustrated in figure 2.2.

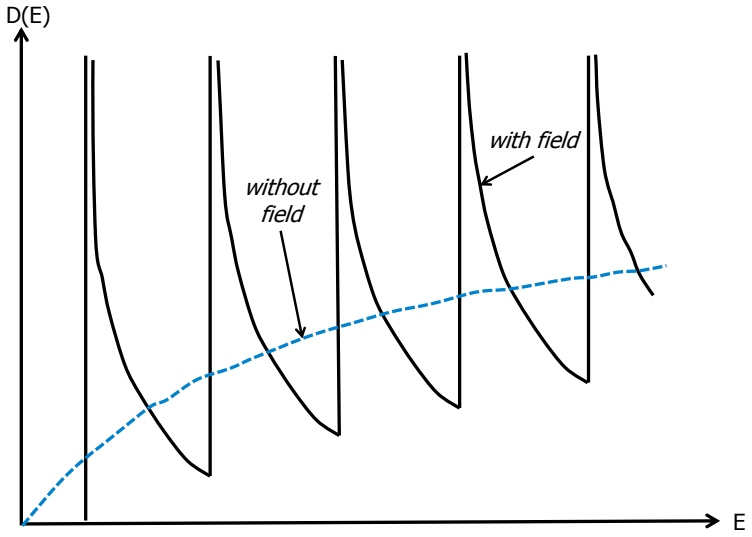

Figure 2.2.: The electronic density of states as a function of energy with and without magnetic field.

Expression (2.16) shows that the density of states diverges every time the condition $E = \left(l+\frac{1}{2}\right)\hbar\omega_c$ is fulfilled. Evaluating this at the Fermi energy E_F shows that the distance between singularities for arbitrary quantum numbers l and $l+1$ is constant on a scale of $1/B$:

$$\Delta(1/B) = \frac{\hbar e}{m_c E_F}. \tag{2.17}$$

The maximum cross section of the Fermi surface perpendicular to the field is $A = k_F^2\pi$, where $k_F^2 = \frac{2m_cE_F}{\hbar^2}$, so the distance between the singularities can be expressed as

$$\frac{1}{F} = \Delta(1/B) = \frac{2\pi e}{\hbar A}, \tag{2.18}$$

Onsager's relation. It shows that the oscillation frequency as a function of inverse field is directly proportional to the cross section area of the Fermi surface perpendicular to the direction of the applied magnetic field. Figure 2.1(c) illustrates how the radius of the individual Landau cylinders grows as the magnetic field is increased and

how they pass the Fermi surface one by one. In real systems of course, the density of states does not diverge at any point as the Landau levels are softened due to scattering processes and thermal broadening. However, as long as the conditions $\hbar\omega_c \gg k_B T$ for the thermal broadening and $\hbar\omega_c \gg \Gamma$ where $\Gamma = \hbar/\tau$ with scattering time τ are met, oscillatory structures can be observed. Here, ω_c is the cyclotron frequency which is related to the carriers effective mass m_c and the magnitude of the applied magnetic field B via $\omega_c = \mathrm{eB}/m_c$. The latter condition expresses the requirement that electrons should be able to travel around the whole cylinder at least a few times before being scattered. Figure 2.3 shows an example of magnetoresistivity data from this work which clearly shows oscillations with a constant period in $1/B$.

Quantum oscillation experiments cannot only be used to probe the form of the Fermi surface in a material, but also to determine the effective mass of the charge carriers in the crystal potential. This is due to the fact that the temperature dependence of the oscillation amplitudes depends on the carrier mass - for heavier carriers, the condition $\hbar\omega_c \gg k_B T$ ceases to be fulfilled faster with increasing temperature.
The complete description of quantum oscillations in physical properties is possible using the Lifshitz-Kosevich formula which is able to account for oscillation frequencies due to different cross sections and their harmonics as well as damping factors that arise from finite temperature, interstate scattering and spin splitting [28]. For the Shubnikov - de Haas effect a symbolic form of the equation looks like this:

$$\rho_{B,\theta} = \rho_{0,B,\theta}\left[1 + \sum_{r,i} C_{r,i} R_{T_{r,i}} R_{D_{r,i}} R_{S_{r,i}} \cos\left(\frac{2\pi F_i r}{B} - \frac{\pi}{4}\right)\right]. \tag{2.19}$$

Here, $\rho_{0,B,\theta}$ is the non-oscillatory background, r indicates the r^{th} harmonic and i counts the different maximum cross sections perpendicular to the field in case the Fermi surface is more complex than a simple sphere. Accordingly, F_i are the different frequencies resulting from these cross sections via equation (2.18). $C_{r,i}$ contains a complicated dependency on field, mass and Fermi energy and determines the amplitude of the oscillations in the ideal case. However, when describing experimental data the oscillations are damped by three processes which are allowed for by the factors R_T, R_D and R_S. R_D describes broadening of the Landau levels due to scattering on defects and R_S is due to spin splitting of each level. R_T results from the temperature dependency at the Fermi level and will be exploited in the following to extract the cyclotronic mass for a given direction of the field. Varying the temperature for a given field direction does not change the oscillation frequency or the position of the peaks, but modifies their amplitude. A measurement of the amplitude of a chosen peak for a series of temperatures can hence be used to fit the reduction factor R_T:

$$R_T = \frac{\pi\lambda}{\sinh(\pi\lambda)}, \ \lambda = \frac{2\pi r k_B T m_c}{Be\hbar}. \tag{2.20}$$

Figure 2.4 illustrates this process. As frequency and amplitude of the oscillations vary with the orientation of the magnetic field relative to the sample for materials with non-spherical Fermi surfaces, repeating this process for different orientations yields different effective masses. This is due to the fact that non-isotropic Fermi surfaces lead to non-isotropic masses that can be described by a tensor. In the case of simple shapes such as ellipsoids, where the general form of the mass tensor is known, its elements can be deduced by measuring the temperature dependence of the oscillations for only a few different angles between sample and magnetic field. Once the mass tensor $\mathscr{M}$ has been determined entirely, the effective mass for arbitrary field directions $\mathbf{h}$ (where $|\mathbf{h}| = 1$) can be calculated [29]:

$$m_c = \sqrt{\frac{\det\mathscr{M}}{\mathbf{h}\cdot\mathscr{M}\cdot\mathbf{h}^{\mathrm{T}}}}. \tag{2.21}$$

2.2 Superconductivity

The normal conductivity of metals is limited by scattering processes of the carriers with phonons, defects and each other. Because these processes happen at all finite temperatures, the electric resistance of a material should be expected to disappear only in perfect crystals and at zero temperature. However, as was first discovered in mercury in 1911, many systems show a jump to zero resistivity at finite temperatures. This property is called superconductivity and gives rise to several curious phenomena such as the Meißner-effect which can make superconductors float

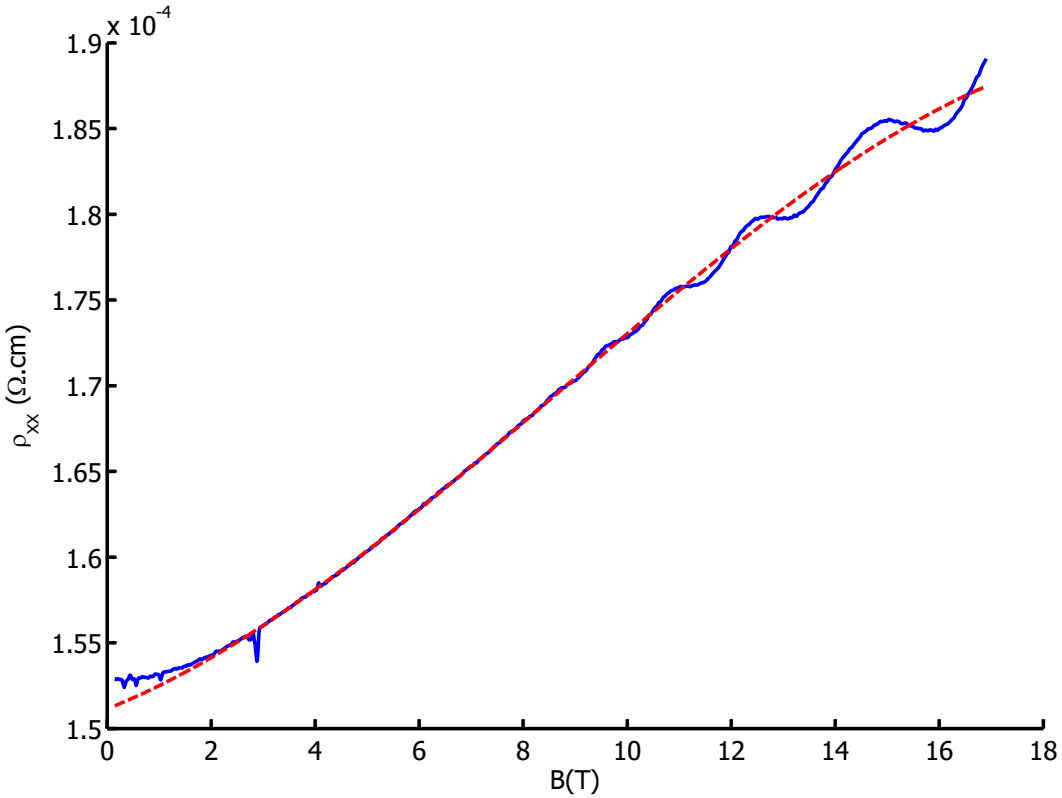

(a) Raw magnetoresistivity data (blue) and polynomial background fitted to this for substraction (red).

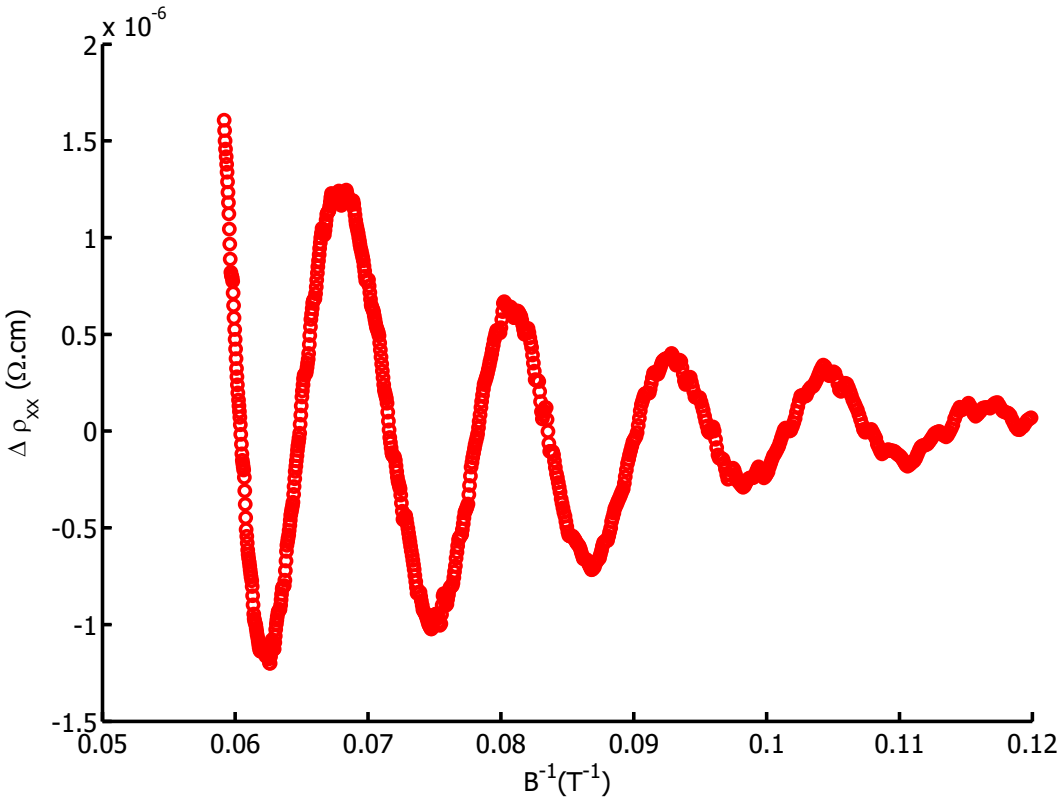

(b) Quantum oscillations after background substraction and inversion of magnetic field.

Figure 2.3.: Resistivity data showing the Shubnikov-de Haas effect, taken within the dilution fridge at 235 mK and for **B** $\parallel [001]$ between -17 and 17 T on a sample with a thallium-content of $x_{\mathrm{Tl}} = 0.3\%$.

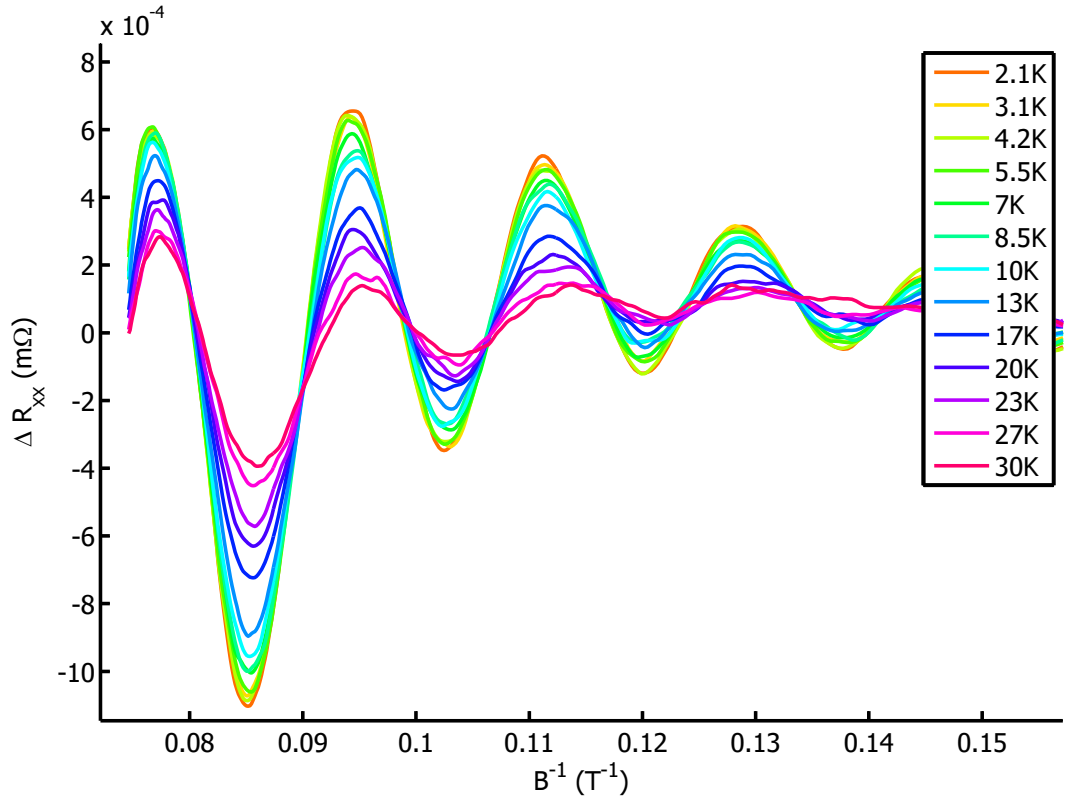

(a) ΔR_{xx} as a function of B^{-1} for T varying between 2.1 K and 30 K and **B** $\parallel [111]$ for $x_{\mathrm{Tl}} = 0.3\%$.

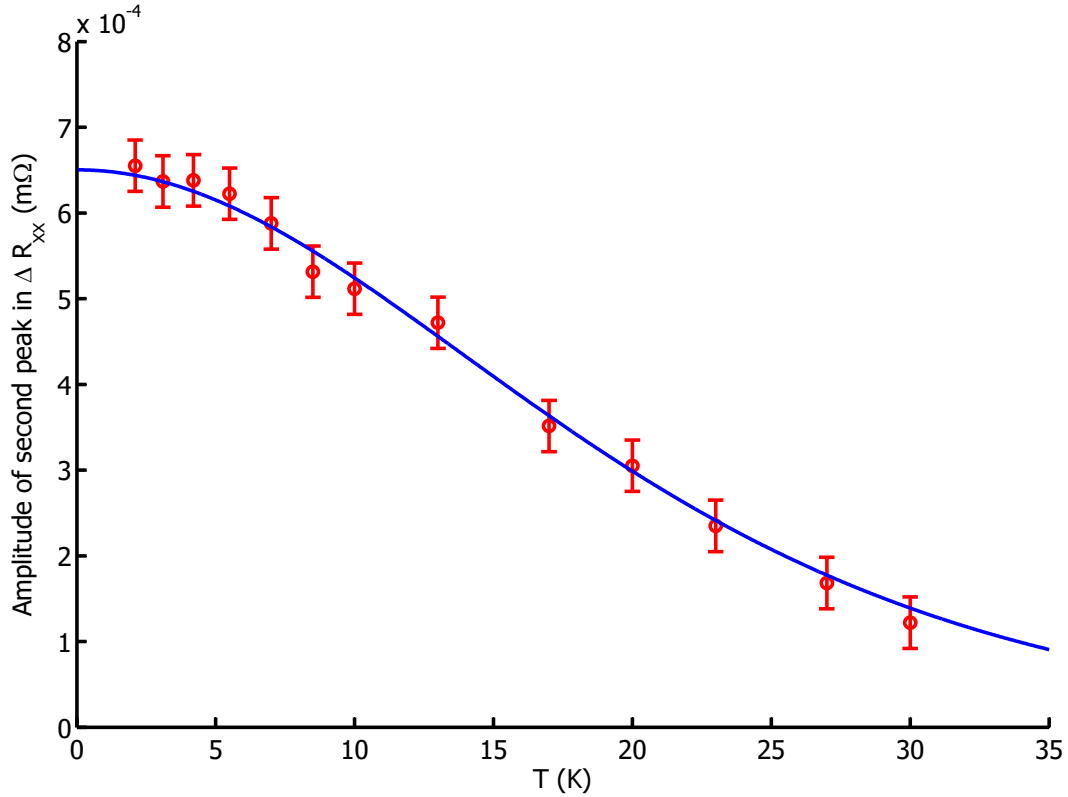

(b) Amplitudes of the quantum oscillations in figure 2.4(a) at $B = 8.8$ T. The line represents a fit of equation (2.20) to the data for $m_c = 0.076\, m_e$.

Figure 2.4.: Procedure for determining the cyclotronic mass.

because of magnetic field expulsion.

In a normal conductor, the spectrum of electron energies is quasi continuous and hence allows for the transfer of arbitrarily small energy amounts between electrons and lattice. This is why scattering processes can happen at all finite temperatures. If this energy spectrum was somehow modified however, for example by introduction of a forbidden energy region (or gap), scattering processes may become suppressed under certain conditions. A mechanism enabling this was first proposed by L. N. Cooper in 1956 and consisted in an attractive interaction between two carriers, binding them into a so-called Cooper pair [30]. If two electrons were introduced into a metal at E_F and bound into a pair, they would be able to sink into the Fermi sea because their collective energy would be lower than $2E_F$.

In 1950 it was observed that the transition temperature between normal and superconducting state of a system depends strongly on the mass of its atoms and therefore on the lattice characteristics: T_c is proportional to the Debye frequency (and hence to the square root of $1/M$ where M is the atomic mass) of the system. This lead to the conclusion that the pair formation must be mediated by the lattice in a way that can be visualised by the following picture: an electron travelling through the positive ions constituting the crystal attracts them slightly and therefore moves them away from their equilibrium position. Because they regain this position on a slower timescale than that of the moving electrons, a second electron can be attracted by the positive trace of the first. As there is a delay between the passing of the first electron at a given point and the ions making this point maximally attractive, the real space distance between the two coupled electrons is around 1000 Å, enough for Coloumb repulsion to be mostly screened. The process is illustrated in figure 2.5. Forming Cooper pairs via phonons is not the only option and is in fact not applicable to some interesting materials. The case of STO at low carrier concentrations is briefly discussed in section 3.2, an exotic suggestion for Tl:PbTe in section 3.3. However, because phonon coupling is the most common case as well as a possible explanation for superconductivity in Tl:PbTe, it will briefly be discussed in the following.

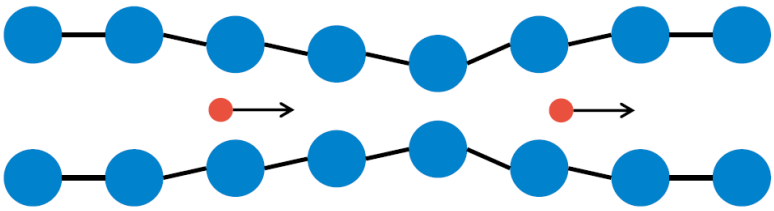

Figure 2.5.: The ionic lattice (blue) coupling two electrons (red) into a pair by means of slowly relaxing deformation.

To describe the process theoretically, virtual phonons $\mathbf{q}$ mediating the attractive interaction between electrons with wave vectors $\mathbf{k}_1, \mathbf{k}_2$ are introduced. After the phonon exchange these electrons possess the wave vectors $\mathbf{k}_1' = \mathbf{k}_1 + \mathbf{q}$ and $\mathbf{k}_2' = \mathbf{k}_2 - \mathbf{q}$, but the overall momentum $\mathbf{K} = \mathbf{k}_1 + \mathbf{k}_2 = \mathbf{k}_1' + \mathbf{k}_2'$ must be conserved. At zero temperature all states below the Fermi level are occupied and only energy levels above E_F are available for electrons. The phononic spectrum of a system is characterised by the Debye frequency ω_D, which quantifies the maximum vibration frequency of the lattice. The maximum energy that can be conveyed by one phonon is therefore $\hbar\omega_D$ and the interaction between electrons of interest is confined to the energy shell between E_F and $E_F + \hbar\omega_D$. This condition together with the conservation of electron momentum mentioned above leads to the conclusion that the probability for two electrons to bind into a pair is largest for $\mathbf{k}_1 = \mathbf{k}_2 \equiv \mathbf{k}$, as is illustrated in figure 2.6.

A linear combination of two plane wave single electron wave functions can serve as an ansatz to describe Cooper pairs with a two-particle wave function $\Psi(\mathbf{r}_1, \mathbf{r}_2)$. Making use of $\mathbf{k}_1 = -\mathbf{k}_2 = \mathbf{k}$ and introducing an amplitude factor A this yields

$$\Psi(\mathbf{k}, \mathbf{r}_1, \mathbf{r}_2) = A\left(\exp(\mathrm{i}\mathbf{k}_1 \cdot \mathbf{r}_1) \cdot \exp(\mathrm{i}\mathbf{k}_2 \cdot \mathbf{r}_2)\right) = A\exp\left[\mathrm{i}\mathbf{k} \cdot (\mathbf{r}_1 - \mathbf{r}_2)\right] = A\exp(\mathrm{i}\mathbf{k} \cdot \mathbf{r}), \tag{2.22}$$

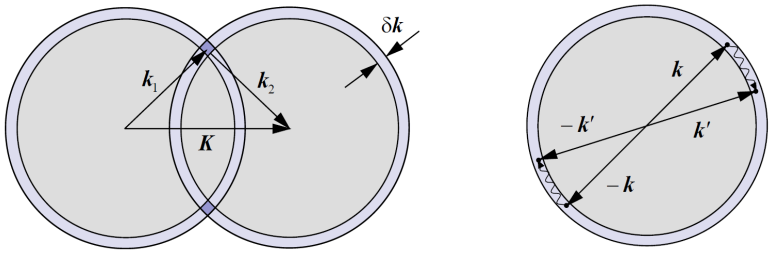

Figure 2.6.: Momentum is conserved only when the wave vectors of the two electrons start (end) in the dark blue area where both momentum shells corresponding to the allowed energies between E_F and $E_F + \hbar\omega_D$ overlap (left). This overlap area is maximised for $\mathbf{k}_1 = -\mathbf{k}_2$ (right). Figures from [24].

where relative real space coordinates where introduced in the last step. Because of scattering processes with the lattice, electrons are constantly transferred into new energy states and Cooper pairs get destroyed and rebuilt. It is thus necessary to modify equation (2.22) by superposing many $\mathbf{k}$-states in order to take scattering into account:

$$\Psi(\mathbf{r}) = \sum_{\mathbf{k}} A_{\mathbf{k}} \exp(\mathrm{i}\mathbf{k}\cdot\mathbf{r}). \tag{2.23}$$

Here, $|A_{\mathbf{k}}|^2$ gives the probability to find the electron pair in the energy state associated with wave vector $\mathbf{k}$. $A_{\mathbf{k}}$ takes non-zero values only for states in the energy shell between E_F and $E_F + \hbar\omega_D$ for $T = 0$. We assume that the energy eigenvalue E of the Cooper pair described by equation (2.23) should be similar to the energies of the two electrons we introduced into the system at the Fermi level, but allow for a possible deviation $\tilde{\Delta}$ from this. To calculate E, the following Schrödinger equation is used:

$$\left[-\frac{\hbar^2}{2\mathrm{m}}(\Delta_1 + \Delta_2) + \tilde{V}(\mathbf{r}_1, \mathbf{r}_2)\right] \Psi(\mathbf{r}_1, \mathbf{r}_2) = E\Psi(\mathbf{r}_1, \mathbf{r}_2) = (2E_F + \tilde{\Delta})\Psi(\mathbf{r}_1, \mathbf{r}_2), \tag{2.24}$$

where Δ_1, Δ_2 are Laplace's operators acting on the first and second electron respectively. The potential $\tilde{V}$ comprises the Coulomb repulsion and the attractive interaction discussed above and its transform in $\mathbf{k}$-space can be approximted by a constant value $\tilde{V}_0$ for $E_F < \hbar^2 k^2/2\mathrm{m} < E_F + \hbar\omega_D$ and set to zero elsewhere. Solving equation (2.24) with these approximations ultimately leads to the result

$$\tilde{\Delta} = E - 2E_F = \frac{2\hbar\omega_D}{1 - \exp\left(4/[\tilde{V}_0 D(E_F)]\right)} \approx -2\hbar\omega_D \exp\left(-4/[\tilde{V}_0 D(E_F)]\right), \tag{2.25}$$

where $D(E_F)$ is the density of electronic states at the Fermi level. This result shows that the energy eigenvalue of a Cooper pair is indeed lower than the sum of the eigenenergies of two separate electrons. It is therefore favourable for two electrons to form a pair at the surface of the Fermi sea.

Up to now the electron spin has been ignored in this discussion, but it plays a major role in the following condensation of all Cooper pairs into a single quantum mechanic energy state. As above, Cooper pairs form between electrons with opposite wave vectors of the same magnitude. A priori, these would be occupying the same energy level, a situation forbidden by the Pauli principle. It is hence necessary that the two electrons within a pair are of opposite spin quantum number, resulting in an overall zero spin, a so-called singlet pair. These pairs are not fermions but bosons to which the Pauli principle no longer applies. This enables the condensation into one energy state mentioned above.

The collective state assumed by the Cooper pairs was first described theoretically by J. Bardeen, L. N. Cooper and J. R. Schrieffer in 1957 [31]. They developed a Hamiltonian that differs from the one describing a gas of free electrons (model system for a simple metal in the normal phase) by an additional term including the attractive

interaction between the members of a pair. In the case of a normal conductor (*nc*), the inner energy of the ground state can be described by

$$W_{0,nc} = 2 \sum_{|k|<k_F} \eta_k, \tag{2.26}$$

where $\eta_k = \hbar^2\mathbf{k}^2/2m - E_F$ is the deviation of each particle's kinetic energy from the Fermi energy. In the BCS description of the superconducting state at zero temperature interaction energy from pair formation is allowed for:

$$W_{0,BCS} = \sum_{\mathbf{k}} 2v_{\mathbf{k}}^2\eta_{\mathbf{k}} - \frac{\tilde{V}_0}{V} \sum_{\mathbf{k}',\mathbf{k}} v_{\mathbf{k}}u_{\mathbf{k}'}u_{\mathbf{k}}v_{\mathbf{k}'}, \tag{2.27}$$

where V is the sample volume. $v_{\mathbf{k}}^2$ and $u_{\mathbf{k}}^2 = 1 - v_{\mathbf{k}}^2$ are the probabilites that the state $(\mathbf{k}\uparrow, -\mathbf{k}\downarrow)$ is occupied or empty respectively. For a scattering process to happen, the initial state $(\mathbf{k}\uparrow, -\mathbf{k}\downarrow)$ must be filled and the final state $(\mathbf{k}'\uparrow, -\mathbf{k}'\downarrow)$ must be empty as expressed by the second term of equation (2.27). Minimising this inner energy eventually yields the dispersion relation for the unpaired carriers in a superconductor:

$$E_{\mathbf{k}} = \sqrt{\eta_{\mathbf{k}}^2 + \tilde{\Delta}^2}. \tag{2.28}$$

$\tilde{\Delta}$ is the superconducting gap as calculated in equation (2.25). The meaning of this gap is clarified by comparing the above dispersion relation with the dispersion relation of the free electron case:

$$E_{\mathbf{k}} = \eta_{\mathbf{k}} + E_F = \frac{\hbar^2\mathbf{k}^2}{2m}. \tag{2.29}$$

In this energy spectrum, even the smallest energies are enough to excite an electron at the Fermi level into an allowed state. On the contrary, in the spectrum given by equation (2.28), there is a minimum energy $\delta E_{min} = 2\tilde{\Delta}$ needed to break up a pair of electrons and form excited quasi-particles. In other words, the energy of excited states is separated from the ground state energy by at least $\tilde{\Delta}$. If this energy is not available to the system because the temperature is low enough, the carriers remain within the macroscopic wave function composed of bosonic pairs and travel through the system without dissipation.

Some modifications need to be applied to the BCS ground state scenario in the case of finite temperatures. For $T > 0$, not all the electrons at the Fermi surface are bound into pairs because thermal excitation can break up some of them and thereby produce quasi-particles that show the conduction properties of a normal state system. These occupy some of the states necessary for the exchange of virtual phonons between the members of a pair and hence lower the interaction energy of the superconducting state. The superconducting gap $\tilde{\Delta}$ shrinks with temperature and disappears completely at the superconducting transition temperature T_c. This boundary condition allows the derivation of a relation between T_c, the interaction potential $\tilde{V}_0$ and the density of pair states at the Fermi level $D_2(E_F)$:

$$k_B T_c = 1.14\hbar\omega_D \exp\left(\frac{-2}{\tilde{V}_0 D_2(E_F)}\right). \tag{2.30}$$

The BCS theory has proven itself very powerful in explaining various features of the superconducting state such as the temperature dependence of the gap, critical magnetic fields, specific heat or thermal conductivity. Various extensions to the original theory allow for the description of more complex systems. From a more applied perspective, one weak point of the theory is that it cannot readily be used for the prediction of new superconducting systems, essentially because it contains a high number of parameters that can only be fixed to a system once some of the superconducting characteristics are known.

While BCS-theory is a microscopic theory of superconductivity, Ginzburg and Landau used Landau's previously developed theory for describing second order phase transitions to explain the superconducting phase transition without knowledge of the microscopic properties. Lev Gor'kov later succeeded in deriving this theory from BCS-theory, relating microscopic parameters and phenomenology. Two important quantities emerge from the equations of Ginzburg-Landau-theory: the coherence length ξ_{GL} and the penetration depth λ_L. The coherence length is a length scale over which the wave function characteristic of a superconductor changes. The penetration depth

characterises the distance to which a magnetic field enters into a superconductor. It also appeared in an earlier description of superconductivity by the London brothers which is why it is often referred to as the London penetration depth. It is given as

$$\lambda_L = \sqrt{\frac{m}{\mu_0 n e^2}}, \tag{2.31}$$

where m is the carriers' mass, n is their density and μ_0 is the magnetic permeability of vacuum.

Up to here it has been assumed that superconductors show ideal diamagnetic behaviour below a critical field B_c above which they lose their superconducting properties. In fact this is only true for so-called type I superconductors - a second type of superconductors, type II, partly allow the penetration of magnetic field at intermediate field strengths while behaving just like type I superconductors at low field. They thus have two critical fields, a lower one, B_{c1}, above which magnetic flux enters the superconductor, and an upper one, B_{c2}, which destroys the superconducting state.

Coherence length and penetration depth can be used to distinguish between type I and type II superconductors. At the interface between a normal conductor and a superconductor, the density of Cooper pairs is reduced and the energy gain per volume through condensation into the superconducting state is lowered as well. Because of this, it is in principle unfavourable for a superconductor to have a large interface with a normal conducting phase. The characteristic length scale on which the condensation energy is reduced can be described by ξ_{GL}. This reduction of the condensation energy due to interfaces is however counteracted by another effect provoked by the mixing of normal and superconducting phases: the expulsion of magnetic field. If a magnetic field is applied to a superconductor, energy is needed to keep this field outside of the sample. Interfaces reduce this energy because they increase the volume fraction in which the magnetic field is allowed to penetrate on the scale of the penetration depth λ_L. In a rough approximation the result of this energy competition is that for superconductors with $\xi_{GL} < \lambda_L$ it is unfavourable to form interfaces with the normal state and hence magnetic flux vortices are expelled from the sample. These are type I superconductors. In contrast to this, type II superconductors gain energy from forming interfaces and hence from allowing magnetic flux to pass through. This is why their phase diagram is more complicated and contains two distinct critical fields. The experimentally accessible upper critical field B_{c2} can be used to calculate ξ_{GL} via the following relation:

$$B_{c2} = \frac{\Phi_0}{2\pi\xi_{GL}^2}, \tag{2.32}$$

where Φ_0 is the magnetic flux quantum.

3 Specific Background: PbTe and Tl:PbTe

In this chapter, research findings more specific to the problem at hand will be introduced. This includes the Fermi surface of PbTe in section 3.1 but also the introduction of an unconventional pairing mechanism associated with Tl-impurities in section 3.3. Two examples are discussed to show how Fermi surface topology and superconductivity may be related: the case of STO in section 3.2 and the case of SnTe in section 3.4. Section 3.3 on negative-U centres partly follows the introduction to the subject given in reference [32].

3.1 Fermi surface of PbTe

Lead telluride is a narrow-gap semiconductor which appears naturally as the mineral altaite. Its crystal structure corresponds to the face-centred cubic structure of NaCl with a lattice constant of a=6.464 Å. Doping with vacancies or third-element dopants results in typical carrier concentrations between 10^{17} and 10^{20} cm^{-3} for both hole and electron doping. Even though the pure material should have a band gap at low temperatures, insulating PbTe has never been found due to anti-site defects: the Tl- and Pb-ions, which are very similar in size as they are direct neighbours in the periodic system of elements, always occupy each others position in the crystal lattice on at least a small fraction of the available sites, thereby introducing carriers into the system. Applied research interest in this material both in past and present has been intense as it exhibits a strong thermoelectric effect and can hence be used to generate electricity from heat. This behaviour has been used in several NASA space missions since the 1960s [33] and continues to attract scientific attention as the search for sustainable energy sources is on the rise. Different dopants have been found to increase the thermoelectric coefficient of PbTe, one of them being thallium [34].

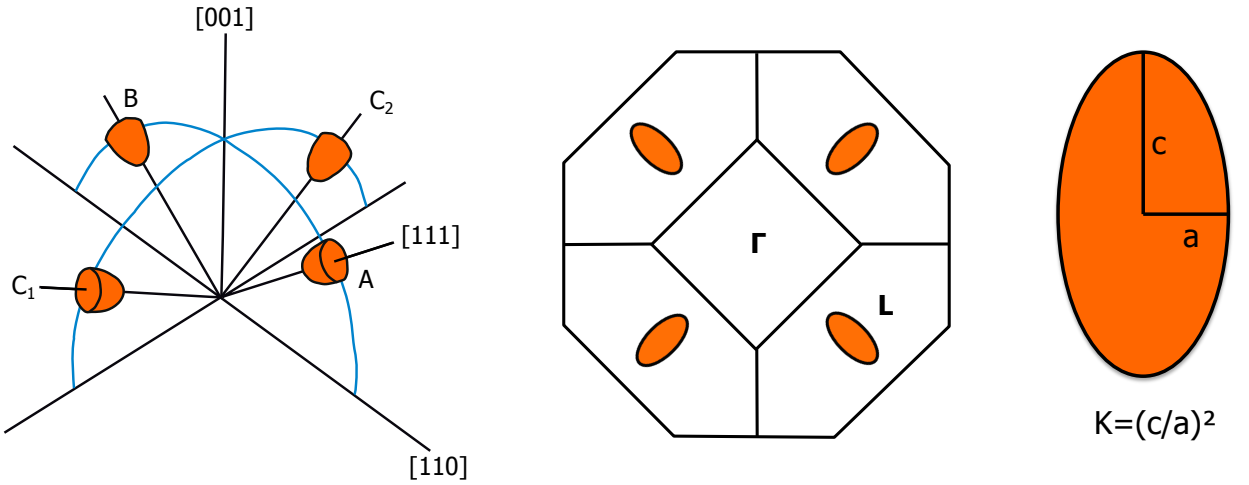

(a) 3D representation of the Fermi surface of PbTe with $p < 10^{19}$ cm^{-3}.

(b) Projection of the fcc Brillouin zone with the ellipsoidal pockets at the L points.

(c) Anisotropy ratio K.

Figure 3.1.: Ellipsoidal Fermi surface of PbTe at low carrier concentrations.

The Fermi surface of p-type PbTe is well studied up to a carrier concentration of 10^{19} holes per cm^3 and it consists of four small ellipsoids at the L-points of the fcc Brillouin zone, as shown in figure 3.1. This picture was established in the sixties with the combined efforts of different experimental methods and theory. The form, position and orientation of the degenerate valleys expected from the cubic symmetry of the system were determined using oscillations in magnetoresistivity (Shubnikv - de Haas (*SdH*) effect) and magnetic susceptibility (de Haas - van Alphen (*dHvA*) effect) as well as other optical and transport phenomena to a lesser extent. Using SdH-measurements, Allgeier [35] found the form of the Fermi surface pockets to be ellipsoidal with the main axis of each ellipsoid oriented along the [111]-direction. This was confirmed by Stiles *et al.* [36] in dHvA-measurements; additionally

they found the position of the structures to be in the centre of the (111)-Brillouin zone faces. The data was used by Dimmock and Wright to develop a model for the band edge structure of the lead salts PbS, PbSe and PbTe using **k·p** perturbation theory [37] which showed reasonable agreement with experiment [38].

Burke *et al.* were the first to apply Fourier analysis to their SdH-data and they were hence able to attain a more precise idea of the ellipsoids and their anisotropy than previous works [39]. To describe the anisotropy of the **k**-space pockets they introduce the useful parameter K which is the square of the maximum-to-minimum cross section ratio for an ellipsoid as shown in figure 3.1(c). In other terms, $K = \sqrt{c/a}$, where c is the length of the major axis of the spheroid and a the length of each of the two minor axes. For a carrier concentration of $3.0 \cdot 10^{18}\,\mathrm{cm}^{-3}$ they find $K = 13$, a value with which all carriers found by Hall-effect measurements can be accounted for when calculating the carrier density from the **k**-space volume of the ellipsoids.

In 1978 Burke and co-workers presented, as a follow-up, the most comprehensive study of the anisotropy of the Fermi surface pockets to this day [40]. They analysed nine samples of p-type PbTe with carrier concentrations between 0.4 and $45 \cdot 10^{18}\,\mathrm{cm}^{-3}$ and found the value of $K = 13$ to be constant at least up to a carrier concentration of $11 \cdot 10^{18}\,\mathrm{cm}^{-3}$. For their last sample which had a hall carrier density of $45 \cdot 10^{18}\,\mathrm{cm}^{-3}$, the model of 4 ellipsoids with $K = 13$ was not able to account for all carriers, leading them to conclude that the Fermi surface is no longer ellipsoidal at this carrier concentration.

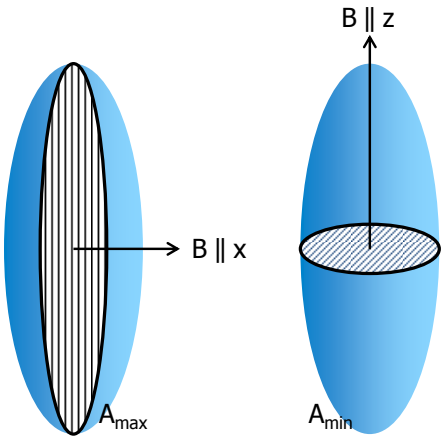

(a) Applying a magnetic field such as to extract minimum and maximum cross sections from the oscillatory data.

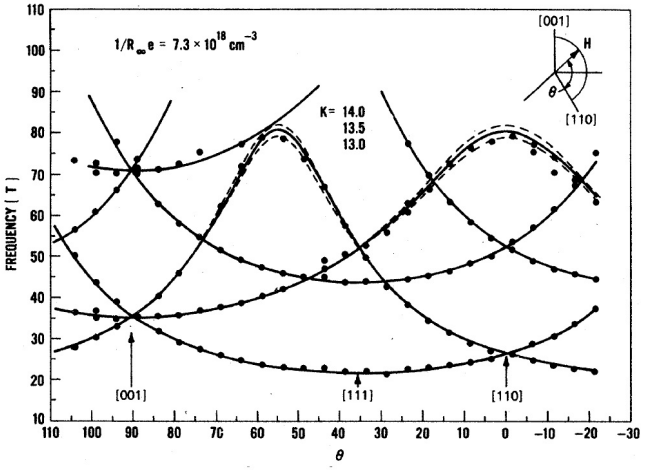

(b) SdH-frequencies as a function of the orientation of the magnetic field in the $(1\bar{1}0)$-plane. Figure from [39].

Figure 3.2.: Using different magnetic field orientations to probe ellipsoidal Fermi surface pockets.

In their studies, Burke *et al.* exploited the fact that the frequency seen in the SdH-effect is proportional to the cross section area perpendicular to the applied magnetic field (as discussed in section 2.1). This means that applying the magnetic field in different directions respective to the sample allows to map the three dimensional Fermi surface elements. In the case of ellipsoids of revolution, it would in principal be enough to measure the frequency for two different angles of the field, as the ellipsoid is completely determined by the lengths of its major and minor axes. Figure 3.2(a) illustrates how the field has to be applied in order to extract minimum and maximum cross section areas of the ellipsoids. Because in PbTe the major axis of the ellipsoids is parallel to the [111]-type directions, both minimum and maximum cross section areas can be probed if the field is turned in a $(1\bar{1}0)$-plane. In this way, the three high symmetry directions [110], [111] and [001] are visited. Burke *et al.* measured oscillation spectra at more than twenty angles in the $(1\bar{1}0)$-plane and Fourier transformed each of them, resulting in the data points shown in figure 3.2(b). The choice of rotation plane means that two of the ellipsoids are degenerate in their frequency signal for every angle. These out-of-plane ellipsoids are labelled with a C in figure 3.1(a), the in-plane ellipsoids with A and B respectively. As, in the general case, the oscillation frequencies of the three types of ellipsoids superpose, Fourier transformation is an essential tool for identifying the contributing cross sections.

For a simple ellipsoidal model the expected oscillation frequencies originating from the three ellipsoid types are readily calculated yielding

$$F(\zeta) = F_{\min}\sqrt{\frac{1}{\cos^2\zeta + K^{-1}\sin^2\zeta}}, \tag{3.1}$$

where $F_{\min}$ is the frequency corresponding to the minimum ellipsoidal cross section and ζ is the angle between the ellipsoid's major axis and the direction of the magnetic field. A more detailed derivation can be found in chapter 5. The anisotropy K can be derived from fitting this type of equation to the data. Burke *et al.* also analysed the masses of the L-pocket carriers and found that the mass corresponding to the minimum cross section of the ellipsoids is between 0.035 and 0.072 electronic masses. An overview over masses extracted with various methods is given in reference [41] and confirms the low L-mass found by Burke.

Older [42] as well as more recent [43] band structure calculations suggest that the next band filling with increasing Fermi energy would occur at the Σ-points of the Brillouin zone thus adding a second set of twelve pockets to the first set of four. Sitter *et al.* who first suggested the Fermi surface shown in figure 3.3(a) with L- and Σ-pockets found evidence using warm hole magnetoresistance between 77 and 400 K [44]. As they point out, the band structure of PbTe changes considerably with temperature, the L-band moving downwards in energy with increasing temperature while the Σ-band moves up. This eventually leads to a band inversion between 400 and 500 K. Due to this strong temperature dependency the application of Sitter's Fermi surface model at low temperature, especially when trying to explain the emergence of superconductivity at temperatures below 2 K, is debatable. In the literature no evidence for a second component has been found in low temperature SdH-experiments, but it is possible that the carrier concentrations of the samples analysed by Burke and others around the same time were not yet high enough to show this feature. However, a study on 0.5%Tl:PbTe with a Hall carrier concentration of about $60 \cdot 10^{18}\,\mathrm{cm}^{-3}$ using high-resolution angle-resolved photoemission spectroscopy (ARPES) at 20 K only showed the L-pockets as well [45]. The mass of the Σ-carriers was determined at higher temperatures by several methods such as temperature-dependent measurements of the Hall coefficient [46] and electric susceptibility [47] and found to lie around one electronic mass, hence above that of the L-carriers. However, if Σ-carriers do exist at low temperatures, this value does probably not apply because of the aforementioned change of the band structure with temperature which is expected to have strong effects on the mass.

Singh calculated the constant energy surfaces of PbTe 0.25 eV below the band edge and found a system of tubes connecting the L-points much like the edges of a cube [43], shown in figure 3.3(b). This Fermi energy most likely corresponds to a doping level that is difficult to obtain in real PbTe systems, but the picture nevertheless brings up the question of how the Fermi surface evolves from the low carrier concentration limit of four separate ellipsoids into the tube system and whether the scenario with L- and Σ-pockets is part of this evolution even at low temperatures.

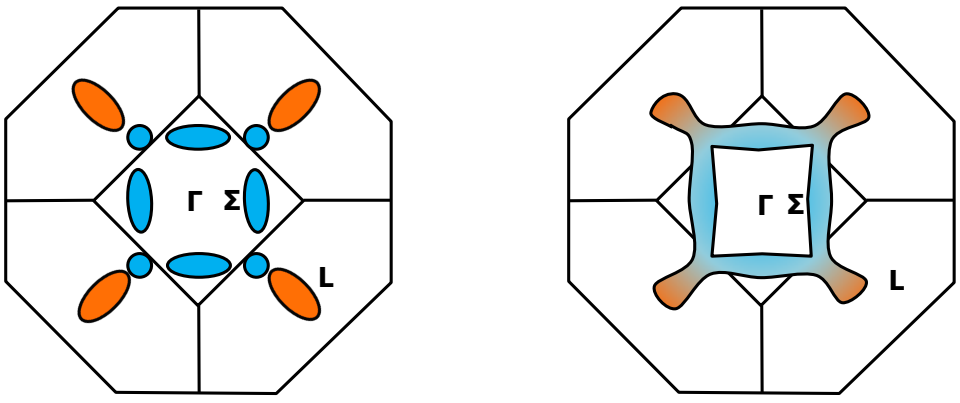

(a) L-pockets (orange) and Σ-pockets (blue) in the Brillouin zone projection.

(b) Tube system with connected L- and Σ-points in the Brioullin zone projection.

Figure 3.3.: Suggested Fermi surfaces for PbTe at higher doping levels.

3.2 Dilute Superconductivity

The system in which superconductivity was first observed in 1911 by Heike Kamerlingh Onnes [1] was mercury. It has an electron concentration of some 10^{22} cm^{-3}, a value typical for simple metals. This value is about three orders of magnitude higher than the carrier density at which Tl:PbTe becomes superconducting. In a naïve approach, one would expect materials with higher carrier concentrations to be better superconductors, as there are more carriers available to form pairs, and the transition temperature into the superconducting state T_c to rise with electron number as well for similar reasons. However, as figure 3.4 shows, even though carrier density and transition temperature are positively correlated in general, there are several peculiarities, such as superconducting domes within some materials, where T_c rises with carrier concentration at first, but then starts to decrease as more carriers are added. Also, the transition temperature for different systems with the same carrier concentration may vary over several orders of magnitude. While this is already interesting when completely different systems are compared, it becomes even more fascinating when the identity of the dopant to one particular system is able to change T_c by two orders of magnitude, as it is the case in SnTe (see section 3.3 for more information).

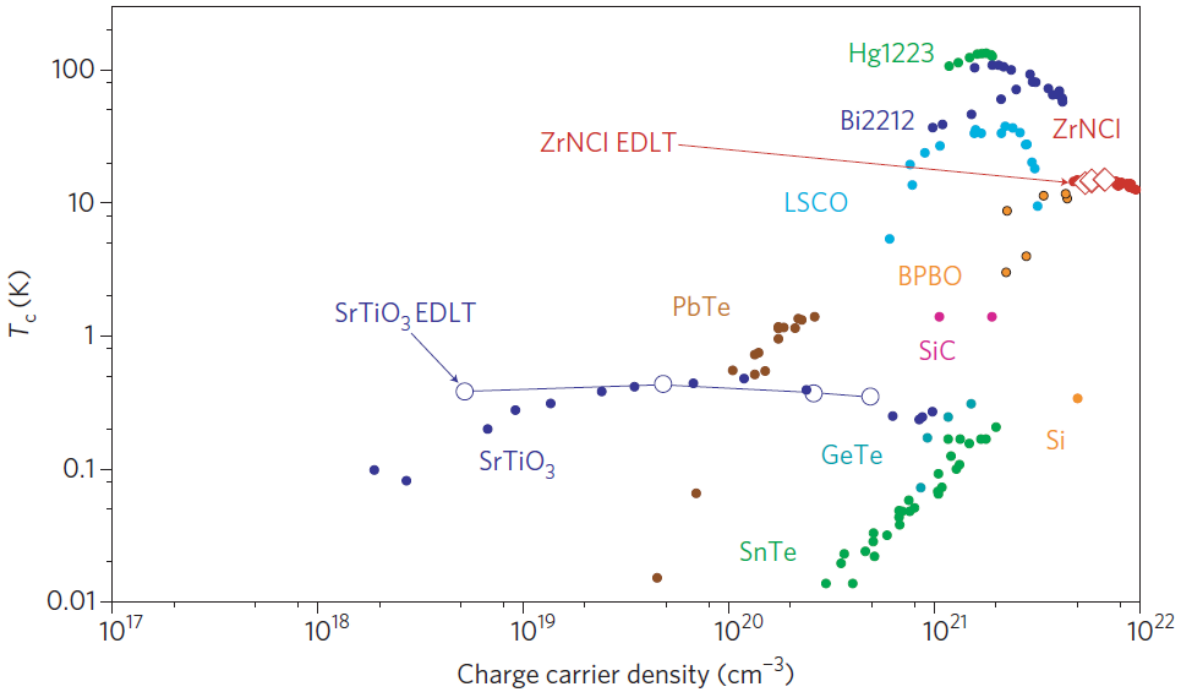

Figure 3.4.: Transition temperature into the superconducting state as a function of carrier density for eleven different systems, figure from [48]. More recently, STO with a carrier concentration as low as $5.5 \cdot 10^{17}$ cm^{-3} has been found to be superconducting as well [49].

Another striking feature of figure 3.4 is the low onset carrier number necessary for superconductivity. In STO, $5.5 \cdot 10^{17}$ cm^{-3} electrons have been found to be enough for a superconducting ground state even though this means that there is one electron per several thousands of atoms. This is a serious problem for phonon mediated superconductivity as described in section 2.2, because it translates into a situation were the Fermi temperature, describing electron speed, is much below the Debye temperature, describing phonon speed ($T_F < \Theta_D$). Using the picture introduced in section 2.2, the trace left in the lattice by a passing electron will vanish so fast that a second electron cannot be attracted by it in time. Alternative pairing mechanisms such as plasmons [50] or soft-mode phonons [51] are invoked by reference [52].

Furthermore, STO displays not only one but two superconducting domes which seem to be closely linked to changes in the Fermi surface of the material. For all superconducting STO samples analysed up to now, a metallic normal state with a sharp Fermi surface was found, allowing for the monitoring of changes in SdH quantum oscillations with increasing doping. Figure 3.5 from reference [52] shows how the transition temperature stops its

monotonous increase as soon as a second band is filled with electrons, but increases further when a third frequency appears.

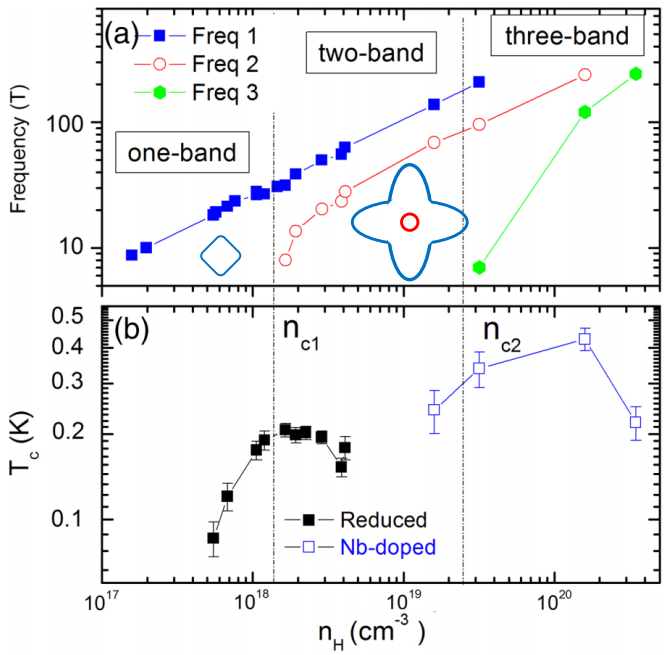

Figure 3.5.: Quantum oscillation frequency and transition temperature as a function of carrier density for oxygen-reduced and Nb-doped STO. The insets in the upper panel show sketches of the one and two band Fermi surfaces. Figure modified from [52].

In STO, the first band seems to be at the origin of superconductivity while the second band is hindering it - this, together with the extremely low onset concentration for a finite T_c, raises the question whether some electrons, characterised by their positions in k-space, are more important for superconductivity than others. In PbTe, it has been suspected that the emergence of a second set of pockets at the Σ-points as discussed in section 3.1 could be the cradle of superconductivity. Contrary to the lowest doped STO samples, superconducting PbTe does not lie within the range where $T_F < \Theta_D$ and phonon mediated pair formation is hence conceivable. In this case a second set of pockets at different k-space positions might introduce new intra-band phonon modes into the system that could be strong enough to produce a superconducting ground state. This will be discussed in more detail in chapter 7.

3.3 Negative U and superconductivity

"U" is a model parameter in the Hubbard model describing the interaction of particles on a lattice. In the case of electrons in a crystal it means the on-site electron repulsion energy and is related to the energy needed to move one electron from one atomic site to another. If E_n is the energy of a site loaded with n electrons, then U_n can be expressed as

$$U_n = (E_{n+1} - E_n) - (E_n - E_{n-1}). \tag{3.2}$$

The first half of the left side of equation (3.2) is the electron affinity of the state in question, the second is its ionisation energy. Generally U_n increases with n as the orbitals grow, but a few elements of the periodic table behave differently, their U_n passing through a minimum for a given n. One of them is thallium which has U-values of $U_1 = 14.3\,\text{eV}$, $U_2 = 9.4\,\text{eV}$ and $U_3 = 20.9\,\text{eV}$ in vacuum [53]. U is never below zero in vacuum because of the Coulomb repulsion between two electrons but may become negative in a solid due to charge screening in the polarised lattice as first proposed by Anderson in 1975 [54]. In those cases one charge state may always be preferred over another even though it forces two like carriers to occupy the same site. One of these valence skipping elements is thallium for which it is energetically unfavourable to assume the state Tl^{2+} - it is hence found to disproportionate

into Tl^{+} and Tl^{3+} in compounds where it would otherwise appear in its divalent state.

In the special case of $Pb^{2+}Te^{2-}$ doped with Tl, Tl replaces lead on its lattice side, a priori being required to take the corresponding charge state of 2+. However, at low doping levels the energetically most profitable state for the dopants is Tl^{+}, every dopant thereby introducing one hole into the system. The energy difference between the two allowed states Tl^{+} and Tl^{3+} is very small though, leading to a degeneration of the two energy levels at slightly higher doping. This has been explained theoretically by M. Dzero and J. Schmalian with a model negative-U Hamiltonian [55]:

$$H = E_0 + (\epsilon_0 - \mu)\sum_{\sigma} n_{s,\sigma} + U n_{s,\uparrow} n_{s,\downarrow} \tag{3.3}$$

where μ the chemical potential, $n_{s,\sigma}$ is the occupation for a spin σ hole in the Tl 6s-shell and $U < 0$. With this the energies of the three Tl valence states in question can be given as

$$E(Tl^{+}) = E_0, \tag{3.4}$$
$$E(Tl^{2+}) = E_0 + \epsilon_0 - \mu, \tag{3.5}$$
$$E(Tl^{3+}) = E_0 + 2(\epsilon_0 - \mu) + U. \tag{3.6}$$

As mentioned above, at low doping Tl^{+} is the lowest available energy state and hence additional holes move the chemical potential μ downwards in the valence band. At a critical doping level x^* and the corresponding chemical potential μ^* the energy difference between the monovalent and trivalent states $\delta E = 2(\epsilon_0 - \mu) + U$ vanishes and additional dopants assume either state with equal probability. Because Tl^{+} ions are electron acceptors in PbTe while Tl^{3+} are electron donors the carrier concentration should stop to increase when more thallium is added above x^* and remain at a constant value. The chemical potential remains fixed at μ^* for the same reason. Dzero and Schmalian calculate x^* to be around 0.5% [55] and this has been confirmed experimentally by Murakami [56].

The presence of two energetically degenerate valence states in Tl:PbTe with doping higher than x^* invites speculations about dynamic valence fluctuations between the two. These could be phenomenologically similar to the spin fluctuations leading to the Kondo effect in systems with magnetic impurities and have hence been associated with the term “charge Kondo effect”. In the more common spin Kondo effect, first described by J. Kondo in 1964 [57], a conduction electron with (without loss of generality) spin up scatters with a spin down electron on an impurity site, temporarily flipping the spin on the impurity site. In the final state both spins have returned to their initial orientation. By including this second order scattering process into his calculation of the temperature dependence of metallic resistivity Kondo was able to explain the long standing puzzle of the low temperature upturn observed experimentally some thirty years before [58].

In the case of dynamic charge fluctuations in systems with valence skipping elements a conduction hole is scattered onto a Tl^{+} site and leaves it together with the hole that had already been there, producing the intermediate state Tl^{3+} (or vice versa). This transition from one valence state to the other has been called a pseudospin flip. Once the system has returned to its original state, the second-order scattering analogy the spin Kondo effect is complete and a low temperature resistivity upturn to be expected [59]. Indeed this has been observed in experiments on Tl:PbTe, thereby supporting the charge Kondo picture [60]. The valence-skipping nature and consequent valence-fluctuating behaviour of Tl impurities may provide an unconventional real-space pairing mechanism because they involve two electrons travelling together from Tl^{3+}-sites to Tl^{+}-sites. This is being discussed both for being at the origin of superconductivity in the system and for strongly enhancing its T_c.

3.4 Fermiology and negative-U: (In:)SnTe

Hulm and co-workers found the rocksalt compound tin telluride (SnTe) to have a superconducting ground state with transition temperatures below 200 mK when doped with tin vacancies [22]. SnTe and PbTe have similar band structures and the low doping Fermi surface of four ellipsoidal pockets is confirmed for both systems [39, 61]. However, self-doping in SnTe allows for carrier concentrations above 10^{21} cm^{-3} whereas self-doped PbTe does not surpass 10^{19} holes per cm^3. The carrier concentration accessible in pure PbTe remains below the value identified as critical for superconductivity when using Tl impurities. In SnTe, Σ-pockets as described for PbTe at room temperature in section 3.1 were observed using SdH and dHvA experiments for carrier concentrations above $3.6 \cdot 10^{20}$ cm^{-3}.

Remarkably, this is close to the lowest carrier concentrations at which a superconducting ground state was observed in reference [22]. Additionally, the high doping-levels attainable in SnTe even seem to allow the system to pass into the regime of the third Fermi surface topology discussed above and shown in figure 3.3(b), the interconnected tube system. Littlewood *et al.* have performed a combined theoretical and experimental study on a sample with $p = 1.14 \cdot 10^{21}\,\mathrm{cm}^{-3}$ corresponding to a doping of about 7% and have found striking agreement between density functional calculations and ARPES [62].

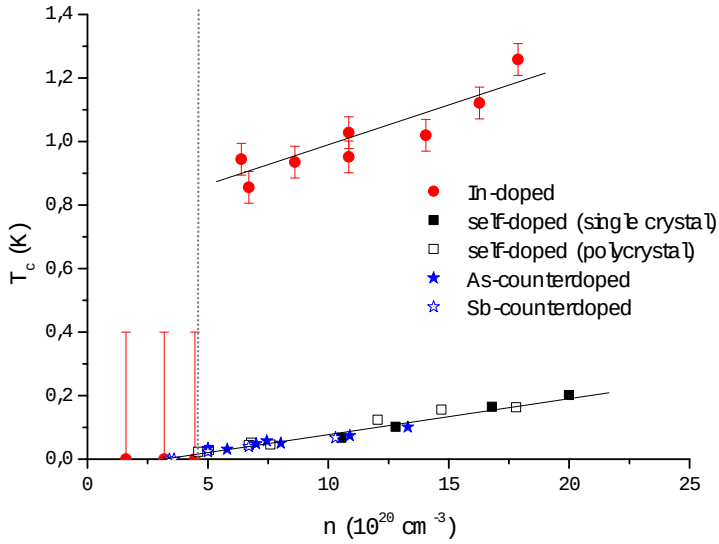

Figure 3.6.: Comparison of T_c values of self- and indium-doped SnTe. Black lines are drawn to guide the eye; no superconductivity was observed to the left of the grey line, possibly due to experimental limitations. Data for self-, As- and Sb-doped SnTe was taken from reference [22], data for In:SnTe from [63]. The latter was rescaled from In content to carrier concentration using the factor given in the reference.

Recently Erickson and co-workers have doped SnTe with indium, another candidate for valence fluctuations [64]. Intriguingly, the transition temperatures that they found were about one order of magnitude above those reported by Hulm. A comparison of the two datasets is shown in figure 3.6. The analysis of SnTe as compared to PbTe is complicated by the fact that it undergoes a structural phase transition from cubic structure at high temperatures to rhombohedral at lower temperatures. The critical temperature for this transition decreases with rising doping and has been found independent of the superconducting behaviour of the material [63]. As a result of this finding it is assumed that a direct comparison between the superconducting properties of PbTe and SnTe is valid.

In summary, SnTe seems to exhibit a cut-off carrier concentration for superconductivity to appear. This concentration can be reached both with vacancy and third-party dopants, but the transition temperature is greatly enhanced when the valence-skipping element indium is used as an impurity. Additionally, there is a topological change in Fermi surface from a single set of L-point pockets to two sets at L- and Σ-pockets respectively appearing in the region of the superconductivity on-set. The carrier concentrations accessible in PbTe remain much below the values in SnTe for all types of doping and superconductivity has only been observed with the valence fluctuating dopant thallium. However, even with Tl-dopants T_c for doping levels just above the cut-off is below 100 mK allowing for the interpretation that the charge Kondo effect is maybe not necessary for superconductivity itself but for the enhancement into the experimentally accessible region. This opens up room for the alternative interpretation introduced in section 3.2 where superconductivity is linked to the emergence of a new Fermi surface component, the Σ-pockets, both in SnTe and PbTe.

4 Methods and experimental set-ups

The data presented in chapter 5 was taken with three different measurement set-ups, two of them at the LPEM in Paris and one at the HFML in Nijmegen. These set-ups as well as the sample growth and preparation processes will be described briefly in the following.

4.1 Sample growth and preparation

All samples analysed in this project were grown by Paula Giraldo Gallo from Ian R. Fisher's group in Stanford by an unseeded vapor transport method as described in [32] and kindly supplied to us. For this, the commercially available starting materials PbTe, Te and Tl_2Te are mixed, ground into a powder and pressed into pellets. These pellets are then sintered at 600° C for one to two days before being ground and pressed again in order to provide a homogeneous polycrystalline mass of Tl:PbTe. This is then sealed in an evacuated quartz ampoule and placed in a horizontal furnace were it remains at 750° C for about a week. Within the ampoule there is a horizontal temperature gradient of about 1-2° C/cm from the centre outwards which transports the vapour originating from the source material in the middle towards the cooler ends where nucleation takes place and the single crystals start to grow. The crystals resulting from this technique are of a typical size of a few millimetres and show high symmetry faces ((100)-type square faces and (111)-type triangular faces) which give orientation for cleaving the samples into cuboids. An example is shown in figure 4.1(a).

The samples cleave preferably along [100]-type directions and this can be done by applying pressure with a sharp blade at room temperature. In this way, the samples were cut into cuboids of typical side lengths between 0.2 and 2 mm. In order to reach low contact resistances, gold pads were evaporated onto the samples for the quantum oscillation measurements. Before evaporation, using thin stripes of aluminium foil or threads drawn from liquid GE varnish, masks were patterned onto the samples. Depending on the individual shape and size of each sample, these left either four parallel stripes or the four sample corners open for the 50 nm gold layer (see figure 4.1(b)). As lead oxidises quickly in air, it is important to scratch the sample surface right before the evaporation process in order to expose a fresh crystal layer. After evaporation, 50 μm silver wires were attached to the gold pads using the single component silver paint DuPont 4929 which was left to dry in air. For the smallest samples the use of 20 μm silver wire proved necessary. With this method, contact resistances of the order of 5 Ω could be reached and, more importantly, remained low for several weeks allowing for sample preparation in advance.

Neither of the contact configurations in figure 4.1(b) is suitable for measuring precise absolute resistivity values as they introduce large uncertainties into the geometrical factor. The properties of quantum oscillations in resistivity are however unaltered by this which is why this does not pose a problem for most part of this work. In order to measure the absolute quantity which is the Hall coefficient and hence the Hall carrier concentration as precisely as possible, contacts were attached to the four side surfaces of the sample such as to pass the current through in one direction and measure the Hall voltage perpendicularly. This allows for a much more accurate determination of the geometrical factor of the sample, but gold pads had to be waived. This resulted in slightly higher contact resistances of around 50 Ω for the Hall effect measurements. Contacts that were prepared without gold pads were found to deteriorate within a matter of hours and could hence only be used for one measurement directly after their installation.

4.2 Experiments with the dilution refrigerator at LPEM

When measuring with the dilution refrigerator in the Paris laboratory a simple copper sample holder with 24 wires was used to mount the samples onto. The samples were either glued directly to the copper insulated with cigarette paper or first attached to a small copper plate insulated in the same way in order to facilitate the detachment of the sample without destroying the contacts. The gold or silver wires attached to the sample as described above were connected to the sample holder's copper wires with silver paint. Between sample holder and probe, twisted pairs of copper wires were laid such as to eliminate magnetic field effects on the measurement results. The manganine wires between bottom and top of the probe were equally prepared as twisted pairs. Once the sample holder with

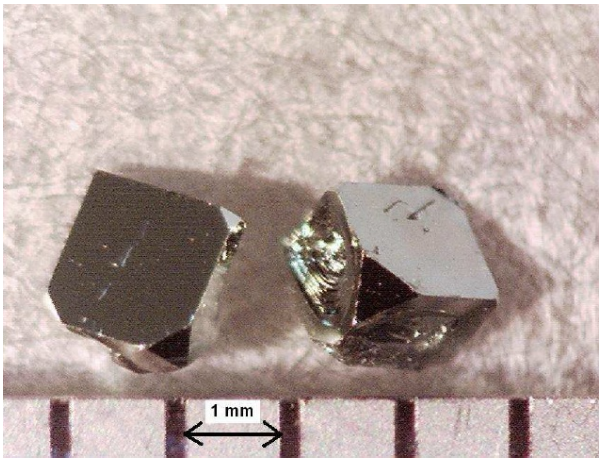

(a) Tl:PbTe crystals after growth displaying clear [100]- and [111]-faces. Figure from [32].

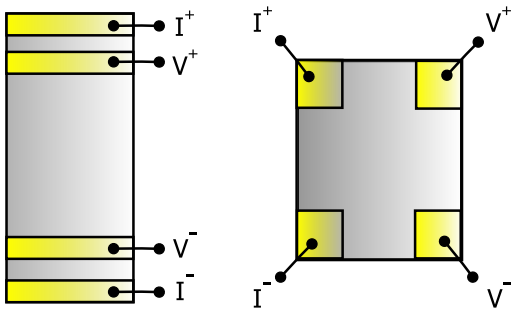

(b) The two kinds of gold contact patterns used for Shubnikov - de Haas experiments.

Figure 4.1.: Sample growth and contact preparation.

up to four or six samples in the cases with Hall voltage measurement (six wires per sample) and without (four wires per sample) respectively was connected to the probe, the inner vacuum chamber was closed with an indium seal. Pressures of some 10^{-6} mbar at room temperature were attained with this. After pumping the dilution unit of the refrigerator for several hours for cleaning purposes the whole unit was inserted into a 17 T solenoid within a liquid helium dewar shielded thermally by liquid nitrogen. By introducing some exchange gas (helium) into the inner vacuum chamber the samples were cooled to the liquid helium temperature of 4.2 K at this stage.

To reach temperatures in the mK range with the dilution unit a mixture of 25% ^{3}He and 75% ^{4}He is let into a thin capillary at the top of the refrigerator and thermalised to 4.2 K on its way downwards through the surrounding liquid ^{4}He. At the moment it reaches the still it is rapidly cooled down to around 800 mK through isenthalpic reduction of pressure when pouring into a larger volume, the so-called Joule-Thomson effect. Through several temperature exchangers and a second Joule-Thomson impedance the still is connected to the heart and coldest point of the dilution unit, the mixing chamber. Here the spontaneous phase separation of ^{3}He/^{4}He into two distinct phases at around 870 mK is exploited to reach extremely low temperatures. Figure 4.2(a) shows how the ^{3}He concentration in the "concentrated" (^{3}He rich) phase tends to 100% while the "dilute" phase always sustains a lower limit of 6.4% ^{3}He as the temperature goes to zero. At the interface between the two phases a cooling effect is given when one atom of ^{3}He crosses from the concentrated to the dilute phase, a process similar to the cooling associated with the evaporation of a liquid (concentrated phase) into a gaseous (dilute) phase. The heat necessary for this evaporation is taken from the mixing chamber environment and is hence the useful cooling power of the device. In order to keep this cooling process running continuously, ^{3}He in the dilute phase is pumped away from the mixing chamber into the still and back out of the unit from there. The pressure in the still is kept at a specific low value to make use of the fact that the partial pressure of ^{3}He at low temperatures is much larger than that of ^{4}He. In the chosen conditions, the ^{4}He is in a superfluid state and the vapour running through the still is almost pure ^{3}He. Because of the concentration difference between the vapour in the mixing chamber and the vapour in the still an osmotic pressure pulls ^{3}He out of the dilute phase in the mixing chamber and keeps the cooling process of atoms crossing the phase boundary running. Figure 4.2(b) shows a picture of the the dilution unit used for these experiments, the commercially available but custom-made system DR-JT-S-12-1093 from cryoconcept. Several exchangers help to keep the low temperature once the system is in the steady state - they transfer the heat of the incoming mixture to the cold outgoing vapour.

When measuring with the dilution fridge and the 17 T solenoid, DC measuring techniques were applied. As a current source a Keithley 6221 DC and AC current source was used and during low magnetic field measurements (<2000 Gs) a Keithley 2420 SourceMeter supplied the current to the solenoid. For high magnetic fields the current was supplied by a magnet power supply from cryogenic. Voltages were read with Keithley 2000 Multimeters and either an EM DC Nanovoltmeter N31 or an EM DC Picovoltmeter P13 connected ahead. The temperature was regulated using a LakeShore 370 AC resistance bridge. During most runs, three thermometers were installed,

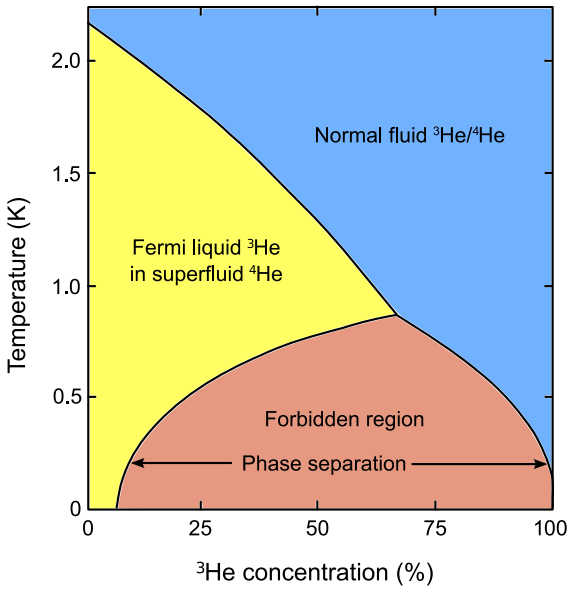

(a) Phase diagram of ^{3}He/^{4}He mixture at low temperatures.

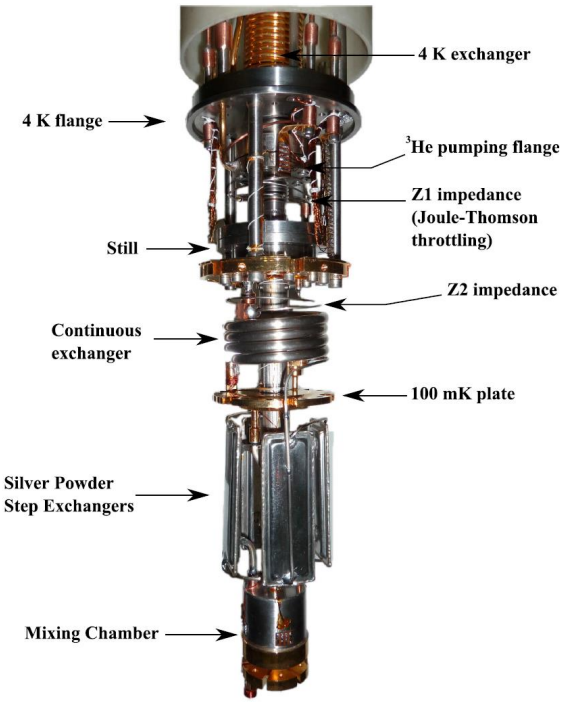

(b) The low temperature part of the dilution refrigerator. Figure from cryoconcept manual.

Figure 4.2.: Cooling into the mK regime with a ^{3}He/^{4}He dilution system.

one each on still, mixing chamber and sample holder. Heaters were installed on the sample holder and on the still, the former serving principally for the temperature regulation of the sample and the latter for evaporating the condensed mixture when warming up the experiment. Measurement cycles were programmed using a LabView routine. The setup allowed for base temperatures of 20 mK and a maximum magnetic fields of 17 T for both field orientations. It was primarily used to search for superconducting transitions.

4.3 Experiments with the PPMS at LPEM

For all angle-dependent studies performed at LPEM a QuantumDesign Physical Property Measurement System (PPMS) with DC resistivity option loaded with a horizontal rotator probe was used. The system reaches a minimum temperature of about 2 K by pumping on ^{4}He and has a very stable temperature regulation. Maximum magnetic fields are $\pm$14 T. The sample holder for the rotation probe can hold two samples with four wires each, but one of these channels was used for a Hall probe during all rotation measurements in order to verify the orientation of the magnetic field relative to the sample. The sample holder displays gold pads and the wires coming from the sample were connected to those using silver paint. Programming of measurement routines and data acquisition was done with the QuantumDesign software MultiVu.
The PPMS was used for extensive angle-dependent studies of quantum oscillations with rotation stepsize down to 2 °, for measuring the temperature-dependence of resistivity and also for determining the Hall carrier density of all samples at 2 K.

4.4 Experiments at the HFML

A large part of the data presented in chapter 5 was acquired during a two-week measurement campaign at the High Field Magnet Laboratory (HFML) in Nijmegen, The Netherlands. We used Cell 5 in the north hall which offers a 33 T Bitter magnet. Bitter magnets are not made of coils of wire but of circular metal plates separated by insulating spaces all stacked into a helix. The plates are perforated by many holes to allow for water cooling of the magnet setup while in operation - about 40 kA are needed to produce 32 T and the heat dissipation is enormous.

Measurements in Nijmegen were performed on a horizontally rotating sample holder able to carry four samples with four contacts each. One of these spots was used for a Hall probe to allow for in situ positioning of the rotator. For this, the field was swept up to 5 T, the setup was orientated as required and the field brought back to zero before performing full field sweeps to ±32 T. All angle-dependent measurements were performed at a temperature of 1.7 K which was kept stable by adjusting the pumping power on the helium bath. Here, AC measurement techniques and equipment were used for availability reasons and no significant difference in data quality was observed in comparison to the Paris DC data. The equipment used consisted of a Stanford Research Systems SR830 DSP Lock-In Amplifier and a SR560 Low-Noise Preamplifier for each sample. During the temperature-dependent measurement series a LakeShore resistance bridge was used for temperature regulation.

5 Experimental Results

This chapter shows a cross-section of the data obtained during this project. The first section introduces the analysed samples and discusses their properties deduced from transverse and longitudinal transport measurements in the normal state, notably their Hall carrier concentrations and their temperature-dependent resistances. In section 5.2, the results of the SdH-experiments probing the Fermi surface are shown. At low doping, the model of four ellipsoids could be confirmed while at higher doping additional features emerge. Furthermore, quantum oscillation measurements at different temperatures allowed to quantify the minimum masses of the L-pocket carriers for almost all the samples - these are shown in section 5.3. This chapter also gives the Fermi energies over a large part of the doping range and confirms that it indeed seems to stay constant above a critical doping level. In the final part, section 5.4, the superconducting transitions in the samples with $x_{\mathrm{Tl}} = [0.55\%, 0.7\% 0.8\%]$ at various different fields are shown and a peculiar anomaly is introduced.

5.1 Sample introduction and normal state properties

During the course of this project lead telluride samples with eight different thallium doping-levels were analysed using electrical transport measurements. The available Tl-concentrations were 0.2%, 0.25%, 0.3%, 0.35%, 0.4%, 0.55%, 0.7% and 0.8% as supplied to us by Paula Giraldo-Gallo from Stanford University. The samples were prepared and measured using processes and devices as described in chapter 4. In cases where several distinct samples were used because of loss or destruction of the first specimen, the replacement stemmed from the same batch (same growth process) and is hence expected to have almost identical properties. An overview over all physical quantities extracted in these measurements is given in table 5.1. This table also indicates which type(s) of experiment were performed on each sample.

During the fabrication of the sample, stoichiometric weight fractions of the base materials are mixed and ground together such as to reach a given Tl-concentration in the single crystal after growth. Due to the extremely small Tl-dopings in the region below one atomic percent and because the different base materials may stick to the used vessels in different ways and amounts, an absolute error of $\pm 0.1\%$ Tl has to be assumed according to the producer. Following this, the eight Tl-concentrations given above can be interpreted only as an approximation and will hence also be called “nominal” thallium concentration in the following. However, as discussed below, in most cases the agreement between measured Hall carrier concentration and expected carrier concentration from the nominal Tl-content was much better, therefore putting the need for an error bar this large into question for concentrations above $x_{\mathrm{Tl}} = 0.3\%$.

Another possibility to determine the impurity concentration of a given sample is its residual resistance ratio (*RRR*). At high temperatures the resistance R of metals is dominated by scattering processes between the conduction electrons and phonons and can be described by a power law. As the sample is cooled down, more and more phonon modes fade away and the resistivity becomes controlled by impurity scattering, thereby approaching a constant value in many cases. This is the so-called residual resistance, completely given by impurity concentration. The residual resistance ratio is theoretically defined as the ratio between room temperature resistivity and 0 K resistivity, but it is mostly given as the ratio between ρ at room temperature and ρ at the lowest accessible temperature. The values presented in this work are extracted as follows:

$$RRR = \frac{\rho(300\,\mathrm{K})}{\rho_0}, \quad \rho_0 \equiv \rho(2\,\mathrm{K}). \tag{5.1}$$

As the thallium content increases, the number of impurities and hence the number of impurity induced scattering processes rise as well. As discussed, the room temperature resistivity is hardly effected by this, but the low temperature value is a sensitive probe. However, because of the gold contact pattern shown in figure 4.1(b) the absolute resistivity values carry a large error and are not suitable for comparison. The *RRR* is a much more useful tool to this end because it is a dimensionless quantity and uncertainties in sample geometry cancel out. However, for sake of completeness, ρ_0 was below 0.5 mΩ cm for all samples while the room temperature resistivity reached up to about 3 mΩ cm for the lowest doping levels. Figure 5.1 shows the *RRR*s measured here together with *RRR* values

nominal Tl content (%)	p_{Hall} ($10^{18}cm^{-3}$)	hole doping (%)	RRR (-)	F^{L}_{min} (T)	F^{Σ}_{min} (T)
0.2±0.1	15±3	0.10±0.02	29.5±0.1	34±2	0
0.25±0.1	39±4	0.26±0.04	13.9±0.1	48±2	0
0.3±0.1	46±4	0.31±0.03	6.9±0.1	58±2	0
0.35±0.1	58±6	0.39±0.04	4.5±0.1	61±2	nn
0.4±0.1	61±8	0.41±0.06	5±0.5	63±2	18±4
0.55±0.1	75±6	0.51±0.04	3.8±0.2	68±3	23±6
0.7±0.1	90±6	0.61±0.04	3±0.2	70±3	26±7
0.8±0.1	95±6	0.65±0.04	3±0.5	nn	nn

nominal Tl content (%)	m^{L}_{min} (m_e)	E_F (meV)	T_c (mK)	performed experiments
0.2±0.1	0.058±0.004	67±6	nn	Hall, QO^{PPMS}, QO^{HFML}
0.25±0.1	0.064±0.006	87±8	nn	Hall, QO^{PPMS}
0.3±0.1	0.076±0.004	88±7	0±40	Hall, QO^{PPMS}, QO^{HFML}, T_c
0.35±0.1	0.080±0.006	88±9	0±40	Hall, QO^{PPMS}, T_c
0.4±0.1	0.085±0.006	86±8	0±40	Hall, QO^{HFML}, T_c
0.55±0.1	0.083±0.008	95±11	307±10	Hall, QO^{HFML}, T_c
0.7±0.1	0.09±0.01	90±11	543±10	Hall, QO^{HFML}, T_c
0.8±0.1	nn	nn	730±10	Hall, T_c

Table 5.1.: Summary of all quantities measured in this work. The last column names the experiments that were performed on each sample. All Hall measurements were done in PPMS at $T = 2K$, all T_c measurements in the dilution refrigerator at LPEM. Quantum oscillation (QO) experiments were performed in PPMS and/or at the HFML as indicated. Quantities that were not determined during any of these experiments are marked with "nn".

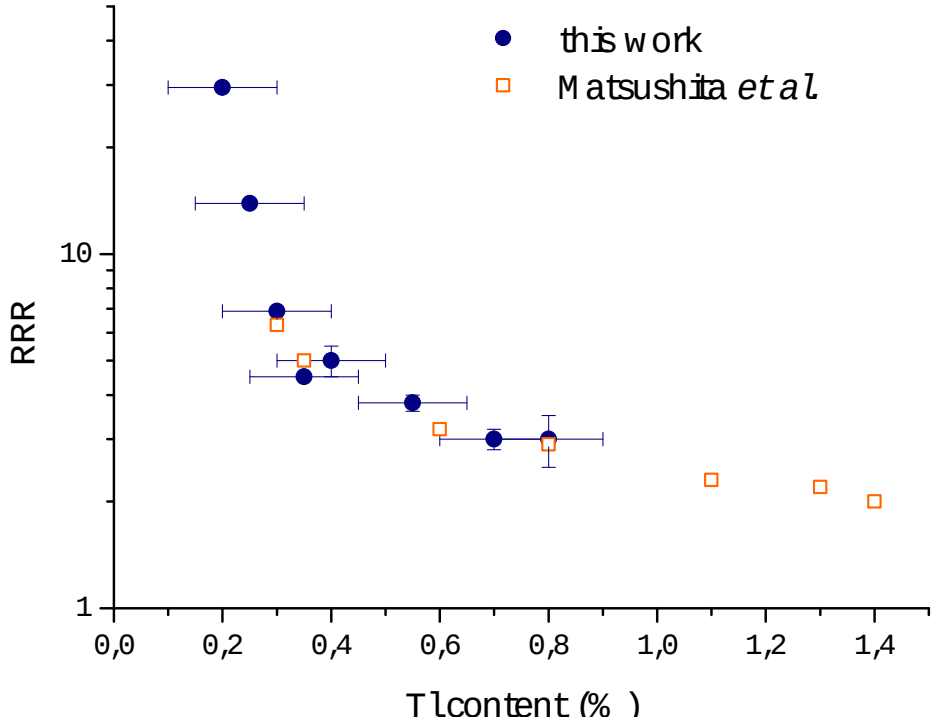

Figure 5.1.: Residual resistance ratio as a function of nominal Tl-doping on a logarithmic scale. Blue points are results from this work, orange points are taken from [32] to show the evolution at higher doping. The RRR decreases rapidly as additional Tl-impurities are introduced.

from reference [32]. The ratio drops very fast with increasing doping. As this display of 15 different data points shows, the relationship between Tl-content and *RRR* is robust, thereby offering a means to cross-check whether the nominal Tl-content is close to reality by measuring the samples $\rho(T)$.

From the Tl-content of a sample it is possible to calculate the expected carrier concentration under the assumption that every thallium dopant contributes one hole to the system. This is expected to be the case at low doping levels (below about 0.4%), as discussed in section 3.3. PbTe has a lattice constant of $a = 6.464\,\text{Å}$ leading to a unit cell volume of $V = a^3 = 270.09\,\text{Å}^3$. Every unit cell of the fcc PbTe lattice contains four lead atoms and it is lead which is replaced by thallium upon doping. Using this information, the expected density of holes p_{Tl} introduced by a thallium fraction x_{Tl} can be calculated to equal

$$p_{\text{Tl}} = \frac{4}{a^3} \cdot x_{\text{Tl}} = \frac{4}{V} \cdot x_{\text{Tl}} = 1.48 \cdot 10^{22}\,\text{cm}^{-3} \cdot x_{\text{Tl}}. \tag{5.2}$$

This means that a sample with 0.1% Tl-doping is expected to have a carrier concentration of $1.48 \cdot 10^{19}\,\text{cm}^{-3}$. The intrinsic carrier concentration of undoped PbTe is of the order of $10^{18}\,\text{cm}^{-3}$ or below, therefore carriers stemming from non-stoichiometric growth can be neglected compared to Tl-induced holes within our accuracy.

The Hall carrier concentrations of all eight doping-levels at hand were measured within PPMS. The transverse voltage was measured for both positive and negative fields to be able to anti-symmetrise the data and get rid of possible longitudinal voltage components due to contact misalignment. The Hall carrier concentration p_{Hall} was extracted from the slope of the Hall voltage V_{Hall} as a function of current and the sample thickness t as follows:

$$\frac{V_{\text{Hall}}\,t}{IB} = R_{\text{Hall}} = \frac{1}{p_{\text{Hall}}\text{e}}, \tag{5.3}$$

where I is the applied current, B is the magnetic field, e is the electron charge and R_{Hall} is Hall's coefficient. The error in the resulting carrier number is completely determined by the uncertainty when determining the sample's thickness. Most samples were thinner than 1 mm and did not have a constant thickness over their whole length and width either, so this error was as large as 20% for the smallest samples. Compared to this, the error in the voltage

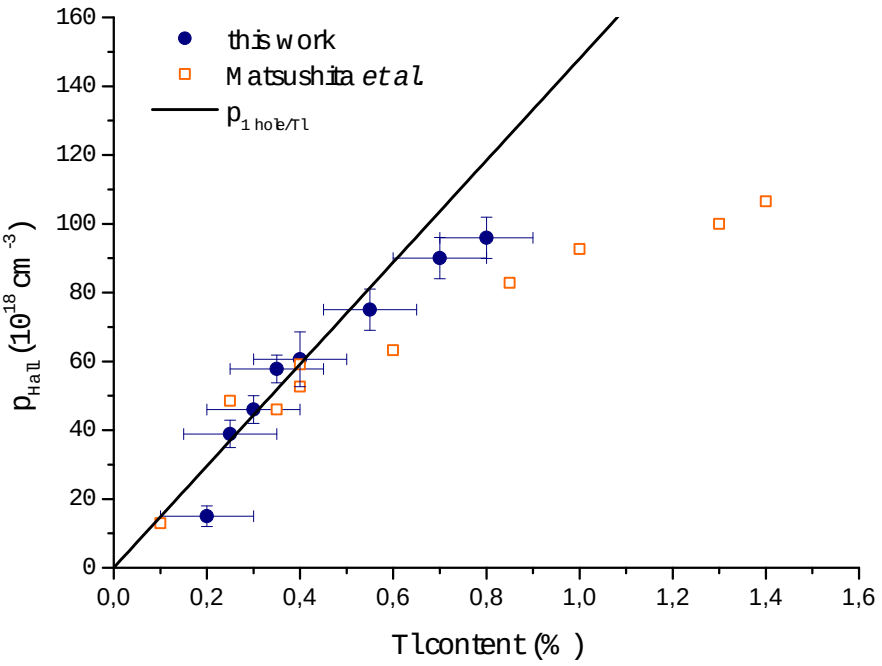

Figure 5.2.: Hall carrier density as a function of nominal Tl-doping. The black line indicates the carrier concentration expected if every dopant contributes one hole. Orange points from reference [32].

measurement which is well below 1% can be neglected. This geometric error propagates into quantities calculated from the Hall carrier concentration and is the dominant uncertainty there as well. It is hence best to avoid further calculations with the quantity where possible.

Figure 5.2 shows the measured carrier concentrations as a function of nominal Tl-doping. A line indicates the position of the expected carrier concentration for the case where one hole per dopant is introduced. It can be seen that for Tl concentrations above 0.4% the measured values remain below this line. This is in agreement with the idea of Tl disproportioning into Tl^{+} and Tl^{3+} above a certain doping level, thereby adding donors and acceptors in similar quantities as described in section 3.3. The doping range analysed here does not extend far enough to show whether the carrier concentration goes into almost full saturation as calculations by Zlatic [59] or continues to increase with a reduced slope as found experimentally by Matsushita [65].

One of the most prominent signatures of a charge Kondo scenario is the resistivity upturn at low temperatures, the phenomenon which inspired Kondo's calculations in the original case of magnetic impurities. In this study a small resistivity upturn was evident for all samples with a doping level above 0.3%. Figure 5.3 shows how the upturn emerges when going from lower to higher doping levels. The first panel shows the resistivity of $x_{\mathrm{Tl}} = 0.25\%$ as a function of temperature; it approaches a plateau at low temperatures and no upturn is observed. In the two lower panels, $x_{\mathrm{Tl}} = 0.3\%$ and $x_{\mathrm{Tl}} = 0.35\%$, the upturn is clearly observable and grows in strength with increasing Tl-content. However, the effect happens on the scale of some $\mu\Omega$ and is therefore more clearly displayed in the insets to figure 5.3.

5.2 Fermi surface

This section summarises all findings concerning the carrier-dependent evolution of the Fermi surface of Tl:PbTe, beginning with a short discussion of experimental issues and limitations before following the evolution of the L-pockets with doping level and coming across an additional feature around 0.4% Tl.

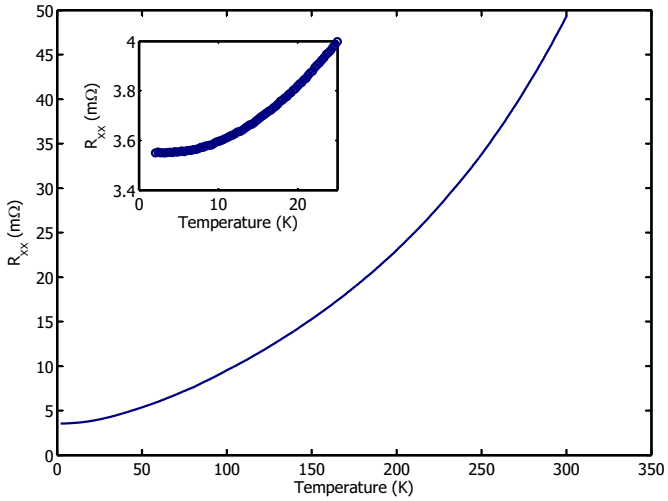

(a) x=0.25% Tl.

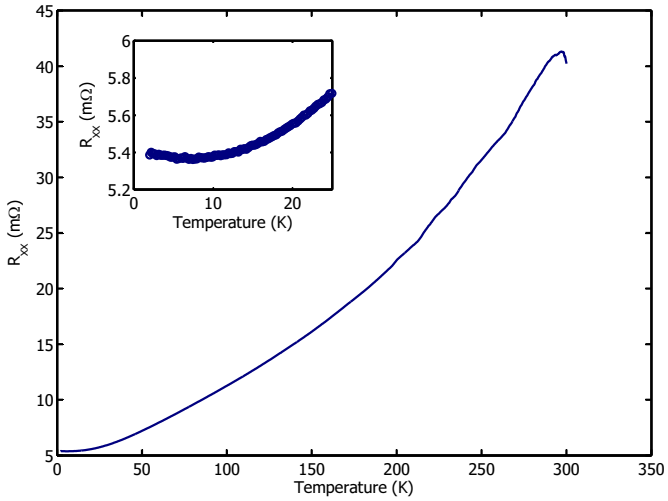

(b) x=0.3% Tl.

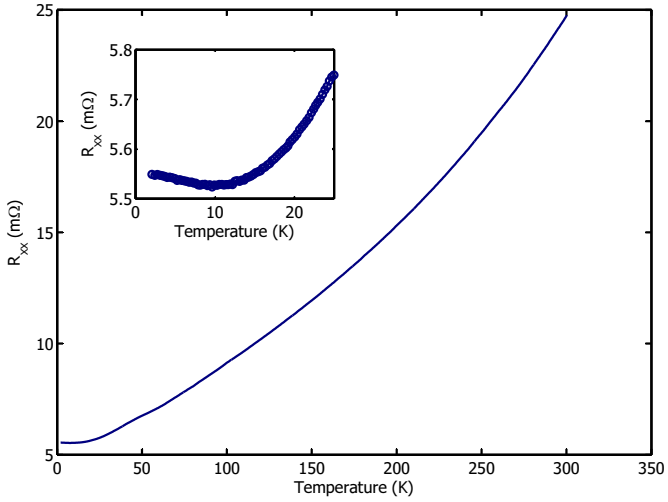

(c) x=0.35% Tl.

Figure 5.3.: Temperature-dependent resistances of three different Tl:PbTe samples. The insets show the low temperature region between 0 and 25 K.

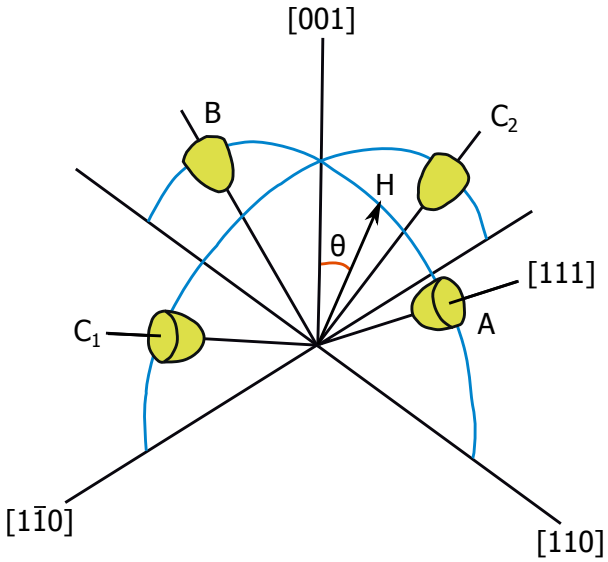

(a) Orientation of the magnetic field vector with respect to the Fermi surface. The magnetic field vector is called H here to avoid confusion with L-pocket B.

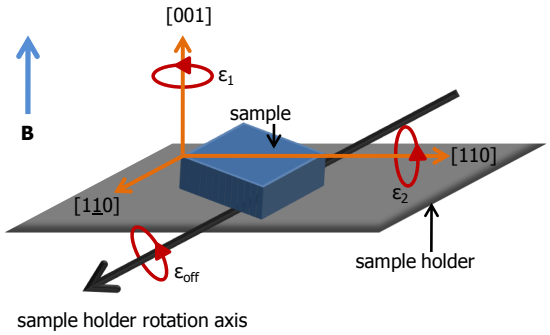

(b) Visualisation of possible misalignment problems of the sample within the setup. The sample may be unintentionally rotated around three independent spatial directions.

Figure 5.4.: Orientation of magnetic field with respect to the sample and possible misalignment issues.

5.2.1 Rotation, misalignment and mobility issues

During all quantum oscillation experiments presented in the following the sample was mounted on a rotating sample holder in such a way that it could be turned to align three directions of high symmetry in the crystal parallel to the magnetic field: $\mathbf{B} \parallel [001]$, $\mathbf{B} \parallel [110]$ and $\mathbf{B} \parallel [111]$. All of these directions lie within the $(1\bar{1}0)$-plane which is why the rotation axis of the sample was chosen to be parallel to $[1\bar{1}0]$. Figure 5.4(a) shows this set-up and how the orientation of the magnetic field relative to the sample can be specified by the angle θ between [001] and field vector in the $(1\bar{1}0)$-plane. Here, the three components of the magnetic field are given by

$$\begin{aligned} B_x &= \frac{\sin\theta}{\sqrt{2}} \\ B_y &= \frac{\sin\theta}{\sqrt{2}} \\ B_z &= \cos\theta, \end{aligned} \tag{5.4}$$

and the three high symmetry directions [001], [111] and [110] correspond to 0°, 54.7° and 90° respectively. The axes $\mathbf{x}, \mathbf{y}, \mathbf{z}$ refer to the crystal directions [100], [010] and [001] respectively.

Because of the small size of the samples and their slightly non-rectangular shapes it is difficult to align the $[1\bar{1}0]$-crystal direction with the rotation axis of the sample holder with high precision. Errors of up to five degrees in all three spatial directions could not be avoided during the eye-guided alignment process. These misalignment problems can be incorporated into the theoretically expected oscillation frequencies for a given Fermi surface model by adjusting the effective magnetic field values accordingly. Here, misalignment in all three spatial directions has to be taken into account. The three possible errors are described by rotation angles around the corresponding axes as visualised in figure 5.4(b). An unwanted rotation around the rotation axis of the sample holder produces an offset on θ and is hence called ϵ_{off}. Rotations around the two directions perpendicular to the rotator axis are a little more complicated to account for and will be called ϵ_1 and ϵ_2 as shown in the figure.

When calculating the expected frequencies for a chosen Fermi surface model with the aim of comparison to experimental data, the magnetic field vector has to be adjusted to include $\epsilon_{\text{off}}, \epsilon_1$ and ϵ_2. This means that the field components given in equation (5.4) have to be replaced by

$$\begin{aligned} B_x &= \frac{\sin(\theta+\epsilon_{\text{off}})\cdot\cos(45^\circ+\epsilon_1)+\cos(\theta+\epsilon_{\text{off}})\cdot\sin\epsilon_2}{\sqrt{2}} \\ B_y &= \frac{\sin(\theta+\epsilon_{\text{off}})\cdot\cos(45^\circ-\epsilon_1)-\cos(\theta+\epsilon_{\text{off}})\cdot\sin\epsilon_2}{\sqrt{2}} \\ B_z &= \cos(\theta+\epsilon_{\text{off}})\cdot\cos\epsilon_2. \end{aligned} \tag{5.5}$$

In samples with Tl doping above 0.4% the experimental possibility to rotate the sample is not only necessary to gain insight into the three-dimensional shape of the Fermi surface but it is vital to see oscillations at all. This is due to the fact that the average mobility of the charge carriers in Tl:PbTe decreases as a function of doping for two reasons: firstly, as the number of impurities rises the electron scattering time goes down and secondly, as will be discussed in more detail in section 5.3, the effective mass rises as a function of carrier concentration as well. Mobility μ, scattering time τ and effective mass $m^\star$ are related by

$$\mu = \frac{\mathrm{e}\tau}{m^\star}, \tag{5.6}$$

so both effects have a negative influence on mobility. The average mobility measured in x=0.3% Tl:PbTe was around $800\,\mathrm{Gs}^{-1}$ while it did not exceed $200\,\mathrm{Gs}^{-1}$ in an $x_{\text{Tl}} = 0.7\%$ sample. This means that the fields necessary to see quantum oscillations are four times as high because the condition that carriers must be able to complete at least one full circuit on their Fermi surface orbit, $\omega_c\tau > 1$, can be translated into a condition for the minimum field needed to see oscillations:

$$\omega_c\tau > 1 \leftrightarrow \left(\frac{\mu m^\star}{\mathrm{e}}\right)\left(\frac{\mathrm{e}B}{m^\star}\right) > 1 \leftrightarrow B > \frac{1}{\mu}. \tag{5.7}$$

Following this rough estimation, 12 T are sufficient to see oscillations for $\mu = 800\,\mathrm{Gs}^{-1}$, but almost 50 T are needed if $\mu = 200\,\mathrm{Gs}^{-1}$. In samples with very low mobility, the rotating sample holder serves as a tool in exploiting the anisotropy of the mobility which is directly linked to the anisotropy of the Fermi surface pockets. For ellipsoidal pockets with an anisotropy of $K = 13$, the effective mobility for $\mathbf{B} \parallel [111]$ is a factor $\sqrt{13}$ times larger then for the direction perpendicular to it. This means that even if no oscillations can be observed for a conventionally mounted sample where $\mathbf{B} \parallel [001]$, it may still be possible to track them for $\mathbf{B} \parallel [111]$.

For samples with $x_{\text{Tl}} < 0.4\%$ the magnetic field strength available in PPMS (± 13.5 T) was sufficient to show oscillations over a wide range of angles. Due to the multi-pocket Fermi surface of PbTe even at low doping, in the general case more than one oscillation frequency is observed and two or even more waveforms overlap. In the following section, Fourier transformation of this data will be introduced as a means to disentangle the different components of the oscillation spectra and make use of them quantitatively. There is, however, a way of displaying oscillation spectra at different angles in such a way that qualitative features of the Fermi surface become evident. Two examples for this are shown in figure 5.5. Here, the $\rho(B)$ curves displaying oscillations taken at a large number of different angles θ are translated into a colour scale, where peaks in resistivity receive a colour from the red end of the spectrum and troughs are coloured in blue.

The first thing that strikes the eye when looking at figure 5.5(b) is that while in theory one would expect to see more than one oscillation frequency for all angles but $\theta = 0^\circ$ ($\mathbf{B} \parallel [001]$), over a wide range around [111] one sees the signature of one pocket only (pocket A in figure 5.4(a)). This is precisely due to the mobility issue discussed above: the cross sections of the other pockets for these field orientations are associated with mobilities so low that either they do not produce an oscillatory signature or it is so weak that it is completely dominated by the signal stemming from the smaller cross section. The mobility jump between the two samples with $x_{\text{Tl}} = 0.2\%$ and $x_{\text{Tl}} = 0.3\%$ is hence responsible for the evident difference between figures 5.5(a) and 5.5(b) - in the former, the oscillations from pockets B and C show in the data for a wider range of angles resulting in a more complicated pattern. In both colourmaps, the three high symmetry directions stand out and can be identified

by the characteristics expected from the Fermi surface model shown in figure 5.4(a): at [111], the cross section is minimised and so is the oscillation frequency. At [001], all three types of ellipsoids are cut by the field in the same way and produce degenerate signals, and at [110] A and B ellipsoids are degenerate producing a common signal while the cross section of ellipsoids C is to large to be observed at these fields. An overview of colourmaps like these produced from data taken at the HFML is shown in appendix B.1. These figures clearly confirm how the number of observable oscillations and the range where signatures of B- and C-ellipsoids are observed shrink with doping.

5.2.2 Evolution of the L-pockets

As discussed in the preceding section, the magnetic fields available in the LPEM setups are not large enough to see oscillations in all samples even for the optimum cross section at $\mathbf{B} \parallel [111]$. They are also not sufficient to follow the signature of one ellipsoid (for example ellipsoid A) throughout the whole angle range even for the lowest doped sample - at a given point the cross section becomes to large for oscillations to appear below 13.5 T (PPMS) or even 17 T (dilution fridge). If the ellipsoidal model is to be tested, however, and the influence of thallium on the Fermi surface to be compared to the data by Burke *et al.*, tracking the signature of a pocket over the whole θ-range is necessary. For these reasons, samples with $x_{\mathrm{Tl}} = [0.2\%, 0.3\%, 0.4\%, 0.55\%, 0.7\%]$ were probed up to 32 T at the HFML in Nijmegen.

For $\mathbf{B} \parallel [111]$ oscillations could be observed in all five samples. The number of observable oscillation periods and the amplitude of the peaks decreased rapidly with rising Tl-content, reducing the precision of the oscillation frequencies and masses extracted from the data. In all cases, a third-order polynomial background was fitted to the raw data for subtraction as described in section 2.1. The resulting oscillation pattern in resistivity over inverse field was Fourier transformed using the Matlab-script in appendix A.1 for all angles probed.

When applying a Fourier transformation algorithm to a data set, there are two different aspects governing the resolution of the resulting spectrum that need to be taken into account. The first is related to the real information content of the experimental data. It is immediately obvious that different frequencies contained in a signal can be resolved with higher accuracy if the field range over which the data is taken is larger because then a higher number of oscillation periods is recorded. This data-governed resolution, ΔR_{data}, is given as

$$\Delta R_{data} = \frac{1}{\Delta \tilde{B}}, \tag{5.8}$$

where $\Delta \tilde{B}$ is the range of the inverse field data that contains oscillations. For example, if oscillations become observable at 5 T, than $\Delta \tilde{B} = \frac{1}{5} - \frac{1}{32} = 0.17$, which translates into an intrinsic resolution of $\Delta R_{data} = \frac{1}{0.17} \approx 6$ T. This means that frequencies that are closer than 6 T to each other cannot be resolved with this data set. If oscillations became observable starting from 1 T, the resolution would be increased and the data would allow to resolve peaks as near as 1 T to each other. This shows how problematic it is that the mobility decreases with doping and that the magnetic field onset for oscillations is pushed further and further up. The second resolution involved in the Fourier process is related to the width of the bins that the algorithm produces output in and will be called ΔR_{FFT} here. This results directly from the number of points that are put into the algorithm and hence from the data spacing via

$$\Delta R_{FFT} = \frac{f_s}{N_{FFT}}, \tag{5.9}$$

where f_s is the sampling frequency and N_{FFT} is the total number of data points. In the simple case, where the whole section of data which is Fourier-transformed contains oscillation data, both resolutions are equal $\Delta R_{data} = \Delta R_{FFT}$. However, the absolute positions of the available bins spaced by ΔR_{FFT} may not correspond to the positions of the actual frequencies constituting the oscillation spectrum. In this case, one peak may be split over two or more bins and the result may hence be obscured. It is therefore better to artificially increase ΔR_{FFT} so that the available number of bins is high enough not to reduce the read-off accuracy. This is usually accomplished by zero-padding the signal: adding data-points with the value zero to the signal's ends such as to make it longer. In this case however, the field range over which data points are available is longer than the range really containing oscillatory information because at very low fields oscillations cannot be observed. It is therefore convenient to just start the Fourier transformation from a lower minimum field than necessary to cover all oscillations. In other words, instead

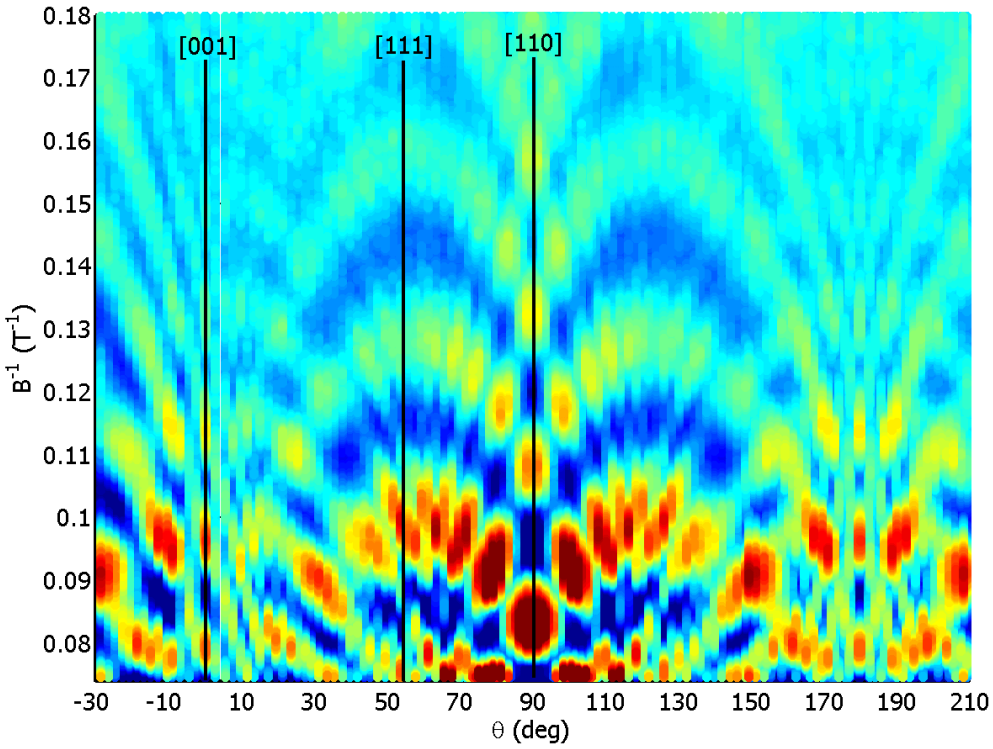

(a) $x_{\mathrm{Tl}} = 0.2\%$.

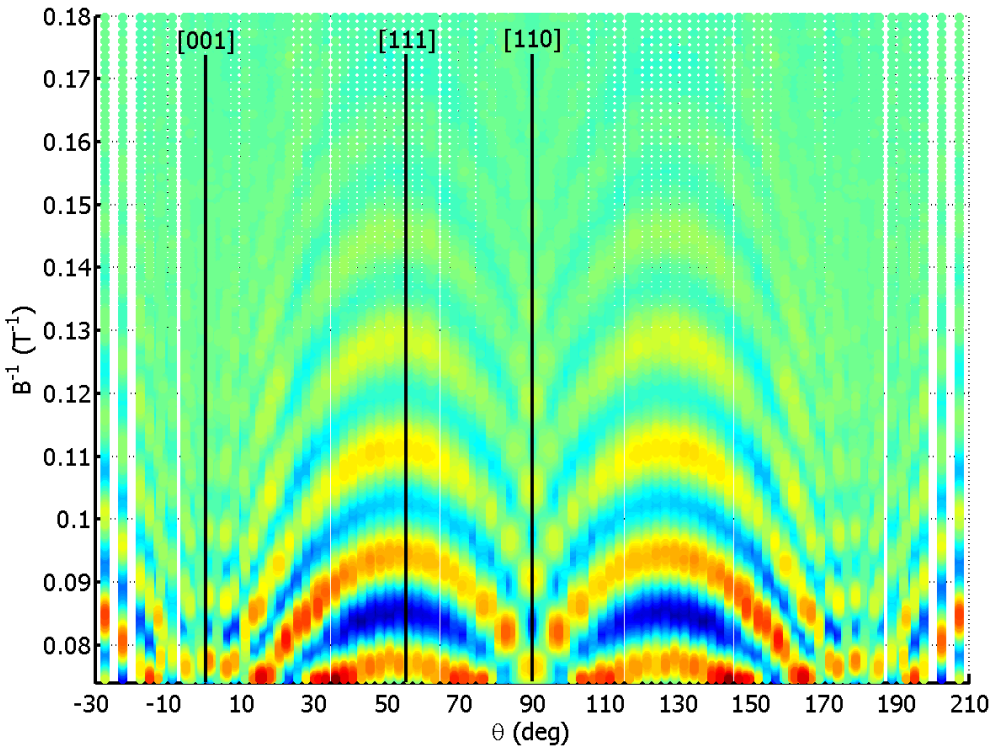

(b) $x_{\mathrm{Tl}} = 0.3\%$.

Figure 5.5.: 3D representation of SdH spectra with an angle spacing of 2° for $x_{\mathrm{Tl}} = 0.2\%$ and 2.5° for $x_{\mathrm{Tl}} = 0.3\%$. Inverse magnetic field is plotted over field angle θ, the colour scale shows the resistivity value after background substraction as explained in section 2.1. The scaling is chosen such that the red end of the spectrum corresponds to the highest peak in $\Delta\rho$ while the blue end corresponds to the lowest trough. The scales of the two panels are not the same. The upper panel shows more structures than the lower panel because of the mobility being higher for lower Tl-content.

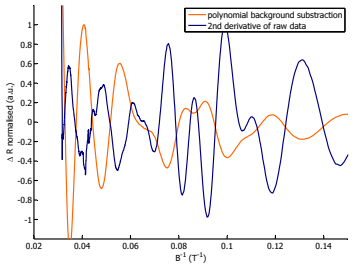

(a) $x_{\mathrm{Tl}} = 0.2\,\%$ oscillations.

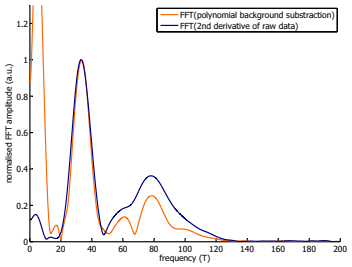

(b) $x_{\mathrm{Tl}} = 0.2\,\%$ Fourier transform.

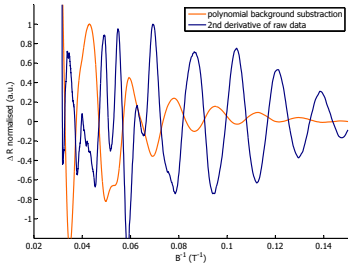

(c) $x_{\mathrm{Tl}} = 0.3\,\%$ oscillations.

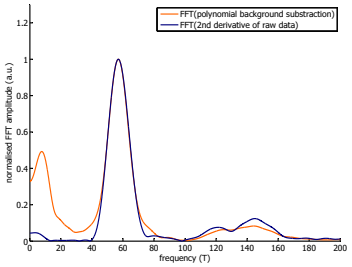

(d) $x_{\mathrm{Tl}} = 0.3\,\%$ Fourier transform.

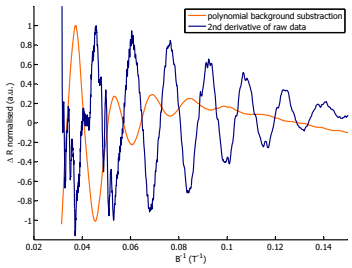

(e) $x_{\mathrm{Tl}} = 0.4\,\%$ oscillations.

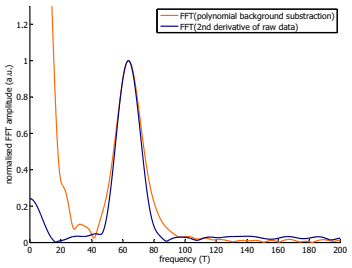

(f) $x_{\mathrm{Tl}} = 0.4\,\%$ Fourier transform.

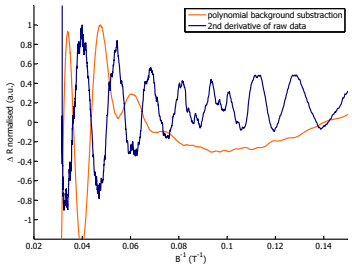

(g) $x_{\mathrm{Tl}} = 0.55\,\%$ oscillations.

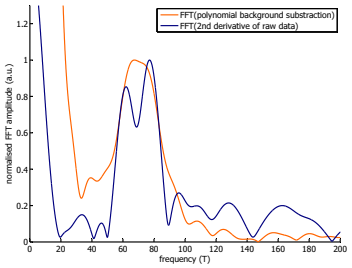

(h) $x_{\mathrm{Tl}} = 0.55\,\%$ Fourier transform.

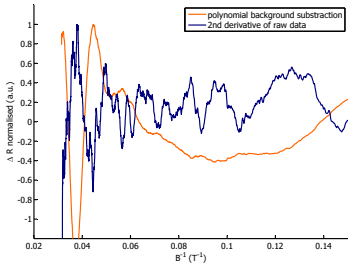

(i) $x_{\mathrm{Tl}} = 0.7\,\%$ oscillations.

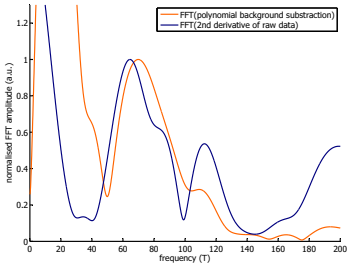

(j) $x_{\mathrm{Tl}} = 0.7\,\%$ Fourier transform.

Figure 5.6.: Comparison showing differences in Fourier resolution between samples and background removal methods. All panels show data for $\mathbf{B} \parallel [111]$, or the closest dataset available to this direction given by experimental angle step size.

of zero-padding the signal, noise from the low field range is added to the used signal. This method additionally ensures that all oscillation information, even that not visible to the bare eye, is used for the frequency spectrum. The frequencies resulting from the Fourier-transformation are not altered by this process because the frequencies associated with the noise are much higher than those stemming from the quantum oscillations, thereby hardly affecting the physically interesting frequency range.

Before calculating the Fourier transform, the script shown in appendix A.1 applies a windowing function to the data. This is necessary because of the finiteness of the data section put into the algorithm. The *Fast Fourier Transform* (FFT) algorithm assumes that this piece of data is one period of a periodic signal. The two endpoints of the waveform are interpreted as if though they were connected together. This may result in a truncated waveform with spectral characteristics that are different from those of the original data. Applying a window function gets rid of this discontinuity and can increase the resolution of the frequency spectrum. The window used here, the so-called Hann-window, is the common choice for cases where one complete period of the signal would be longer than the applied window. The coefficients of a Hann-window with length L are computed as

$$w(n) = 0.5\left(1 - \cos\left(2\pi\frac{n}{N}\right)\right), \quad 0 \leq n \leq N, \tag{5.10}$$

where $L = N + 1$ and the result is a column vector that can be multiplied with a data vector of length L to apply the windowing effect. This choice of window leads to an increased frequency resolution but leads to some spectral leakage (peaks spreading out over neighbouring bins) and hence to false-positives in the read-off of frequencies from the FFT-spectrum. It is partly because of this that there are many points in the frequency spectra of the higher doped samples that could not be identified as stemming from any Fermi surface element. They are mere artefacts of the process of Fourier transformation and could not be distinguished from real peaks because of the low amplitude of the latter in these samples.

Looking at the resulting frequency spectra disclosed two weaknesses of the procedure of subtracting a polynomial background, both related to the fact that a single fit to the whole field range does not do the data justice. Because of this, on the one hand some of the weaker oscillation peaks at lower field values are suppressed or even overwritten by the subtraction process, while on the other hand low frequency peaks corresponding to the curvature of the polynomial background appear as artefacts in the Fourier transformed spectrum. Because of these issues with the background fit, the second derivative of the raw data is used as a complimentary data base for further evaluation. By deriving the data twice, all linear and quadratic parts of the signal disappear while the oscillatory components survive. With this, more oscillation periods can be used for analysis and less artificial low frequencies are introduced. However, small fluctuations at low field values stemming from noise in the raw data can be magnified by this approach. In order to increase the reliability of the analysis, both methods were applied to the data and the results compared. Only frequencies found in the Fourier spectra of both approaches were accepted for comparison to the model. The direct comparison of Fourier spectra corresponding to the same raw data processed in the two different ways confirms that the polynomial background is unfit to reproduce the weaker peaks present in the raw data. Figure 5.6 shows the oscillations in inverse field as extracted with the two methods for all five samples and how the resolution of the Fourier transform is slightly affected by this. All the data shown there was taken with $\mathbf{B} \parallel [111]$ (or as close to this configuration as possible within the experimental resolution). In this region, were $\mathbf{B}$ is almost parallel to the A ellipsoid's major axis, the frequency is almost independent of the precise angle as will be discussed below. Because of this, angle offsets of the order of a few degrees do not affect the oscillation spectra in this area much.

Just like figure 5.5, figure 5.6 is a clear manifestation of decreasing mobility with increasing doping. While a lot of oscillation periods can be observed for $x_{\mathrm{Tl}} = 0.2\%$, it is difficult to find more than two or three peaks for $x_{\mathrm{Tl}} = 0.7\%$. However, in all five cases the data was sufficient for extracting the frequency corresponding to the minimum cross section of the L-point pockets, F^L_{min}. The exact values are given in table 5.1. Figure 5.7(a) shows how F^L_{min} evolves as a function of carrier concentration. The combination of data from this work with information from reference [40] allows to follow the growth of the L-pockets between 0.4 and $90 \cdot 10^{18}$ holes per cm^3 and shows a smooth evolution of the minimum cross section. Tl-doping does not seem to alter the band structure significantly as compared to vacancy-doping; the last vacancy-doped point and the first Tl-doped point ($x_{\mathrm{Tl}} = 0.2\%$) lying in close proximity of each other without calling for a jump or discontinuity in the pocket growth.

The carrier range of PbTe probed in the literature extends to $11 \cdot 10^{18}$ holes per cm^3 and the L-ellipsoidal model is found to hold up to this value. Burke *et al.* analyse one sample with higher carrier density and find its Fermi surface to be "non-ellipsoidal" without specifying this further. Older band-calculations [66–68] for two-band cases agree with this finding and suggest that the pockets become more cylindrical in shape as the doping surpasses a certain level between 10 and $50 \cdot 10^{18}\,\mathrm{cm}^{-3}$. It is one of the quests of this work to follow the evolution of the Fermi surface into this region and beyond. This means not only the search for possible new components of the Fermi surface but also exploring the limits of the ellipsoidal description of the L-pockets.

As a starting point, the lowest Tl-doped sample of $x_{\mathrm{Tl}} = 0.2\%$ serves as a connector to Burke's data range because its Hall carrier concentration of $15 \cdot 10^{18}\,\mathrm{cm}^{-3}$ is very close to their last ellipsoidal sample at $11 \cdot 10^{18}\,\mathrm{cm}^{-3}$. As ellipsoids of revolution are a simple geometrical form the expected oscillation frequencies for all four ellipsoids at a magnetic field orientation $\mathbf{B}(\theta)$ are easily calculated. Imagining an ellipsoid of revolution with its axes aligned with those of the Cartesian coordinate system such that the major axis is parallel to the z-direction, the radius r in the xy-plane at any height s along the z-axis is given as $r(s) = a\sqrt{1 - \frac{s}{c}}$, where a and c are the lengths of the spheroids' semi-axes. If a magnetic field is applied to this object, the resulting cross section is of 2D-ellipsoidal form in all cases. One semi-axis of this ellipsoidal cross section is always a, the other one, b, depends on the angle ζ between field and the spheroids major axis. b can be expressed through r or s as $b = r/\cos\zeta = s/\sin\zeta$. Combining this geometrical information allows to calculate the cross section area A depending on ζ:

$$A = \sqrt{\frac{a^2\pi^2}{\frac{\cos^2\zeta}{a^2} + \frac{\sin^2\zeta}{c^2}}}. \tag{5.11}$$

With the help of Onsager's relation (2.18), the minimum cross section area $A_{min} = \pi a^2$ can be replaced by the minimum oscillation frequency. By further replacing c with the help of $K = (c/a)^2$, the useful result

$$F(\zeta) = F_{\min}\sqrt{\frac{1}{\cos^2\zeta + K^{-1}\sin^2\zeta}} \tag{5.12}$$

is deduced. From this, the frequencies for all angles can be calculated if the minimum frequency and the geometrical factor K are known. It is also possible to make predictions for the frequencies without knowing $F_{\min}$ if the carrier concentration and the shape of the ellipsoids is known. For this, the minor semi-axis of the spheroid is calculated from the carrier density as will be explained below in equation (5.17), yielding

$$a = \sqrt[3]{\frac{3\pi^2 p}{4K^{-1}}}. \tag{5.13}$$

Then, the predicted frequencies of the K-ellipsoidal model are

$$F(\zeta) = \frac{\hbar}{2\mathrm{e}}\left(\frac{3\pi^2}{4K^{-1}}\right)^{2/3}\sqrt{\frac{1}{\cos^2\zeta + K^{-1}\sin^2\zeta}}. \tag{5.14}$$

These equations can be customised to the different ellipsoids in PbTe by replacing the general angle ζ by the actual angles found between $\mathbf{B}(\theta)$ and L-ellipsoids A, B and C. If $\mathbf{c}$ is the vector describing the ellipsoids major axis, then

$$\zeta = \frac{\mathbf{c}\cdot\mathbf{B}}{|\mathbf{c}|\cdot|\mathbf{B}|}. \tag{5.15}$$

For the ideal magnetic field given in equation (5.4) (without misalignment), this results in the following expressions:

$$\begin{aligned}
\zeta_A &= \arccos\left(\frac{\sqrt{2}\sin\theta + \cos\theta}{\sqrt{3}}\right),\\
\zeta_B &= \arccos\left(\frac{-\sqrt{2}\sin\theta + \cos\theta}{\sqrt{3}}\right),\\
\zeta_C &= \arccos\left(\frac{\cos\theta}{\sqrt{3}}\right).
\end{aligned} \tag{5.16}$$

Similar equations can be derived for the misaligned case using equations (5.5) as a basis. It is important to note that in this case the out-of-plane ellipsoids C1 and C2 are no longer degenerate and may produce different oscillation frequencies. An example for this will be shown at the end of the section. Appendix A.2 contains a short Matlab-script allowing to plot all ellipsoidal model curves used in the following with the possibility to choose the misalignment parameters ϵ_{off}, ϵ_1 and ϵ_2.

Because F_{min} can be determined quite accurately directly from the oscillation spectra at single angles, K remains the only fitting parameter in equation (5.12). In the sample with $x_{\text{Tl}} = 0.2\%$ it was possible to follow the oscillation branches stemming from all three ellipsoid types over the whole θ-range. The field was swept between -32 and 32 T on this sample 23 times between -5° and 100° with a regular stepsize of 5°. Every dataset was symmetrised, processed and Fourier transformed as described above and shown in figure 5.6. The peaks read off in these 23 Fourier transformations correspond to the data points in figure 5.8(a). The data points have been coloured for orientation purposes where the colour corresponds to the calculated line closest to the point. In this case, the misalignment errors seems to have been small enough not to affect the data-model agreement within the experimental resolution.

The ellipsoidal model was fit to all points simultaneously using Matlab's `lsqnonlin`. For a minimum frequency of $F_{\text{min}} = 33.8\,\text{T}$ this resulted in $K = 13.8 \pm 0.4$ which is in very good agreement with the values of 13 and 13.5 found by Burke *et al.*. It can hence be confirmed that firstly, doping with Tl in itself does not affect the Fermi surface of PbTe and that secondly, the ellipsoidal model holds at least up to a Hall carrier density of $15 \cdot 10^{18}\,\text{cm}^{-3}$.

The mobility restrictions discussed in section 5.1 impose severe restrictions on exploring the further evolution of the L-pockets at higher doping. In all measurements it was found that frequencies above 130 T could not be observed experimentally. In the case of $x_{\text{Tl}} = 0.2\%$ with a minimum frequency of 34 T the maximum frequency is to be expected around at $34\,\text{T} \cdot \sqrt{13} = 122\,\text{T}$ for $K = 13$, hence within the experimental window. For the sample with $x_{\text{Tl}} = 0.3\%$ and $p_{\text{Hall}} = 46 \cdot 10^{18}\,\text{cm}^{-3}$ however, the minimum frequency was found at 58 T which would correspond to a maximum frequency of 209 T within the ellipsoidal model. This is not observable and it is therefore difficult to make statements about the validity of the model. Figuratively speaking, we can see the waist of the pockets but not their ends. Experimentally there is no way of knowing whether they are formed compliant with the ellipsoidal model, whether they are more pointy or more flat or even more complicated in shape.

However, a deviation from $K = 13$ ellipsoids is already evident from the available data. Figure 5.8(b) shows all data points extracted from the measurements on $x_{\text{Tl}} = 0.3\%$ which were equally conducted at 23 angles between -5° and 100°. The data points believed to stem from the C-pockets start to lie significantly above the model line for $\theta > 25°$. This is evidence that the suggested transformation of ellipsoidal pockets into more cylindrical objects is close to reality: the measured frequencies lie above the model line meaning that the real k-space object is more rod-like than the expected $K = 13$ ellipsoid. Indeed, comparing the data points to calculated lines corresponding to ellipsoids with $K \approx 60$ yields a much better fit (figure 5.8(c)). It is of course very unlikely that the real shape of the pockets resembles to ellipsoids with such a large anisotropy because firstly this would not be coherent with the shapes found at slightly lower doping and secondly these pockets would be able to hold almost twice as many carriers as found in Hall effect measurements. However, as we cannot map the pockets in all directions, it is only the experimentally accessible part that is believed to resemble the corresponding part of a $K = 60$ ellipsoid. An idea for modelling these non-ellipsoidal pockets is visualised in figure 5.8(d) and uses the curvature of a $K = 60$ ellipsoid as suggested by the fit but the length of a $K = 13$ ellipsoid for continuity reasons connecting this sample to the lower doping range. Additionally, complete $K = 60$ ellipsoids would be able to hold far more carriers than found in the Hall experiments, thus eliminating this possibility. Following experimental evidence the last sketch in this figure may represent the non-ellipsoidal pockets at intermediate and higher doping. However, there is no way of finding out what the far ends of the pockets look like using SdH-experiments up to 32 T only.

Even if the magnetic field available here is not high enough to probe the complete shape of the L-pockets, there is one clear indicator showing that the L-ellipsoidal model with $K = 13$ can no longer be sufficient to describe the material at $p_{\text{Hall}} = 38 \cdot 10^{18}\,\text{cm}^{-3}$ and above: the fact that the $K = 13$ model together with the experimentally determined minimum frequencies cannot account for all carriers found in the Hall effect measurements in the samples with higher doping levels. In principal, if the volume of a Fermi surface is known, the number of carriers it

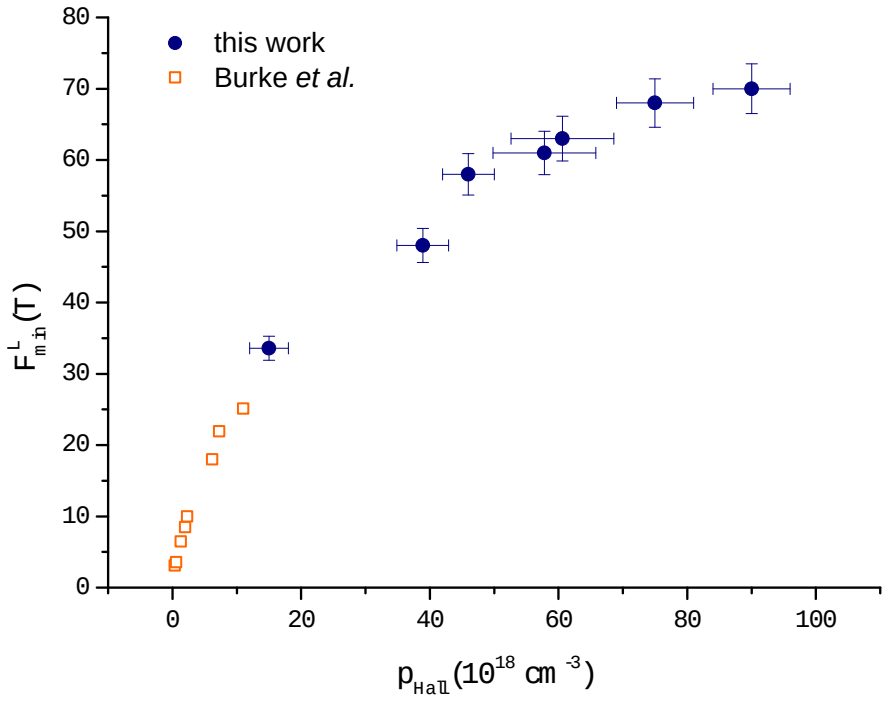

(a) Minimum oscillation frequency from the L-pockets as a function of Hall carrier density. Combination of data from [40] and new data.

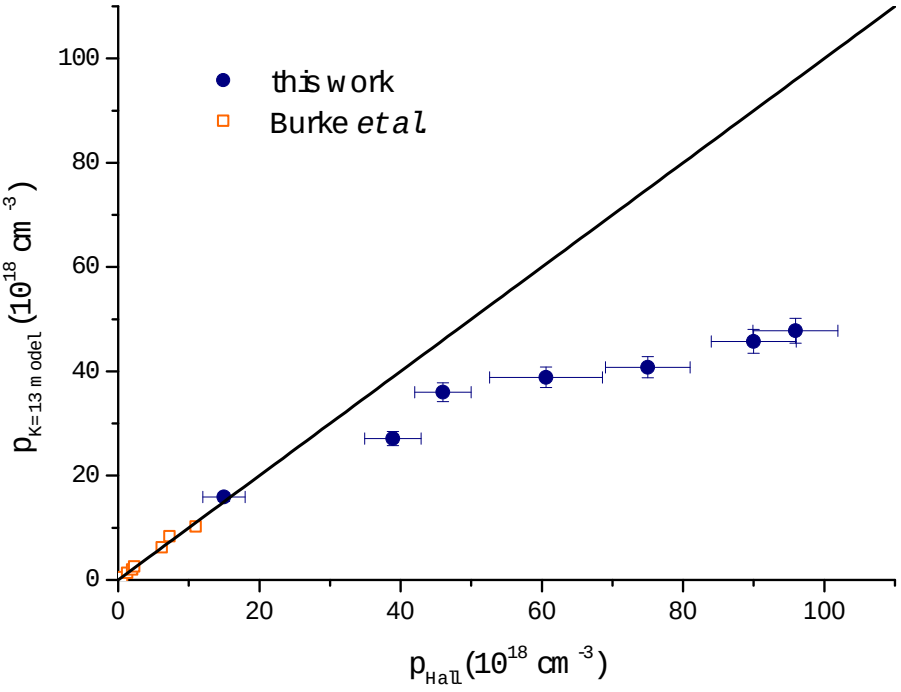

(b) Comparison between carrier concentration calculated from $F_{\min}$ with the $K = 13$ model and Hall carrier density. The black line shows ideal agreement, $p_{\mathrm{Hall}} = p_{model}$. The model does poorly above $x_{\mathrm{Tl}} \geq 0.25\%$, the second data point from this work.

Figure 5.7.: Evolution of the L-pockets as a function of doping.

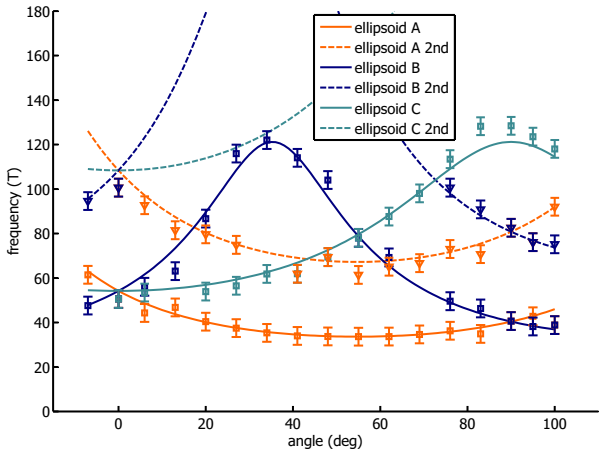

(a) $x_{\mathrm{Tl}} = 0.2\%$. Lines correspond to a $K = 13$ ellipsoidal model.

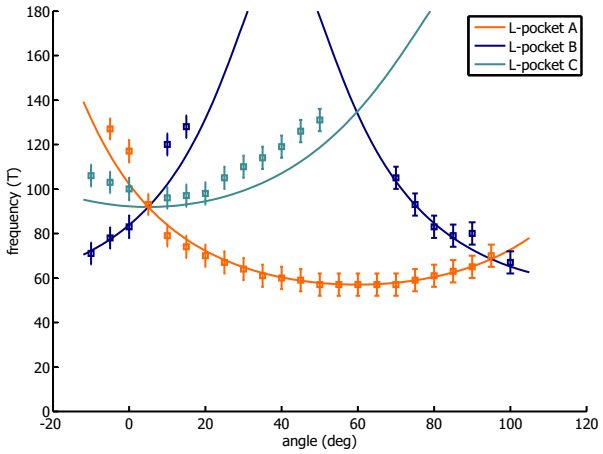

(b) $x_{\mathrm{Tl}} = 0.3\%$. Lines correspond to a $K = 13$ ellipsoidal model.

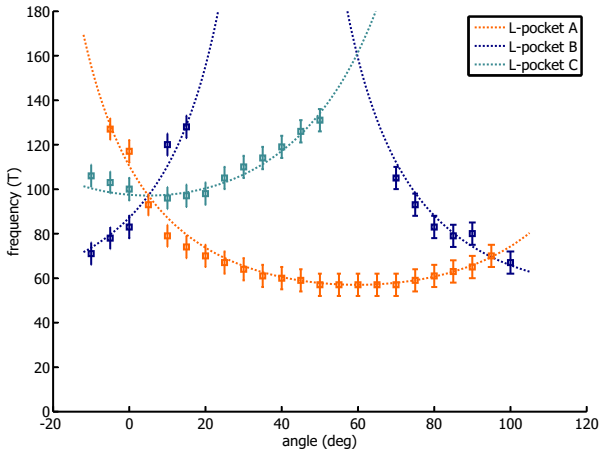

(c) $x_{\mathrm{Tl}} = 0.3\%$. Lines correspond to a $K = 60$ ellipsoidal model.

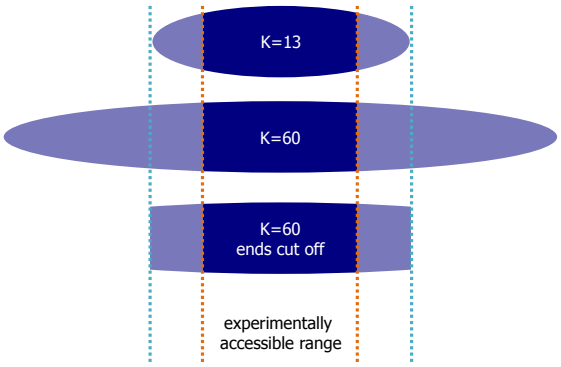

(d) Heuristic construction of a non-ellipsoidal Fermi surface pocket using the curvature of a $K = 60$ ellipsoid and the length of a $K = 13$ ellipsoid. Only part of the shape is accessible to experiment.

Figure 5.8.: Peaks in the Fourier transform of 23 oscillation spectra as a function of magnetic field orientation for $x_{\mathrm{Tl}} = 0.2\%$ and $x_{\mathrm{Tl}} = 0.3\%$. Some of the peaks were identified to be second harmonics of lower frequencies as indicated. Comparison to ellipsoidal models with different anisotropies.

is able to house can be calculated. In the case of an ellipsoidal model, the volume of the four pockets is calculated from the minimum oscillation frequency as follows:

$$V_{FS} = 4 \cdot \frac{4\pi}{3} a^3 \sqrt{K} = \frac{16\pi}{3} \left(\sqrt{\frac{4\pi e F_{\min}}{\hbar}} \right)^3 \sqrt{K}, \tag{5.17}$$

where Onsager's relation (2.18) was used. The **k**-space volume occupied by every electronic state is given by $(2\pi)^3$ and allows to calculate the real space carrier density p from the **k**-space Fermi surface volume:

$$p = 2 \cdot \frac{V_{FS}}{8\pi^3}. \tag{5.18}$$

A factor of 2 has been included to account for the spin quantum number. In figure 5.7(b) the number of carriers that ellipsoids with an anisotropy of $K = 13$ can hold is calculated from the observed minimum oscillation frequencies and compared to the direct measurement of the Hall carrier density. This shows that the $K = 13$ model explains the carrier numbers in all of Burke's samples and also in Tl:PbTe up to $x_{\mathrm{Tl}} = 0.2\%$ ($p_{\mathrm{Hall}} = 15 \cdot 10^{18}\,\mathrm{cm}^{-3}$). Above

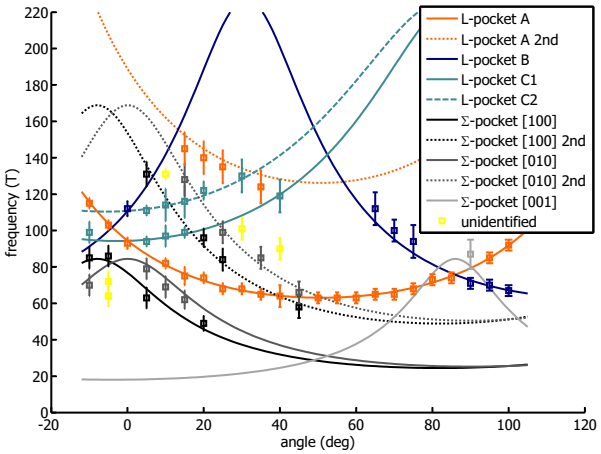

(a) $x_{\mathrm{Tl}} = 0.4\%$.

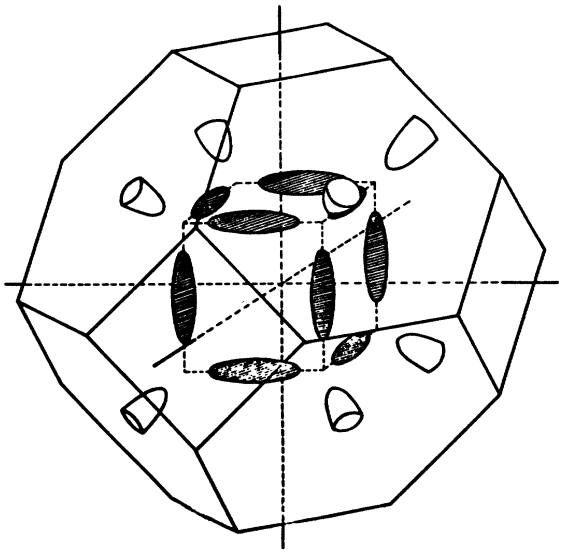

(b) Fermi surface of high-temperature PbTe as proposed by reference [44].

Figure 5.9.: Peaks in the Fourier transform of 23 oscillation spectra as a function of magnetic field orientation for $x_{\mathrm{Tl}} = 0.4\%$ and two-component Fermi surface model. Colourful lines correspond to L-ellipsoids with $K = 13$, grey scale lines correspond to Σ-ellipsoids with $K = 22$.

this value, the experimentally measured carrier concentration is higher than the one calculated from the minimum oscillation frequency and the $K = 13$ model. It is hence safe to say that some alteration of the Fermi surface takes place above $15 \cdot 10^{18}\,\mathrm{cm}^{-3}$. This may be the appearance of additional pockets, a change in the shape of the L-pockets or a combination of both. In the following section, evidence for additional pockets is presented and in chapter 6 more recent band structure calculations produced for comparison with this work are exploited to gain further insight into the change of shape of the L-pockets.

5.2.3 Additional Fermi surface components at higher doping?

When moving on to the samples with $x_{\mathrm{Tl}} = [0.4\%, 0.55\%, 0.7\%]$, the B and C branches vanish from sight even earlier than in the case of $x_{\mathrm{Tl}} = 0.3\%$ discussed above. However, around the high symmetry direction $\mathbf{B} \parallel [001]$, where the frequencies from all three types of L-ellipsoids are very close to each other, the oscillation spectra for $x_{\mathrm{Tl}} = 0.4\%$ show additional frequencies that cannot be explained within the L-ellipsoidal model. As shown in figure 5.9(a) for $x_{\mathrm{Tl}} = 0.4\%$ ($p_{\mathrm{Hall}} = 61 \cdot 10^{18}\,\mathrm{cm}^{-3}$), frequencies below the major frequencies stemming from the dominant L-pockets appear in six spectra around $\mathbf{B} \parallel [001]$. This completely new feature as compared to the sample with $x_{\mathrm{Tl}} = 0.3\%$ immediately inspires the thought of a new Fermi surface component being filled. A readily available idea for this is found in the Fermi surface first suggested by Sitter for PbTe at temperatures above 300 K: a model with four pockets at the L-points (as for lower doping) and an additional set of twelve ellipsoidal pockets at the Σ-points of the fcc-Brillouin zone as introduced in section 3.1. The Σ point is located between Γ- and K-points, halfway between the middle of the zone and the edges between two hexagonal zone faces. The original suggestion by Sitter *et al.* [44] is shown in figure 5.9(b).

Equation (5.12) which was used to describe the signals from the L-pockets can equally be employed to model Σ-pocket oscillation frequencies if the right expressions are inserted instead of ζ. In principal, there are three sets of four different Σ-pockets: those with major axis parallel to [100], [010] and [001]. Because we move the

field vector from [110] to [001] during the course of our measurement, the pockets along [100] and [010] are degenerate for all angles θ if there is no misalignment. In the ideally aligned case the angles are

$$\zeta_{[100]} = \zeta_{[010]} = \arccos\left(\frac{\sin\theta}{\sqrt{2}}\right),$$
$$\zeta_{[001]} = \theta\,. \tag{5.19}$$

Like for the L-pockets, these expressions are slightly altered in the misaligned case and the two degenerate sets of pockets can split into distinct branches, as shown in figure 5.9(a). The expressions used to plot the model lines can be found in appendix A.2. While the coloured lines describe the L-ellipsoidal model with $K = 13$ as before, the new grey scale lines are derived using the misaligned version of equations (5.19). For this sample it was necessary for the first time to make use of the misalignment corrections to the model as is most clearly shown by the two C-branches (turquoise). These were used to determine the misalignment angles $\epsilon_{\text{off}} = 4°$, $\epsilon_1 = -1°$ and $\epsilon_2 = 4°$. When this correction was applied to the Σ-pocket equations as well, the extended model could account for the vast majority of peaks found in the Fourier spectra. Some unidentified peaks remain, however, and are coloured in yellow in figure 5.9(a). These may be artefacts of the Fourier transformation because a Hamming-window was applied to the raw data with the aim of increasing the Fourier resolution. The trade-off for this improvement is however the introduction of false positives that cannot be distinguished from real peaks. The Σ-signal on the other hand is not believed to be a pure artefact because of the continuity with which it appears over several neighbouring spectra. In fact, enough data points could be collected from the Σ-pockets to fit ellipsoidal curves to them, yielding $F^{\Sigma}_{\text{min}} = 18$ and $K_{\Sigma} = 22$ with an accuracy of 20%.

However, it is a serious threat to this result that the signature of the new pockets could not be traced into the angle-region where frequencies below 40 T are expected. A priori one would expect these frequencies to be observed more easily because of the higher mobilities associated with the smaller cross section, but even though several different methods to remove the background were applied, no robust sign of them showed. The approaches included the polynomial background subtraction an the second derivative as discussed above as well as taking the third derivative of the raw data. The third derivative is expected to perform even better than the second derivative in the low frequency region and indeed with this frequency peaks below 40 T were observed. Yet, none of them were found to be robust in change of analysis parameters such as the field range put into the Fourier algorithm or the number of points for which a moving average was calculated during data smoothing. Therefore they are not displayed in figure 5.9(a). It is unclear why the Σ-pocket signature shows up only in a narrow range around $\mathbf{B} \parallel [001]$ and not elsewhere, but it may be down to data quality.

In $x_{\text{Tl}} = [0.55\%, 0.7\%]$ the frequency resolution is yet decreased as compared to $x_{\text{Tl}} = 0.4\%$. This means that a lot of false positive peaks appear in the Fourier spectra as discussed above. Figure 5.10 shows all of the peaks extracted from the single spectra without prior selection. The error bars have to be assumed to be larger than for $x_{\text{Tl}} = 0.4\%$ and this together with the uncertainty whether a peak can be trusted to result from an existing frequency at all makes it hard, almost futile, to test a model on them. Nevertheless, the two panels of figure 5.10 show a possible attribution of the points to the pockets they may stem from and Σ minimum frequencies were extracted from the model lines which were overlaid visually. The $x_{\text{Tl}} = 0.55\%$ sample was probed at 23 different angles between $-10°$ and $100°$, the $x_{\text{Tl}} = 0.7\%$ sample at 17 angles between $-7°$ and $100°$. The minimum frequencies guessed from the figures are $F^{\Sigma}_{\text{min}}(x_{\text{Tl}} = 0.55\%) = (23 \pm 6)\,\text{T}$ and $F^{\Sigma}_{\text{min}}(x_{\text{Tl}} = 0.7\%) = (26 \pm 7)\,\text{T}$.

Using the information about this new Fermi surface component, a second attempt to explain the position of all the Hall carriers in **k**-space can be made. Here, the L-ellipsoids are assumed to be present for all carrier concentrations and K_L is assumed to be 13 while F^{L}_{min} is extracted from the measurements. Starting from $x_{\text{Tl}} = 0.4\%$, the capacity of twelve small Σ-pockets with $K_{\Sigma} = 22$ and $F^{Sigma}_{\text{min}} = [18\,\text{T}, 23\,\text{T}, 26\,\text{T}]$ for the three last samples is added to that. As can be seen in figure 5.11, the agreement is already much better than in the first try. However, the model still falls behind the Hall count, especially at intermediate carrier concentrations. This is due to the fact that in this simple calculation, the change of shape of the L-pockets towards a cylinder which was clearly observed in the $x_{\text{Tl}} = 0.3\%$ sample (as shown in figure 5.8) is not accounted for. Cylinders can house more carriers than ellipsoids with the same minimum cross section and length because of their larger volume. Nevertheless, figure 5.11 serves as a proof of principle that a second set of pockets is needed to explain the whereabouts of the beforehand homeless carriers.

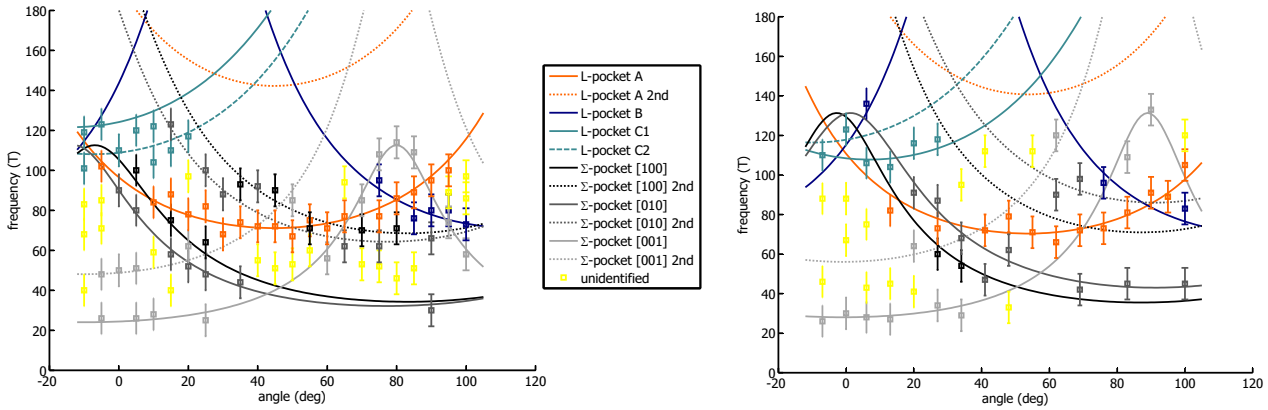

(a) $x_{\mathrm{Tl}} = 0.55\%$. (b) $x_{\mathrm{Tl}} = 0.7\%$.

Figure 5.10.: Peaks in the Fourier transform of 23 (17) oscillation spectra as a function of magnetic field orientation for $x_{\mathrm{Tl}} = 0.55\%$ ($x_{\mathrm{Tl}} = 0.7\%$) and two-component Fermi surface model. Colourful lines correspond to L-ellipsoids with $K = 13$, grey scale lines correspond to Σ-ellipsoids with $K = 22$.

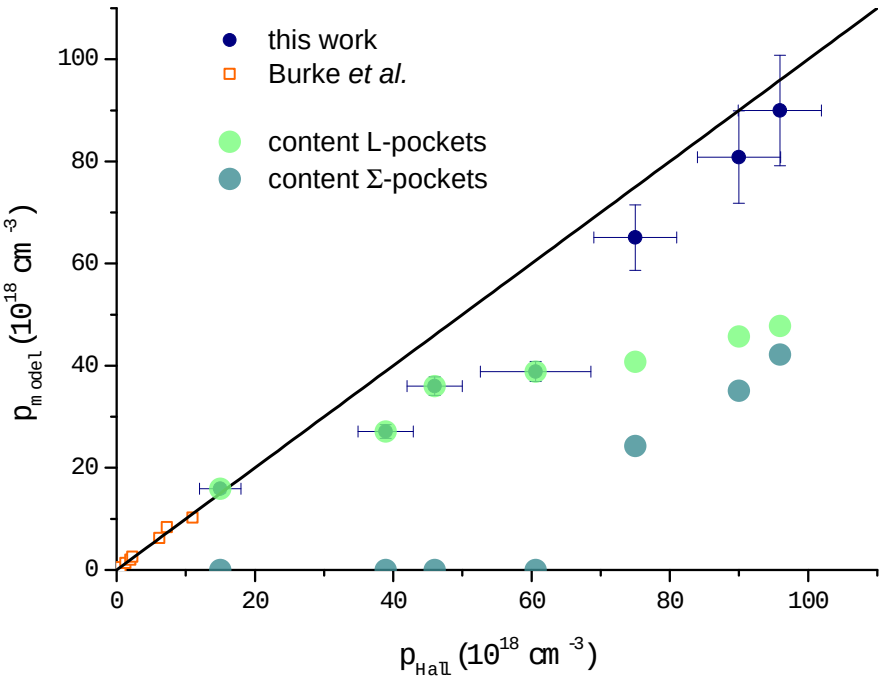

Figure 5.11.: Comparison between Hall carrier density and carrier number accounted for by a model of four L-ellipsoids with $K = 13$ at low doping and additional Σ-pockets with $K = 22$ for the last three samples. The black line shows ideal agreement, $p_{\mathrm{Hall}} = p_{model}$. The light blue and green disks show the carrier number that L- and Σ-pockets can contain separately, the blue dots are the sum of the two.

5.3 Mass and Fermi level

The effective mass of charge carriers in a solid is a concept based on the observation that in many cases electron and holes in a crystal react to external stimuli such as magnetic or electric fields as if they were free particles with an altered mass. This tensorial effective mass $m^\star$ is usually given in units of the electron mass m_e and is related to the dispersion relation $E(\mathbf{k})$ as follows:

$$\left(\frac{1}{m^\star_{ij}}\right) = \frac{1}{\hbar^2}\frac{\partial^2 E(\mathbf{k})}{\partial k_i \partial k_j}. \tag{5.20}$$

In the free electron case with its quadratic dispersion relation $E(\mathbf{k}) = \hbar^2\mathbf{k}^2/2m$ this results in a constant isotropic value but in a crystal the mass is dependent on position in k-space, orientation of the applied field and the Fermi level position in the band structure. Therefore the determination of the mass in a series of samples with different doping contains information about the band structure itself.

In the case of ellipsoidal Fermi surface pockets, the mass tensor $\mathscr{M}$ assumes diagonal form if $\mathbf{B}$ is parallel to one of the ellipsoids axes of symmetry. For the choice of $\mathbf{B}$ parallel to the major axis oriented along the z-axis we find

$$\mathscr{M} = \begin{pmatrix} m_S & 0 & 0 \\ 0 & m_S & 0 \\ 0 & 0 & m_L \end{pmatrix}, \tag{5.21}$$

where m_S and m_L are the two different components of the tensor, distinguished by the indices "small" and "large". If the cyclotronic mass was measured for a field parallel to the z-direction, according to equation (2.21), it would result in $m_{c,z} = \sqrt{m_S m_S} = m_S$. Similarly, for either of the fields parallel to x- and y-directions, the effective masses are $m_{c,x} = m_{c,y} = \sqrt{m_S m_L}$.

As the Fermi surface ellipsoids in PbTe are oriented along the [111]-type directions, a measurement of the temperature-dependent oscillation amplitudes as explained in section 2.1 with the field parallel to the [111]-direction yields the value of m_S. This value was determined for all the samples probed in this work, using either PPMS or the HFML setup (or both in some cases). m_L could not be determined experimentally because the extraction of mass values from experimental data relies on quantum oscillations just like the measurements of the Fermi surface itself do. If there are no oscillations observable for a given pocket at a given field orientation, the corresponding mass cannot be determined. However, in the ellipsoidal case, the anisotropy K translates directly from the Fermi surface pockets into the mass tensor by using $E = \hbar^2\mathbf{k}^2/2m^\star$:

$$K = \left(\frac{k_{major\ axis}}{k_{minor\ axis}}\right)^2 = \frac{m_l}{m_s}. \tag{5.22}$$

Quantum oscillation curves were recorded for $\mathbf{B} \parallel [111]$ at a variety of temperatures for Tl:PbTe with $x_\mathrm{Tl} = [0.2\%, 0.25\%, 0.3\%, 0.35\%, 0.4\%, 0.55\%, 0.7\%]$ in order to extract the minimum mass of the L-carriers. During the theoretical introduction of the mass extraction process in section 2.1, an exemplary data set stemming from $x_\mathrm{Tl} = 0.3\%$ was shown in figure 2.4. This data set is easy to evaluate because on the one hand a lot of oscillation periods could be observed, offering the opportunity to verify the mass value fitted to the amplitude decrease of one peak on several others, and on the other there is no contamination from B or C ellipsoids present below approximately 10 T. These issues complicate the analysis of the temperature-dependent oscillations when coming closer to the edges of the available doping range as will be explained below. Figure 5.12 contains the oscillation data and the partial Lisfshitz-Kosevich fit for the two extreme cases of $x_\mathrm{Tl} = 0.2\%$ and $x_\mathrm{Tl} = 0.7\%$. An overview of all temperature-dependent oscillations and the corresponding mass fits is shown in appendix B.2.

For $x_\mathrm{Tl} = 0.2\%$ the peaks at higher fields stem principally from the ellipsoid of interest for the minimum mass determination, but are nevertheless contaminated by contributions from other pockets which are beginning to become observable at these field. This becomes evident when comparing the mass values yielded by the fit to different peaks' amplitudes. The mass resulting from the first peak (highest field value) is significantly higher than that resulting from peaks at lower fields because the other pockets, which exhibit a heavier mass for this field orientation,

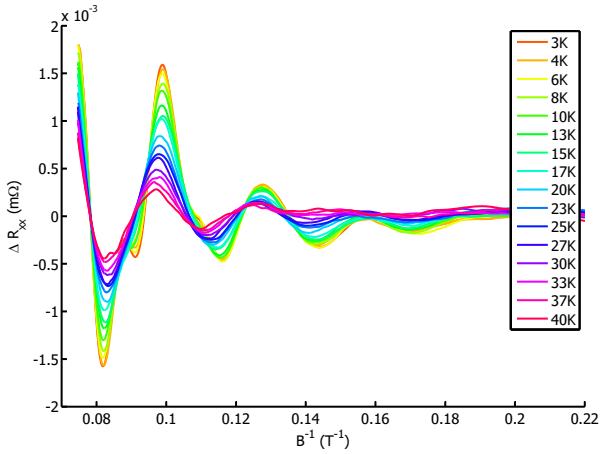

(a) $x_{\mathrm{Tl}} = 0.2\%$ oscillations.

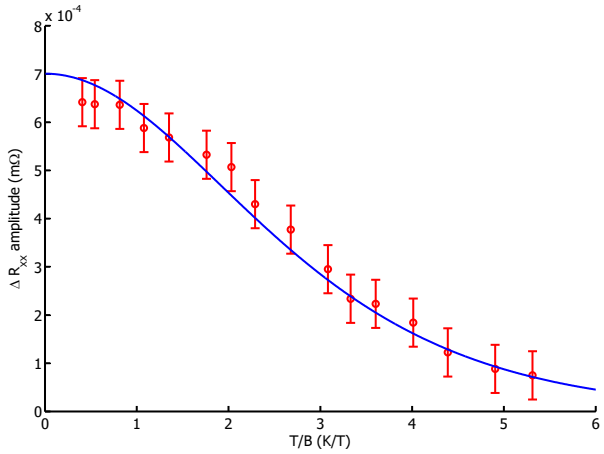

(b) $x_{\mathrm{Tl}} = 0.2\%$ Lifshitz-Kosevich-fit.

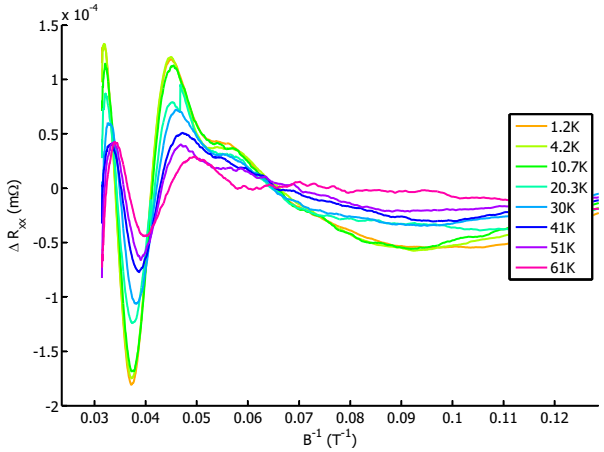

(c) $x_{\mathrm{Tl}} = 0.7\%$ oscillations.

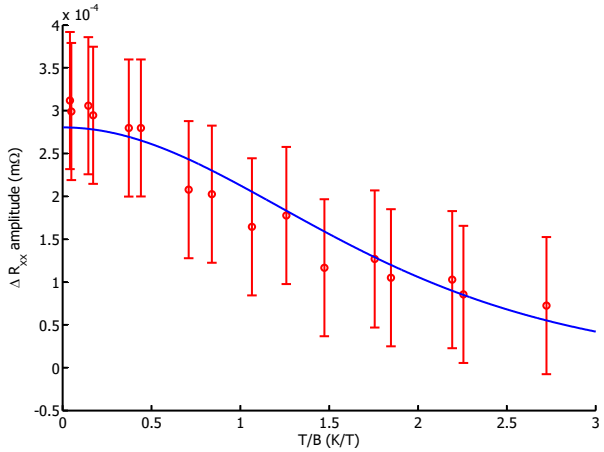

(d) $x_{\mathrm{Tl}} = 0.7\%$ Lifshitz-Kosevich-fit.

Figure 5.12.: Temperature-dependent oscillations for $\mathbf{B} \parallel [111]$ for a sample with high and a sample with low mobility. On the left side the quantum oscillations at several different temperatures are shown, on the right side the amplitudes of a chosen peak (or the difference between a peak and consecutive trough as explained in the main text) is plotted as a function of field-normalised temperature. The line is a fit of equation (2.20) to the points where m^* is the fitting parameter.

do not contribute to the signal at low fields.

For $x_{\mathrm{Tl}} = 0.7\%$ only very few oscillations could be observed. There is definitely no contamination from other pockets to be expected, but the method of simply using the peak heights at a fixed field value, as applied at lower doping, ceases to work because the extrema of the oscillations are not exactly in the same position for different temperatures and, more importantly, the background changes so much that it cannot be subtracted from all data sets in a consistent way. The processing method was hence adjusted to fitting the mass to the field-normalised difference between the first peak and the first trough. λ, as given in equation (2.20), is proportional to T/B. In the new approach of fitting the mass, instead of reading the resistance value of the oscillations at one fixed field, the peak resistance and the corresponding magnetic field are read together. This is done for a set of consecutive peaks and troughs in order to get rid of the contribution of the background. Finally, ρ_{peak}-ρ_{trough} is plotted over $(T/B_{\mathrm{peak}} + T/B_{\mathrm{trough}})/2$ and equation (2.20) is fitted to this. The error induced by averaging over two different fields is estimated to be below 5% by comparing this approach to the standard approach for the sample of $x_{\mathrm{Tl}} = 0.3\%$. It was applied to the three samples with highest doping as well as to $x_{\mathrm{Tl}} = 0.2\%$ - in the latter case, because of the contamination discussed above, the oscillations chosen for evaluation were at such low fields that the background shift had set in as well (see figure 5.12(a) at low fields).

Taking into account these difficulties, the L-pocket masses for **B** ∥ [111] were determined for seven samples of Tl:PbTe, the results being shown in table 5.1. The evolution of this mass as a function of Hall carrier concentration is shown in figure 5.13(a). Here, mass seems to increase linearly up to a carrier concentration of about $p_{\mathrm{Hall}} = 50 \cdot 10^{18}\,\mathrm{cm}^{-3}$ and approaches saturation afterwards. This is consistent with the development of the carrier number contained in the L-pockets as shown in figure 5.11, where the L-pockets begin to grow much slower starting from the same carrier density. This is equivalent to the Fermi level beginning to move lower into the band at a decreased speed - hence the effective mass as a property depended on the band curvature changes less rapidly as well.

Combining the values of F_{min} and $m^{\star}_{min}$ extracted up to now, the Fermi energy for each sample can be calculated using the general relation

$$E_F = \frac{\hbar^2 k_F^2}{2m^{\star}} = \frac{\hbar^2}{2m^{\star}} \frac{A}{\pi} = \frac{\hbar^2}{2m^{\star}} \frac{1}{\pi} \frac{2\pi e F}{\hbar}. \tag{5.23}$$

This value gives the energy distance between band edge and highest energy carrier in the 0 K limit. Figure 5.13(b) shows how this energy evolves as a function of doping. It is clear that there is almost complete saturation for $p_{\mathrm{Hall}} > 50 \cdot 10^{18}\,\mathrm{cm}^{-3}$, the Fermi level has reached a constant level and does not increase much further. This has been observed before by Matsushita [32] and agrees with the interpretation offered by Tl-disproportionation as introduced in section 3.3. As additional dopants are added to the material, they assume either of the two allowed states Tl^{+} and Tl^{3+} with equal likelihood and hence keep E_F pinned to a constant value.

While the minimum mass for the carriers in the L-pockets could be determined for all samples, mass values for the Σ-pockets are not available from these measurements. For none of the samples with higher doping level the Σ-pocket showed at **B** ∥ [111], so no temperature-dependent data is available. Even if sufficient temperature-dependent data had been taken at the HFML for a direction around **B** ∥ [001], it is unlikely that a a mass could have been extracted using the methods employed above, because for this it is necessary to relate peaks in the oscillation spectra directly to one type of pocket and follow the evolution of their amplitude in temperature. As the signal from the L-pockets is much stronger in all spectra showing additional Σ-frequencies and both frequencies are close to each other, it is difficult to identify contributions from single pockets precisely. However, the Lifshitz-Kosevich-fit can also be applied to the Fourier-transformed oscillation spectra where attribution of the peaks is much easier. Even though this method introduces an additional source of errors into the process, it would be interesting to measure a temperature-dependent data set for **B** ∥ [001] on an $x_{\mathrm{Tl}} = 0.4\%$ sample to get an idea of the masses of the Σ-carriers. The field directions at which signs of the second pockets were observed here correspond to the direction where they would display their heaviest mass in an ellipsoidal case, additionally making their observation and especially the mass determination more difficult because higher masses translate into lower mobility and faster amplitude-decrease in temperature.

5.4 Superconductivity

All samples with $x_{\mathrm{Tl}} \geq 0.3\%$ were probed for a superconducting transition in the dilution fridge. The thermometer on the sample holder showed temperatures below 28 mK, but with the set-up used there is no way of knowing the actual temperatures of the samples. The lowest transition temperature measured up to now with the same dilution fridge and sample holder on a sample of STO with comparable contact resistance was around 40 mK, so this temperature can realistically be expected to have been reached during the experiments on Tl:PbTe as well. Down to this temperature, no transition into the superconducting state was observed for any sample with $x_{\mathrm{Tl}} \leq 0.4\%$ and no superconducting fluctuations were observed either. Matsushita *et al.* [32] measured similar samples in a different set-up down to 10 mK and indeed found transitions in $x_{\mathrm{Tl}} = 0.3\%$ and $x_{\mathrm{Tl}} = 0.4\%$ at 13 mK and around 50 mK respectively. Of course these measurements were not performed on the identical samples used here and the nominal x_{Tl} values carry a large relative error so that this does not imply that values below 50 mK were not reached in the measurements discussed here. While Matsushita *et al.* found a superconducting transition in all those samples that also displayed a low-temperature resistivity upturn, the so-called Kondo-upturn, this link cannot be established in the same firm way with the data available in this project. The issue, however, draws attention to the general problem that just because no superconducting ground state can be observed this does not mean that there is none. Extrapolation from finite transition temperatures at higher doping into the low-doped region where no transitions are observed are therefore a necessary tool for making statements about critical doping levels or carrier concentrations for the onset of superconductivity and will be applied below.

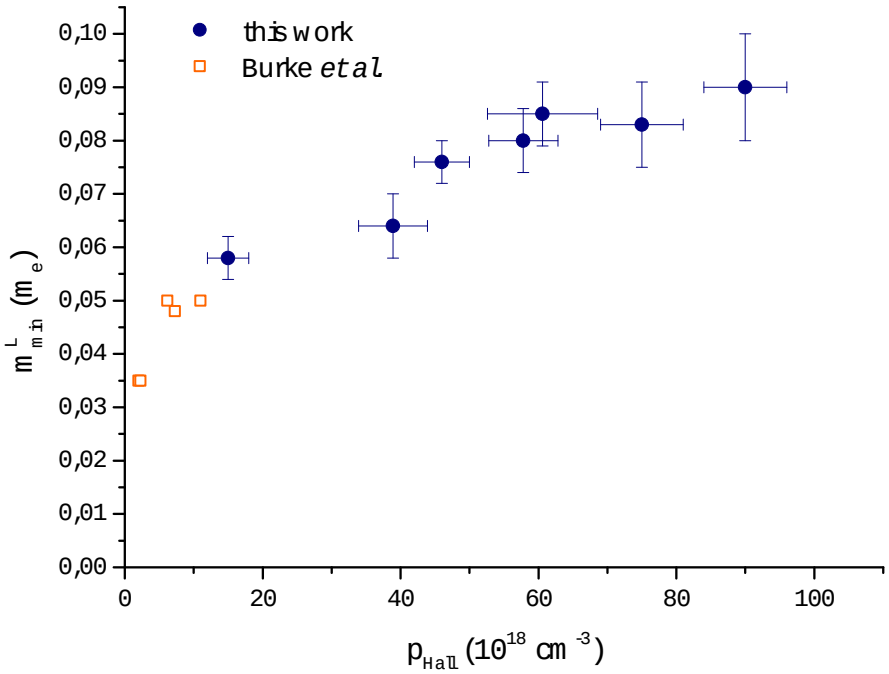

(a) Effective mass as a function of Hall carrier concentration.

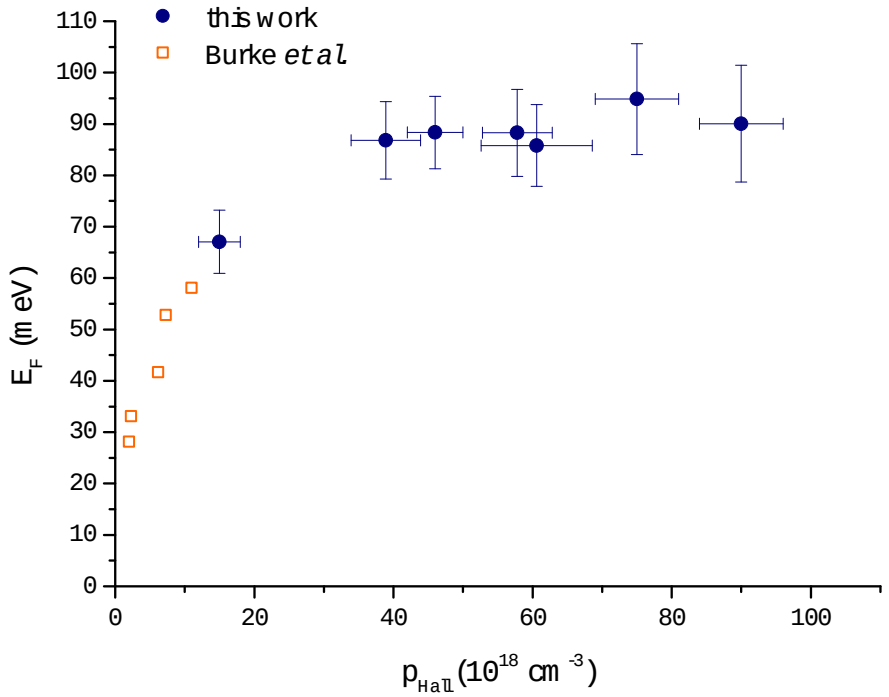

(b) Fermi level as a function of Hall carrier concentration.

Figure 5.13.: Evolution of mass and Fermi energy with increasing doping. Combination of data from this work (blue dots) and data from reference [40] (orange squares).

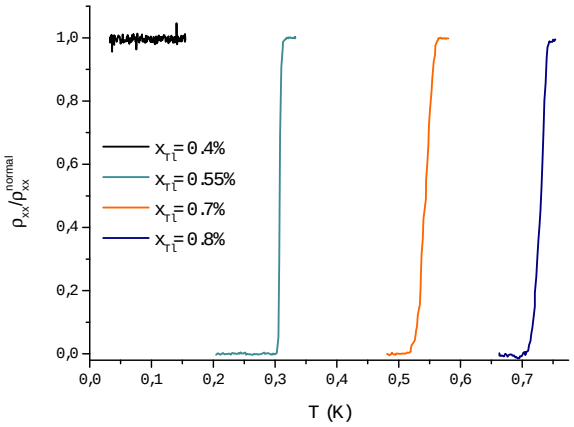

(a) $\rho(T)$ for samples with $x_{\mathrm{Tl}} = [0.4\%, 0.55\%, 0.7\%, 0.8\%]$ normalised to the resisitivity at 1 K.

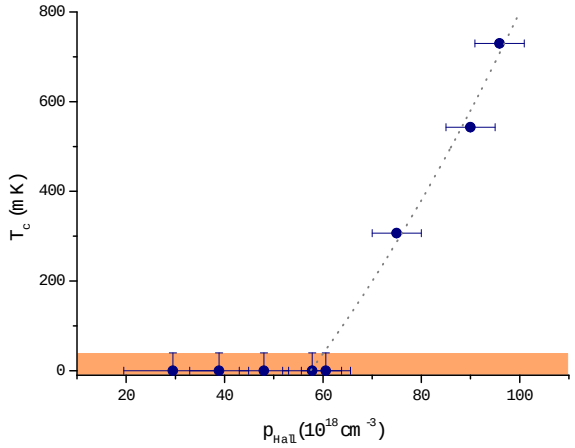

(b) T_c as a function of Hall carrier density. The dotted line is drawn to guide the eye and is a possible extrapolation into the inaccessible temperature range.

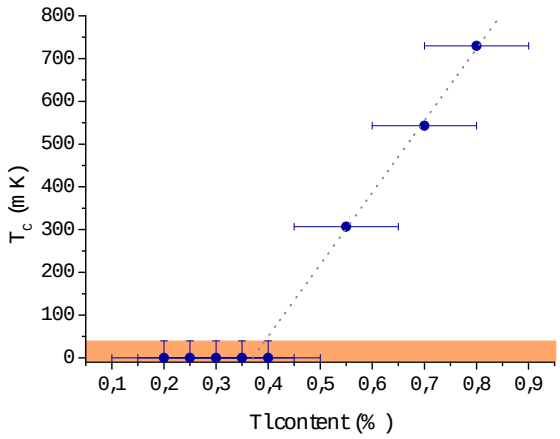

(c) T_c as a function of Tl-doping. The dotted line shows a linear extrapolation into the inacessible regime.

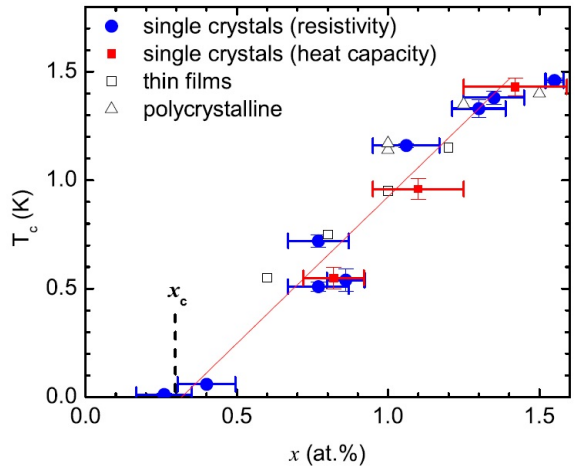

(d) T_c as a function of Tl-doping. Figure from reference [32], includes data from [69] (polycrystals) and [56] (thin films).

Figure 5.14.: Transition between normal and superconducting state in Tl:PbTe as function of Hall carrier density and Tl-doping.

Finite superconducting transition temperatures were observed in the samples with $x_{\mathrm{Tl}} = [0.55\%, 0.7\%, 0.8\%]$ and ranged from 307 mK to 730 mK. This means that within a doping range of 0.4 percentage points (between $x_{\mathrm{Tl}} = 0.4\%$ and $x_{\mathrm{Tl}} = 0.8\%$), which corresponds to a difference in carrier number of only $p_{\mathrm{Hall}} \simeq 35 \cdot 10^{18}\,\mathrm{cm}^{-3}$, the critical temperature rises by more than one order of magnitude. The critical temperatures given here equal the temperature at which the resistivity of the samples has fallen to half of its value at 1 K. The transitions observed at zero field was sharpest for the lowest doped sample with a width of $\Delta T_c = 4.6\,\mathrm{mK}$ and slightly broader for $x_{\mathrm{Tl}} = [0.7\%, 0.8\%]$ with $\Delta T_c = [25.6\,\mathrm{mK}, 21.2\,\mathrm{mK}]$ respectively. Transition widths ΔT_c are given as $\Delta T_c = T(90\%\rho(1\,\mathrm{K})) - T(10\%\rho(1\,\mathrm{K}))$. The width of the transition generally seems to increase as a function of the doping level even though the highest width is observed for $x_{\mathrm{Tl}} = 0.7\%$. However, this anomaly may be related to another peculiarity found in this sample which will be discussed towards the end of this chapter. Figure 5.14(a) shows the temperature-dependent resistivity of the three superconducting samples normalised to $\rho(1\,\mathrm{K})$ together with the corresponding curve for $x_{\mathrm{Tl}} = 0.4\%$, where no transition was observed down to a sample temperature below 40 mK. Next to this, figure 5.14(b) shows how the superconducting transition temperature rises as a function of Hall carrier density. On first sight the data suggests a superproportional rise of T_c in carrier density, but a linear

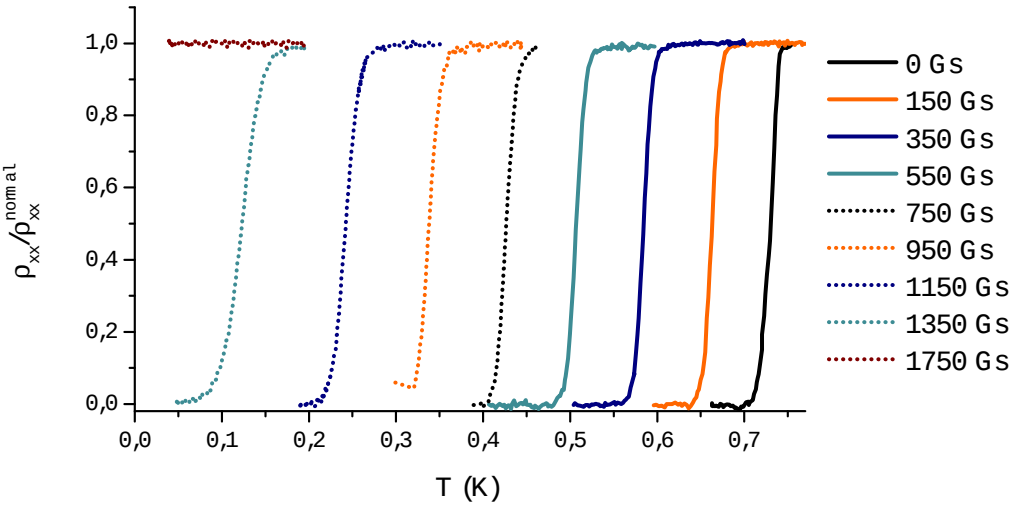

(a) Superconducting transitions in $x_{\mathrm{Tl}} = 0.8\%$.

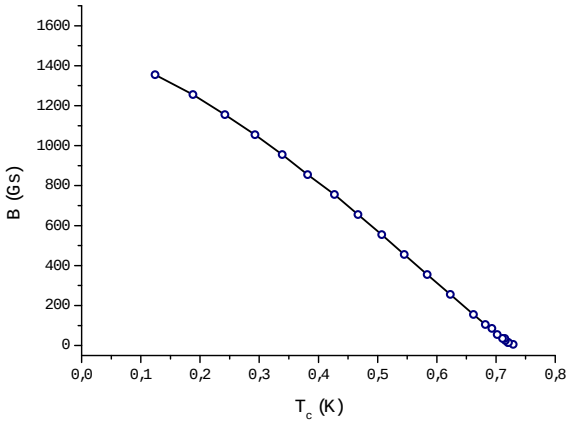

(b) Critical field as a function of transition temperature.

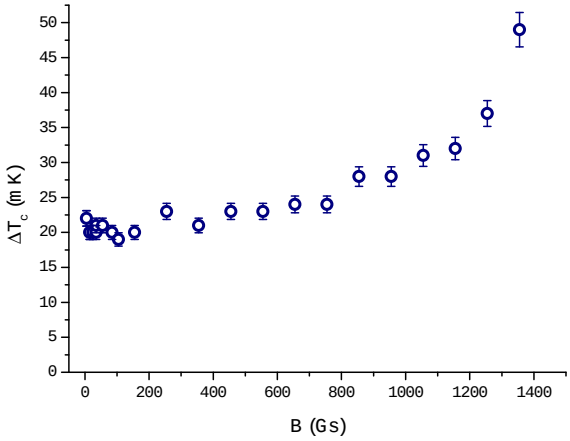

(c) Width of superconducting transition as a function of applied magnetic field.

Figure 5.15.: Field-dependent analysis of the superconducting phase transition for $x_{\mathrm{Tl}} = 0.8\%$.

relation cannot be excluded with this data base due to the low number of available points and the large error bars. With the heuristic extrapolation shown, a cut-off carrier concentration for superconductivity may lie somewhere between carrier densities $40 \cdot 10^{18}\,\mathrm{cm}^{-3}$ and $60 \cdot 10^{18}\,\mathrm{cm}^{-3}$, exactly in the region where the Σ-pockets begin to be populated as discussed in section 5.2, supporting the idea that their appearance is the cradle of superconductivity. The fact that the $x_{\mathrm{Tl}} = 0.4\%$ showed Σ-pockets but did not show a finite T_c within experimental limits is a drop of bitterness on this analysis but no serious threat to the interpretation because of the very large error bars on both Tl-content and Hall number for this sample and the lowest accessible temperature of possibly 40 mK.

A different approach is to analyse the critical temperature directly as a function of Tl-doping. The three data points from this work invite a linear extrapolation into the inaccessible temperature-range, resulting in a cut-off Tl-concentration of about 0.35% as shown in figure 5.14(c). This is in agreement with the much wider study of Matsushita, the result of which is shown in figure 5.14(d). Here, the critical Tl-value for superconductivity is also determined close to x_{Tl} =0.3%. The fact that the disproportionation of thallium seems to start around a similar doping level together with the the linear dependence of the transition temperature on Tl-content has been used as evidence for the charge Kondo-scenario elsewhere [60].

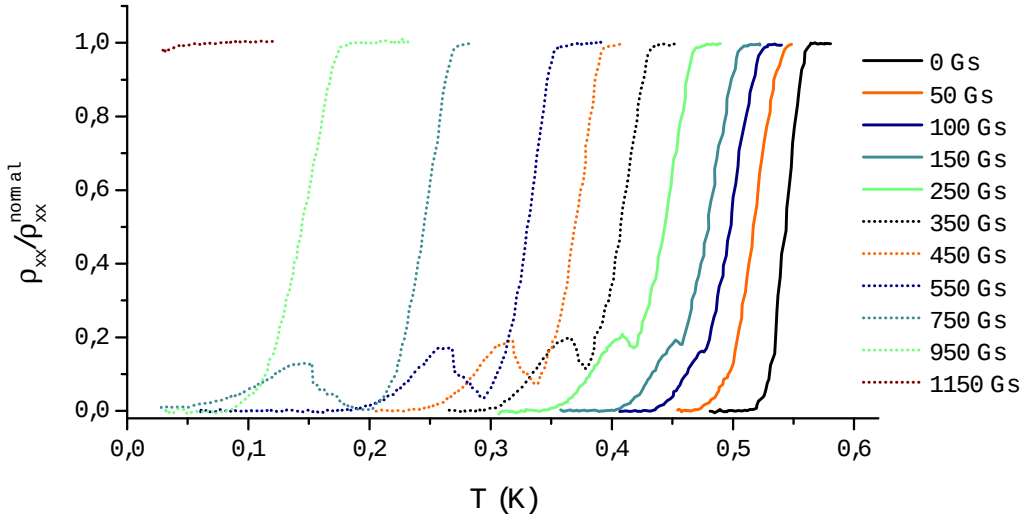

(a) Superconducting transitions in $x_{\mathrm{Tl}} = 0.7\%$.

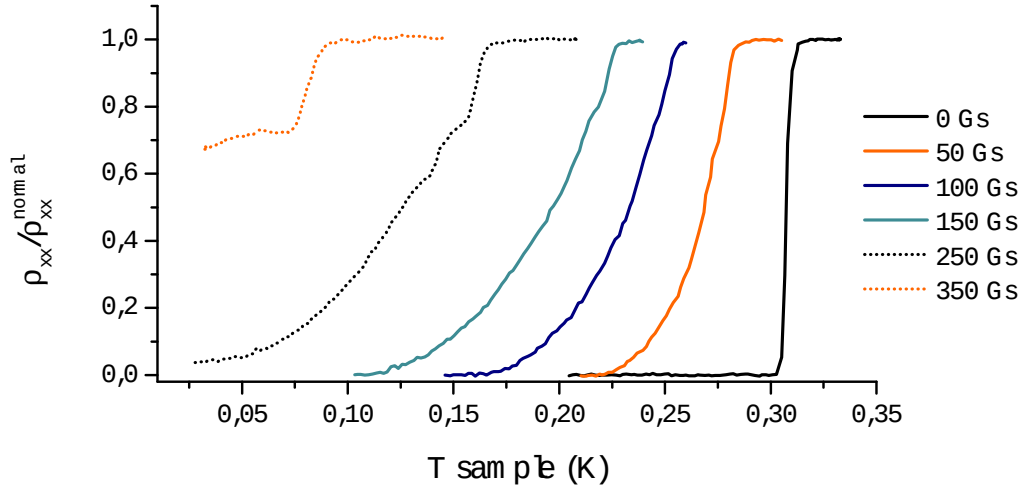

(b) Superconducting transitions in $x_{\mathrm{Tl}} = 0.55\%$.

Figure 5.16.: Re-entrant superconductivity in temperature-sweeps.

In order to characterise the superconducting phase transition further and to get an idea of the electron mean free path, the coherence length and the field penetration depth of the three samples displaying a finite T_c were exposed to a series of weak fields ($B < 2000\,\mathrm{Gs}$) while scanning resistivity as a function of temperature. Figure 5.15 shows the data gained this way for $x_{\mathrm{Tl}} = 0.8\%$ as an example. The phase transition between superconducting and normal state is pushed towards lower temperatures as the applied magnetic field is increased and is suppressed completely by a field of 1750 Gs. The upper critical field $H_{c2}(0)$ can be extracted via an extrapolation of $H_{c2}(T_c)$ to zero temperature, as shown in figure 5.15(b). This procedure yields approximate upper critical fields of $H_{c2}(0) = [400 \pm 50\,\mathrm{Gs}, 1150 \pm 100\,\mathrm{Gs}, 1460 \pm 50\,\mathrm{Gs}]$ for the samples with $x_{\mathrm{Tl}} = [0.55\%, 0.7\%, 0.8\%]$ respectively. As the magnetic field is turned up, the transition in $x_{\mathrm{Tl}} = 0.8\%$ broadens from an initial $\Delta T_c = T(90\%\rho(1\,\mathrm{K}) - 10\%\rho(1\,\mathrm{K})) = 22 \pm 1\,\mathrm{mK}$ to $49 \pm 3\,\mathrm{mK}$ in the last completely observed transition at 1350 Gs.

From the upper critical field and the Fermi velocity v_F the parameters of superconductivity ξ_{GL} and λ_L can be determined as discussed in equations (2.31) and (2.32). The mean free path of an electron is the average distance it travels before being scattered and is hence given as $l = v_F\tau = v_F\mu m_{DOS}/\mathrm{e}$ where $v_F = \sqrt{2E_F/m}$ is the Fermi velocity, τ is the scattering time, μ is the mobility of the carriers and $m_{DOS} = N^{2/3}(m_s m_s m_l)$ is the density of states effective mass for an ellipsoidal case with N equivalent valleys. Here, we are limited to a very rough estimation of these parameters because of our insufficient knowledge about the carriers in the Σ-pockets. In the

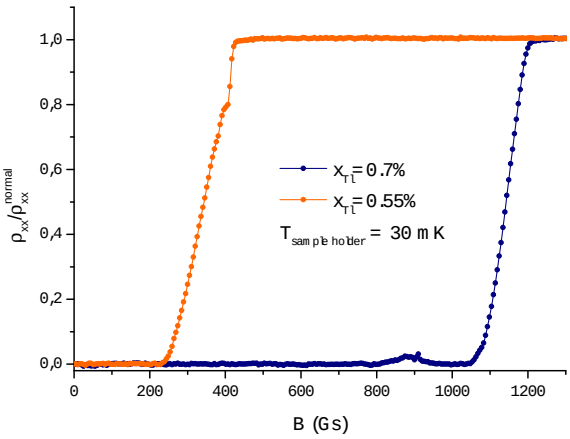

(a) Superconducting transitions at fixed temperature as a function of applied field.

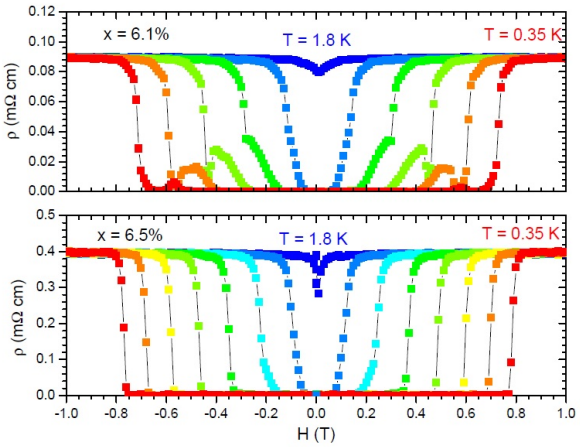

(b) Field-sweeps at fixed temperatures for two samples of In:SnTe with indium-contents of $x_{\mathrm{In}} = 6.1\%$ and $x_{\mathrm{In}} = 6.5\%$ respectively. The upper panel shows re-entrant superconductivity. Figure from reference [70].

Figure 5.17.: Re-entrant superconductivity in field sweeps.

case of the mean free path, it is sufficient to calculate l_L, because in the low temperature limit inelastic scattering from phonons becomes negligible and only elastic scattering processes off impurities remain. This justifies the approximation $l = l_L = l_\Sigma$. Because the Fermi energy E_F and the effective mass m^L_{min} have been observed to saturate around 90 meV and 0.09 m_e respectively in section 5.3, these values can be used for the estimation of the superconducting parameters in $x_{\mathrm{Tl}} = 0.8\%$. Even though the L-pockets are no longer ellipsoidal at this doping-level, it can serve as a first approximation yielding $m_l = \sqrt{13} m_s = \sqrt{13} m^L_{min}$. Using the experimentally estimated mobility of 150 Gs, the resulting mean free path is $l \approx 100$ Å. Calculating the Ginzburg-Landau coherence length from the upper critical field at zero temperature, $H_{c2}(0) = 1460 \pm 50$ Gs results in $\xi_{GL} \approx 500$ Å. Finally, in order to estimate the London penetration depth, some further assumptions have to be made. In a general two-component case, equation (2.31) has to be adjusted to allow for different masses as follows:

$$\frac{1}{\lambda_L^2} = \frac{\mu_0 p_L e^2}{m^L_{DOS}} + \frac{\mu_0 p_\Sigma e^2}{m^\Sigma_{DOS}}. \tag{5.24}$$

Even though not much is known about the mass of the Σ-carriers in Tl:PbTe, one constraint can be extracted from the previous measurements, namely that the maximum mass was observable at 32 T in the $x_{\mathrm{Tl}} = 0.4\%$ sample where the anisotropy was determined to be of the order of $K = 22$. This means that the minimum mass of the Σ-carriers is likely to be smaller rather than larger than the L-mass at that doping because otherwise the observation of oscillations would become very difficult (or else that the relationship between smallest and largest mass is not solely determined by the anisotropy). On the other hand, the Σ-signal was weak, indicating carriers on the edge of the observable range. Overall it is a reasonable assumption to position a Σ-mass guess in the same order of magnitude as the L-mass. As the valley degeneracy of the Σ-pockets is twelve, it is convenient to assume equal density of states masses for the two types of carriers, hereby implicitly making a guess for m^Σ_{min} and the corresponding anisotropy. Additionally, L- and Σ-carriers are estimated to appear in like fractions, justified by figure 5.11. These assumptions result in $\lambda_L \approx 3000$ Å.

All three values are only intended to give an idea of their order of magnitude and cannot be expected to be accurate within more than 50%. However, they allow to characterise superconducting Tl:PbTe: because of $\xi_{GL} < \lambda_L$ it is a type-II superconductor, due to $l < \xi_{GL}$ it is classified to be in the dirty limit. This agrees with what was found elsewhere and also with general expectations for doped semiconductors [32].

While the evolution of the superconducting transitions with increasing outer field in $x_{\mathrm{Tl}} = 0.8\%$ is compliant with the expected behaviour, in the sample with $x_{\mathrm{Tl}} = 0.7\%$ there is a peculiarity to be seen. As the field is turned up, starting from 100 Gs the beforehand smooth transition from normal to superconducting state begins to show a growing substructure. At first, a step-like feature appears on the slope and with higher fields this step moves out of the actual transition and becomes a hump with finite resistivity. In other words, the sample enters the superconducting state at temperature T_c, remains there for a short temperature range and then re-enters the normal state before coming back into the superconducting state, as shown in figure 5.16(a). In the case of $x_{\mathrm{Tl}} = 0.55\%$, although no complete re-entrant behaviour can be observed, this may be due to the experimental window, as the last shown transition in figure 5.16(b) displays a bump as well. Also, the transition width in this sample rises more strongly as a function of field than in the other two samples, possibly due to the re-entrant bump being coated by the principal transition.

To verify that these peculiar effects are not due to a measurement artefact or a hysteresis effect, curves were recorded applying negative fields and also when coming back to low fields after having measured at 2000 Gs. All of them showed the same structures. Additionally, the magnetic field was swept continuously from 0 to 1300 Gs at a fixed temperature of $T < 40$ mK. Just like in the case with fixed field and sweeping temperature, the sample is expected to show normal behaviour above a critical field and the superconducting state once the field is low enough (if the fixed temperature is low enough for a superconducting ground state). However, as the little bump around 900 Gs in figure 5.17(a) shows, the re-entrant behaviour in $x_{\mathrm{Tl}} = 0.7\%$ was also confirmed in this measurement. In $x_{\mathrm{Tl}} = 0.55\%$, a small shoulder sits on the transition as well.

A similar effect has been reported by Erickson [70] in In:SnTe where two different samples with $x_{\mathrm{In}} = 6.1\%$ showed the same re-entrant behaviour into an area of non-zero resistance in experiments with fixed temperatures and sweeping field (figure 5.17(b)). Erickson points out the similarity between this and the “peak-effect” - a field-dependent variation of vortex-pinning strength that has been observed to cause peaked structures in the critical current density in niobium alloys [71]. However, there may be an explanation more specific to systems with valence-skipping dopants such as thallium and indium which surfaces from the charge Kondo model. This will be discussed in chapter 7.

6 Comparison to Theory

In order to compare the findings presented in chapter 5, particularly the Σ-pockets, to theory, new calculations were performed by Alaska Subedi (formerly Collège de France, now Max-Planck-Institut for the Structure and Dynamics of Matter) using density functional theory. As the exact functionals for exchange and correlation are not known in real systems, they have to be approximated. In the most common approximation, the *Linear Density Approximation* (LDA) the functional depends only on the electron density at the coordinate where the functional is evaluated. The *General Gradient Approximation* (GGA) used here refines this procedure by additionally taking the first derivative of the electron density into account. In this calculation, the identity of the dopant does not play any role. Quantities are read of the calculated band structure at different energy values which correspond to a specific number of charge carriers without taking care of their origin. This means that Tl-doping is consequently assumed not to alter the band structure. The lattice parameter used for the calculations is $a = 6.464\,\text{Å}$. The oscillation frequencies given below were extracted from the calculated electronic structure data using the `SKEAF` package [72] of the `WIEN 2k` code.

Figure 6.1 shows a plot of the band structure resulting from Subedi's calculation. It is clear that the first band filling happens at the L-points as it is established both theoretically and experimentally. Of the secondary band maxima at W-, Δ- and Σ-points, the one at Σ is highest in energy and hence becomes filled next. L- and Σ-pockets stem from the same band, the result is hence not a "two-band Fermi surface" but a "two-component Fermi surface". In order to extract Fermi surfaces at different isoelectronic doping levels, the Fermi energy was moved downwards into the valence band of the material and the expected oscillation frequencies and effective masses of the carriers were extracted for each of them. On overview of the numerical data calculated in this way is given in table 6.1. Here, Σ-pockets appear for the first time at a doping of $x_{\text{holes}} = 0.39\%$, remarkably close to the experimentally determined value of $x_{\text{Tl}} = 0.4\%$, keeping in mind that both values may not exactly correspond to the emerging point of the pockets due to the spacing of the available data. Figure 6.2 shows plots of the Fermi surfaces at five different doping levels. At low doping, the L-pockets are ellipsoidal in shape as confirmed experimentally. With increasing doping, they first become more cylindric in shape (also in close agreement with experiment) and start to grow fingers towards the Σ-pockets at still higher carrier concentrations. The latter emerge at $x_{\text{holes}} = 0.39\%$ and grow continuously thereafter. For the example case of $x = 0.52\%$ both minimum and maximum frequencies and the resulting anisotropy K were calculated. $F_{\text{min}} = 19\,\text{T}$ and $F_{\text{max}} = 93\,\text{T}$ result in $K_{\text{theo}} = 24$ which matches the experimentally determined value of $K_{\text{exp}} = 22$ closely. Figures 6.3(a) and 6.3(b) show experimental and theoretical values for oscillation frequencies and masses in combined plots. The agreement between the two sets of Σ-minimum frequencies is quite good whereas the theoretical L-frequencies fall behind experiment by as much as 10 T at the highest doping levels. At lower doping, the agreement is much better. Reasonable overlap is achieved for the effective masses even though there is again a tendency of the calculation to yield lower values than the experiment.

hole doping (%)	p ($10^{18}\,\text{cm}^{-3}$)	F^{L}_{min} (T)	m^{L}_{min} (m_e)	F^{Σ}_{min} (T)	m^{Σ}_{min} (m_e)
0.12	17	33	0.057	0	0
0.23	34	48	0.068	0	0
0.39	57	55	0.073	12	nn
0.52	77	59	0.077	19	0.110
0.63	94	62	0.082	24	0.113
0.74	110	65	0.086	28	0.115
0.86	127	68	0.090	32	nn

Table 6.1.: Overview of the numerical data on PbTe calculated by A. Subedi. Quantities given as "nn" were not available at the time of writing.

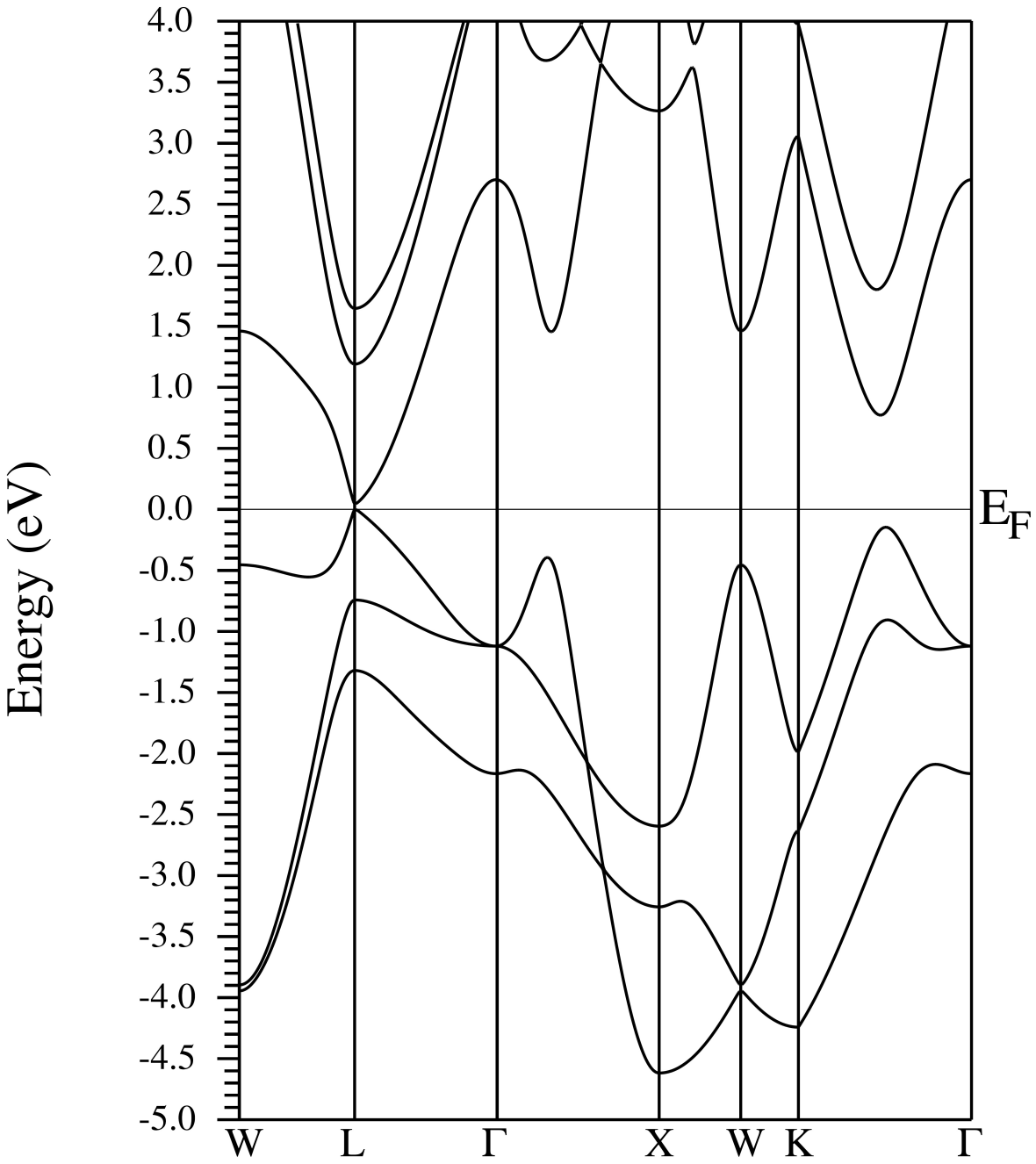

Figure 6.1.: The band-structure of PbTe. The Σ-point is located between K- and Γ-points. When the Fermi energy is lowered into the conduction band, the fist band filling occurs at the L-points, the highest maximum shown above. Upon further doping, the next peak entered is the one at Σ. L- and Σ-peaks sit on the same band which originates from a lead p-orbital. Figure: A. Subedi.

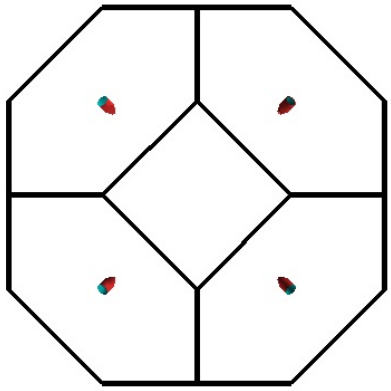

(a) $x = 0.12\%$.

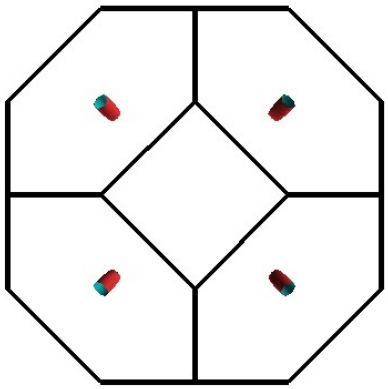

(b) $x = 0.23\%$.

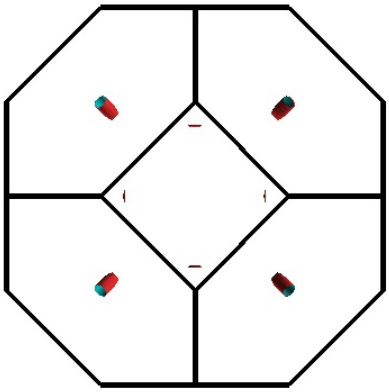

(c) $x = 0.39\%$.

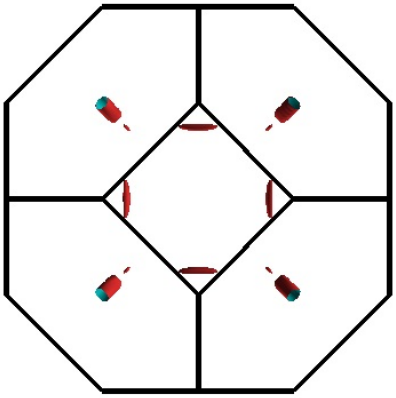

(d) $x = 0.52\%$.

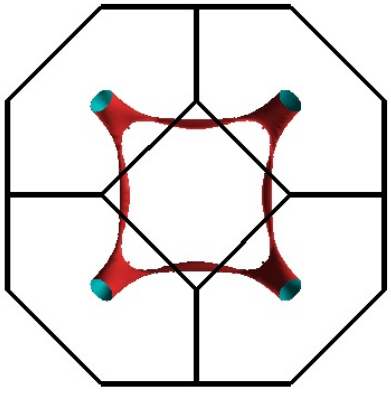

(e) Tube structure at higher doping.

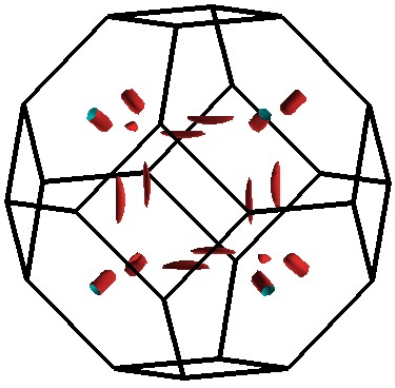

(f) Different perspective on $x = 0.52\%$.

Figure 6.2.: Evolution of the Fermi surface of PbTe between ellipsoidal pockets at low doping and a tubular structure at very high doping. In the four upper panels, a projection of the fcc-Brillouin zone is shown; the last panel visualises the 3D-arrangment of the pockets in the Brillouin-zone for the example of $x = 0.52\%$. For sake of completeness the tubular structure as found before by Singh [43] for even higher doping is shown as well. Figures: A. Subedi.

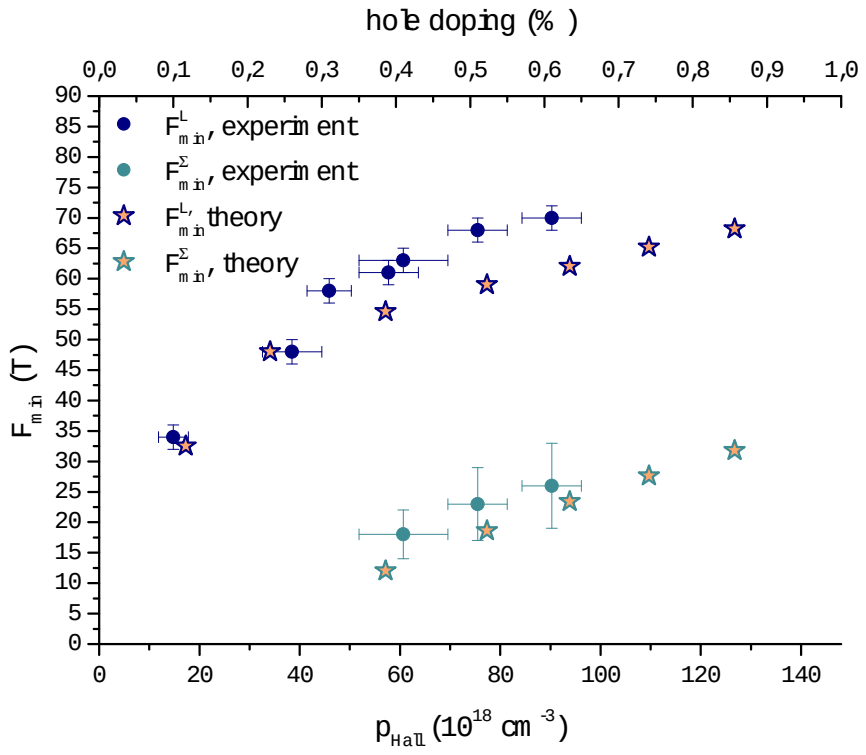

(a) Minimum oscillation frequencies of both pocket sets as a function of hole doping (top axis) and carrier concentration (bottom axis).

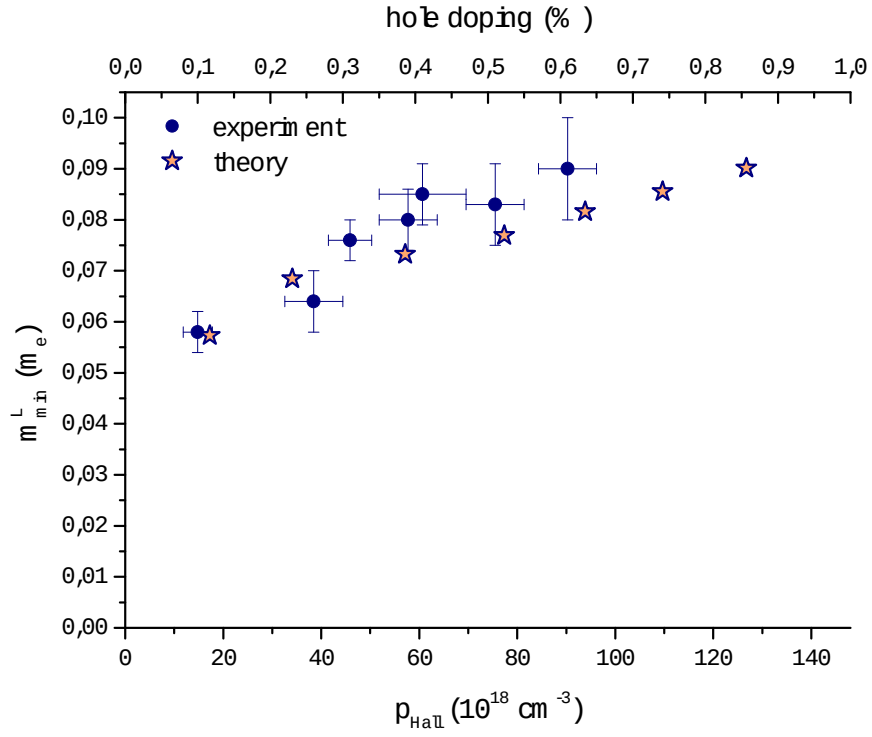

(b) Minimum masses of the L-pocket carriers as a function of hole doping (top axis) and carrier concentration (bottom axis).

Figure 6.3.: Comparison of experimental and theoretical oscillation frequencies and masses. The experimental values (dark blue an turquoise dots) stem from this work, the theoretical values (stars) were calculated by A. Subedi.

7 Discussion

At the heart of this project lies the analysis of the electronic structure of Tl:PbTe in **k**-space by means of quantum oscillations in resistivity. It has long been known [40] that the Fermi surface of p-type lead telluride at carrier concentrations below $10^{19}\mathrm{cm}^{-3}$ consists of four small ellipsoidal pockets at the L-points of its fcc-Brillouin zone, but no experimental advances were made into the higher doping-range because this requires stronger magnetic fields. In this work, samples with higher carrier concentrations were analysed in a high magnetic field facility offering dc fields of up to 32 T. With these experiments, the range in which the ellipsoidal model can be confirmed was slightly extended as a sample with $x_{\mathrm{Tl}} = 0.2\%$ and $p_{\mathrm{Hall}} = 15 \cdot 10^{18}\mathrm{cm}^{-3}$ showed the corresponding signature. More importantly, the confirmation of the ellipsoidal model of pure PbTe in thallium-doped system serves as a cornerstone for the following discussion which is in large parts independent of dopant identity, making no qualitative distinction between samples with carriers from different origins. This first data point shows that the effect that replacing less than one percent of the lead atoms in the crystal with thallium has on the band structure is negligible for our purposes.

Following the evolution of the L-pockets further into the higher doping regime reveals the breakdown of the ellipsoidal Fermi surface model. A sample with $x_{\mathrm{Tl}} = 0.3\%$ and $p_{\mathrm{Hall}} = 46 \cdot 10^{18}\mathrm{cm}^{-3}$ shows a strong deviation from the K=13 ellipsoids and a barrel-model is suggested instead in figure 5.8(d). This model results from the fact that the oscillation frequencies observed in the sample lie above the predictions of the K=13 model, in fact agreeing with a K=60 ellipsoidal model (figure 5.8(c)). The height of the barrel is assumed to equal the length of a K=13 ellipsoid with the same minimum cross section as no discontinuous jumps in the pockets length are to be expected. However, this remains a heuristic assumption because the far ends of the pockets are not accessible to experiment. In reality the pockets' shape may lie in between ellipsoidal and cylindrical form. A K60/13-barrel (where 60 gives the curvature of the pocket and 13 the length) can hold more carriers than a K=13 ellipsoid because of its larger volume. This is in favour of the model because it is clearly shown (5.7(b)) that the K=13 model cannot account for all carriers above $x_{\mathrm{Tl}} = 0.2\%$.

At higher doping still, namely in $x_{\mathrm{Tl}} = 0.4\%$, additional frequencies are observed in the spectra of the quantum oscillation data which cannot be accounted for by the model of four simple pockets at the L-points. These oscillatory branches can be tracked over several orientations of the magnetic field around $\mathbf{B} \parallel [001]$ and agree with calculations for a model of twelve additional ellipsoidal pockets at the Σ-points of the Brillouin zone. The general data quality for $x_{\mathrm{Tl}} \geq 0.4\%$ is poor and the tracking of these branches in more spectra as well as the confirmation of the new feature at higher doping proved difficult. Because of this, the accuracy with which the Σ-carriers could be characterised remains much below the level accessible for the L-carriers. Notably, it was impossible to determine the Σ-carriers' effective masses. General considerations building on the fact that they are observable in the fields applied here suggest that the mass corresponding to the frequencies observed for $\mathbf{B} \parallel [001]$ must be significantly below one electronic mass.

Even though the oscillatory evidence for the Σ-carriers will have to await replication by future experiments, the need for additional pockets is fortified by the comparison of measurements of the Hall coefficient and the number of carriers that L-pockets can hold, even if the barrel-model is applied for $x_{\mathrm{Tl}} \geq 0.3\%$. The growing discrepancy between model and data in figure 5.7(b) shows the necessity of additional Fermi surface components and their effect is displayed in figure 5.11. A combination of modified L-pockets and additional Σ-pockets with the measured minimum frequencies as a base can reproduce the Hall carrier concentration with sufficient accuracy. Taking into account the sound agreement with Subedi's results as discussed in the previous chapter, the emergence of Σ-pockets in the carrier density range of $p_{\mathrm{Hall}} = (50 \pm 15) \cdot 10^{18}\mathrm{cm}^{-3}$ can be established as a reliable fact.

The minimum oscillation frequency and hence the minimum cross section of the L-pockets rises fast as a function of doping-level in the region below $20 \cdot 10^{18}\mathrm{cm}^{-3}$ and considerably slower afterwards as shown in figure 5.7(a), almost going into saturation. This implies that the size of the L-pockets remains almost constant at higher doping as additional carriers are put into the newly emerged set of Σ-pockets. In agreement with this, the effective mass for $\mathbf{B} \parallel [111]$ rises from $0.035\, m_{\mathrm{e}}$ in Burke's lowest-doped sample to about $0.08\, m_{\mathrm{e}}$ at $46 \cdot 10^{18}\mathrm{cm}^{-3}$ but does not increase considerably thereafter. The Fermi energy calculated from minimum frequency and corresponding mass

consequently goes into saturation as well as is shown in figure 5.13(b). At first glance it seems paradoxical that the carrier concentration continues to increase even though the Fermi level hardly moves at all, but at second sight this is a further proof for the existence of Σ-pockets at higher doping levels. Because the filling of the band at the Σ-point is only beginning at the doping-levels analysed here, the curvature of the band at the Fermi energy positions concerned is weak. As shown in figure 6.1, the band peak at Σ has a flat top, thus a minuscule change in Fermi level can induce a large change in carrier concentration. Additionally, the Σ-pockets have a valley degeneracy of twelve in the fcc Brioullin zone, any change in the associated carrier content hence resulting in a three times stronger overall change than for a comparable L-pocket filling. The high number of Σ-valleys combined with the flat top of the band explain why the carrier number estimated to lodge at the Σ-point is already so high (about $20 \cdot 10^{18}\mathrm{cm}^{-3}$) when they are first observed in $x_{\mathrm{Tl}} = 0.4\%$ (see figure 5.11). The new band filling also yields the explanation necessary to account for the discrepancy between the complete stop of carrier increase predicted by theory once the Fermi level is pinned and the continuing rise with doping that is observed experimentally. Even though the Fermi level moves very little, the peculiarity of the Σ-point and -band leads to a continuous carrier number increase. At the same time, the L-pockets become almost frozen objects in **k**-space as they stop growing and remain fixed to a minimum frequency of about 70 T and a minimum mass of about $0.08\, m_e$.

One of the questions asked at the beginning of this project was whether the emergence of a superconducting ground state and the emergence of a second Fermi surface component are related with one another. To answer this, all samples were cooled below 40 mK to look for superconducting transitions. A superconducting ground state was found in $x_{\mathrm{Tl}} = [0.55\%, 0.7\%, 0.8\%]$ with transitions temperatures of $T_c = [307\, mK, 543\, mK, 730\, mK]$ respectively. In $x_{\mathrm{Tl}} = 0.4\%$ no transition was observed. The transition temperatures seem to rise linearly with Tl-content (figure 5.14(c)), but due to the small number of points and the large error bars in both Tl-content and Hall number no definite statement can be made. The three data points taken here might just as well agree with a linear dependency on carrier concentration, though this seems less likely as figure 5.14(b) shows. It is especially important to note that the data collected in this work is not in disagreement with a standard electron-phonon BCS description. Firstly, T_c rises monotonously with carrier concentration once the Σ-pockets are present. Secondly, the emergence of these second pockets may allow for new intra-valley phonons, thereby changing the electron-phonon interaction potential $\tilde{V}_0$ as introduced in equation (2.30). Because of the small size of all Fermi surface elements in the case of PbTe, the inter-band phonons within the L-pockets can only cover a fraction of the phonon dispersion relation close to the Γ-point. A second set of pockets does not only introduce new Σ-inter-valley phonons but also phononic interactions between the two pockets at their different **k**-space positions. A qualitative difference in the superconducting properties of PbTe with L-pockets only and PbTe with two sets of pockets is hence conceivable.

A careful comparison with literature data of SnTe backs the idea of the Σ-pockets being at the root of superconductivity. As figure 7.1(a) shows, there is a sharp onset carrier concentration of about $p = 4 \cdot 10^{20}\mathrm{cm}^{-3}$ for superconductivity in SnTe that seems to be independent of dopant identity. The carrier density dependent evolution of the Fermi surface in SnTe has been analysed by Savage *et al.* and a second band was found in samples with $p > 3.6 \cdot 10^{20}\mathrm{cm}^{-3}$. A similar plot for PbTe containing new data from this work is shown in figure 7.1(b). Just like in SnTe, a second frequency and superconductivity seem to emerge in a very narrow range. As PbTe has not yet been found to exhibit superconductivity with any other dopant, a comparison between different ways of doping is not possible here. The critical carrier concentration for both superconductivity and a second set of pockets is around $p = 50 \cdot 10^{18}\mathrm{cm}^{-3}$ in Tl:PbTe. A possible connection between superconductivity and a second type of carriers has been discussed before by Lewis [23]. He analyses the case of GeTe where there is also a distinct cut-off carrier concentration for superconductivity and compares it to calculations resulting in an emerging second band at a similar carrier density. However, there is no experimental evidence for (or against) the filling of a second band at this value. Lewis relates superconductivity to the new set of pockets only, discussing the possibility that only these heavier carriers assume a superconducting state while the carriers from the first set of pockets remain in the normal state. Nevertheless his evidence agrees with the scenario discussed here (additional phonon modes increasing the electron-phonon interaction potential) as well.

If superconductivity in Tl:PbTe as well as in SnTe can be explained within electron-phonon BCS theory when incorporating the filling of a second set of pockets, this raises the question of the position of the charge Kondo model introduced in section 3.3 in this puzzle. A possible answer is again offered by a look at SnTe. Here, while the cut-off carrier concentration for superconductivity is independent of dopant identity, the actual transition temperatures observed clearly are not. While self-doped as well as As- and Sb-counterdoped systems exhibit transition temper-

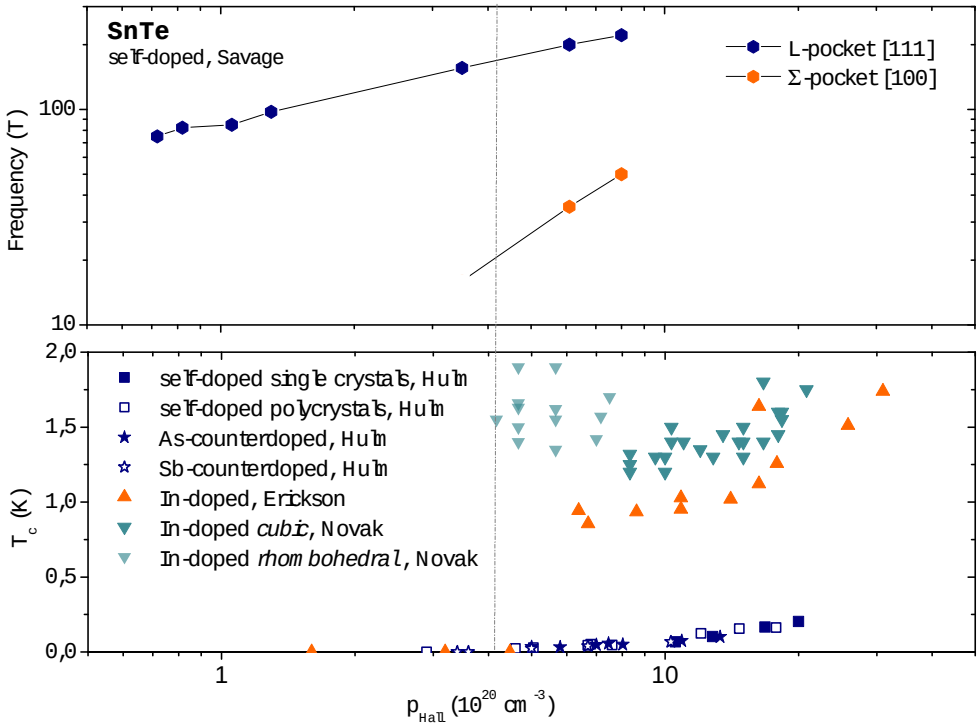

(a) SnTe. Data points are from Savage *et al.* [39], Hulm *et al.* [22], Erickson *et al.* [63] and Novak *et al.* [73].

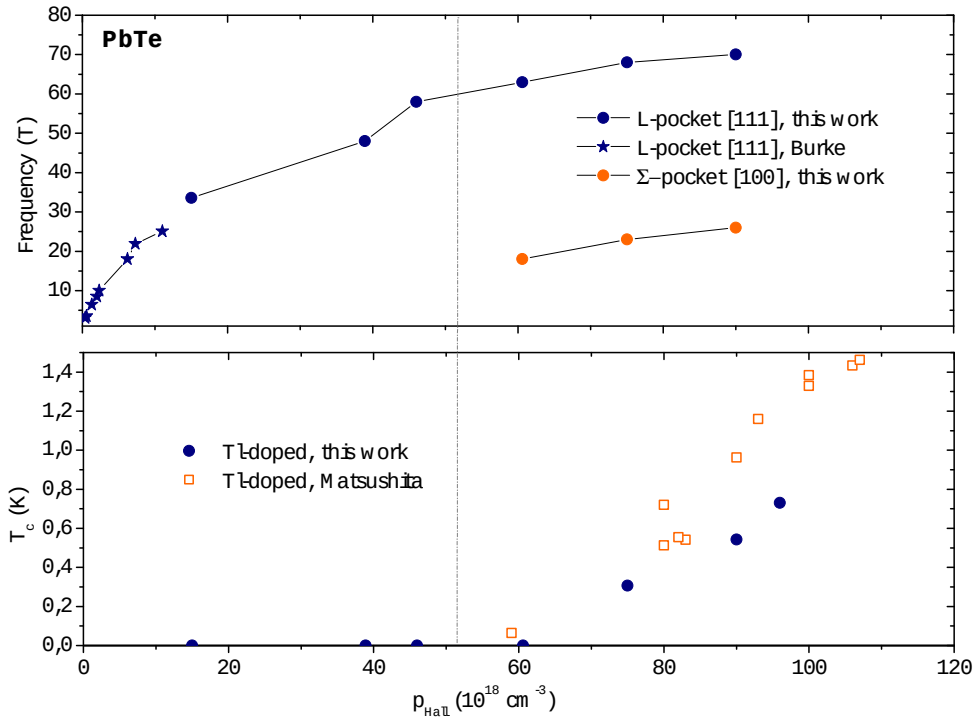

(b) PbTe. Data points are from Burke *et al.* [40], Matsushita [32] and this work.

Figure 7.1.: Minimum oscillation frequencies and transition temperatures as a function of carrier density. Carrier concentration and frequency for SnTe are plotted on a logarithmic scale because of the large ranges covered by the points. The dotted straight lines roughly separate the regimes with one set of pockets (no superconducting ground state) and two sets of pockets (finite T_c).

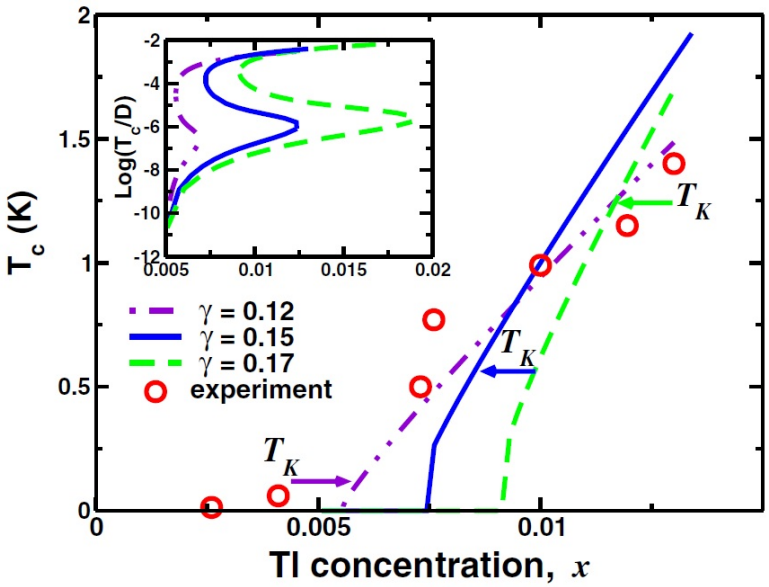

Figure 7.2.: T_c as a function of thallium concentration for different coupling constants γ. Figure from [55].

atures in the range below 200 mK, the T_c values of In:SnTe lie between one and two orders of magnitude higher, reaching peak values of almost 2 K. There is thus a clear difference between indium and other dopants causing so large an effect that it cannot be explained with BCS's standard treatment of atomic differences in the lattice via ω_D (the isotope effect). As indium is a valence-skipping element and In:SnTe has been discussed as a candidate system for charge Kondo physics, it may be the negative U related pairing mechanism that enhances T_c as compared to other SnTe systems with the same carrier concentration. In the case of Tl:PbTe, where the low temperature resistivity upturn described as a signature of the charge Kondo effect has been widely observed in samples with $x_{\mathrm{Tl}} \geq 0.3\%$ in this work as well as elsewhere, Tl may act a T_c enhancer in a similar way. Because the highest transition temperatures observed in the system remain below 1.5 K even in the presence of Tl, the transition temperature in other systems may be extremely low explaining why no superconducting ground state has been observed there up to now.

While phenomena such as the low temperature resistivity upturn shown in figure 5.3 and the deviation of the Hall charge carriers from the expected number shown in figure 5.2 have been associated with the negative U picture, albeit re-entrant superconductivity having been observed in charge Kondo candidate systems (figure 5.17(b)) no connection with charge Kondo physics has been made. However, Schmalian and Dzero [55] discuss re-entrance as a "unique fingerprint for a charge Kondo origin of superconductivity" in their paper on negative U superconductivity using Tl:PbTe as an example case. The result of their calculations is shown in figure 7.2 in the form of a phase diagram. They discuss re-entrance in the field-free case, giving 30 mK as the order of temperature at which the normal state might reappear for $x_{\mathrm{Tl}} = 1\%$ and put it down to the competition between the negative U pairing interaction and the pair breaking being caused by scattering processes including Kondo pseudo-spin flip. As this temperature is extremely low, it may be the reason why the effect has not been observed in the field-free case. No expectations for cases with an applied field are given, but it is conceivable that the competition between pair-bonding and pair-breaking forces in the material is influenced in such a way as to move the re-entrance into the normal state to higher temperatures. While the experimental observation of re-entrant superconductivity may be in agreement with the charge Kondo model, the complete saturation of carrier concentration once the disproportionation of Tl-atoms has begun could not be confirmed here. Instead, the carrier concentration continues to increase at a reduced speed as was found by Matsushita. Here, further theoretical attention would be desirable in order to review which experimental findings can be reconciled with the model and which cannot.

From the database available here it is difficult to make definite statements about whether the Σ-pockets or the presence of two different valence-states needed for the charge Kondo effect is at the root of superconductivity. A significant deviation of the Hall carrier number from the expected carrier concentration for one hole per thallium dopant cannot be observed below $x_{\mathrm{Tl}} = 0.7\%$ because of the large error bars in Tl-content. At the same time, a low-temperature resistivity upturn is detected for x_{Tl} as low as 0.3%, a value where Hall carrier concentration

and expected carrier concentration in figure 5.2 still seem to match. On the other side, Σ-pockets are believed to appear at $x_{Tl} = 0.4\%$ - in a sample where no finite T_c was detected within experimental range. In the light of superconductivity being a collective phenomenon of a large fraction of the carriers in the system, assuming general phononic interactions at the base of the collective state rather than a coupling mechanism introduced by less than one percent of the atomic sites seems the more down-to-earth option. It is clear however that further investigation, both on the experimental and the theoretical side of the question, are needed to settle the problem definitely.

When thinking about constructive experiments to this end, a major issue that appeared in this study needs to be taken into account: the sought-after Fermi surface structures are at the limit of what is observable with quantum oscillations. As a general rule mobility decreases as carrier number increases, but the presence of third party dopants such as thallium complicates this even more. The dc fields used in this work are among the highest available in the world and it is highly debatable whether increasing the applied fields by a few Tesla would significantly help the case. Even if the highest existing dc fields of about 40 T were used, because of the oscillations being periodic in inverse field, this would only add a span of $0.006\,\mathrm{T}^{-1}$ to the data collected here (typically about half an oscillation period of L-pocket type A). Pulsed fields reach values of up to 90 T but the data quality is much impaired due to the high noise and short acquisition times so that collecting quantum oscillations with amplitudes as small those examined in this work may be very difficult. Nevertheless, there are a number of experiments and calculations both in Tl:PbTe and neighbouring materials that would be helpful in corroborating the outcomes discussed above.

First of all it would be very important to confirm superconductivity in PbTe systems without thallium. A good crystalline candidate for this is Na:PbTe because the solubility limit of Na in PbTe allows for carrier concentrations that are as high as those discussed in this work. However, great care should be taken to decrease the temperature into the range of a few mK because the transition temperatures in these materials may lie orders of magnitude below those of Tl:PbTe with the same carrier concentration. Na:PbTe may also be a more convenient candidate for fermiology purposes as the mobility of the carriers has been reported to be higher than in Tl:PbTe [40]. If superconductivity was confirmed in Na:PbTe, this would be a sharp test for two of the questions discussed above: firstly, if a similar threshold value was found, the crucial dependency of superconductivity on the second set of pockets could be established more firmly. Secondly, the actual transition temperature would contain the answer to the question whether thallium enhances T_c in the same way that indium raises the transition temperature of SnTe. In a complementary approach, one could search for superconductivity in PbTe thin films because here it is possible to reach much higher carrier concentrations than in the bulk without adding third party dopants. In Tl:PbTe, the transition temperatures of single crystals and thin films has been shown to be very similar [32].

Experiments that can be performed on the existing Tl:PbTe samples used in this work include returning to high field facilities with a set-up adjusted to the quest by employing a ^{3}He-system or even a dilution refrigerator in order to reach lower temperatures. If the mass of the Σ-carriers is larger than that of the L-carriers, this could help to make their signature stronger as the signal from heavier carriers is reduced faster with rising temperatures. It would be a definite proof of a second set of pockets if one of the frequency peaks attributed to them in this work could be found to display a Lifshitz-Kosevich temperature dependence. Further experiments during a second magnet time at high fields should include more samples around the critical concentration of $x_{Tl} = 0.4\%$ (because the mobility in samples with much higher thallium concentration is to low for precise results at the available fields) as well as a finer angle-spacing in the region of $\mathbf{B} \parallel [001]$ were the pockets were observed in this work.

A different possible experimental approach would be thermoelectric measurements on Tl:PbTe. In the topological insulator candidate Bi_2Se_3 strong quantum oscillations were observed in the Nernst effect, the thermoelectric equivalent of the Hall effect [74]. It is possible that thermoelectric effects are a more sensitive Fermi surface probe in PbTe as well, hence making more of the available magnetic fields. However, the extremely small size of the available samples together with the difficulties of reaching low contact resistances on them poses a challenge for thermoelectric experiments.

On the theoretical side of things there are two different questions that could be tackled. For one thing, using the same functional as for PbTe, the Fermi surface evolution of SnTe could be analysed. If Σ-pockets appear at a carrier concentration of $p \approx 4 \cdot 10^{20}\mathrm{cm}^{-3}$, the cut-off concentration for a superconducting ground state as shown in figure 7.1(a), this would further strengthen the suggested key role for superconductivity. Secondly, the change of the electron-phonon-interaction potential $\tilde{V}_0$ with the emergence of a second set of pockets at different $\mathbf{k}$-space

positions should be analysed in order to look into whether it is strong enough to bring about a superconducting state.

Once the Σ-pockets are firmly established as the cradle of superconductivity in PbTe and SnTe, this information gained in systems whose Fermi surface is easily tuned as a function of carrier concentration, can be applied to other systems with more complex Fermi surface topologies. Their electronic systems may contain substructures similar to the two sets of pockets discussed here but the effects of these elements cannot experimentally be separated from those of others. The study of the simpler systems PbTe and SnTe as presented and summarised in this work hence serves as a magnifying glass on the more complex systems, singling out one component for detailed analysis. It is in a similar context that the study of the charge Kondo effect in Tl:PbTe has to be classified. The existence of such an effect is not yet a commonly acknowledged fact and it has hence not surpassed the state of being analysed for its own sake. There are however suggestions that charge Kondo related phenomena play a role in high-T_c cuprates [75]. Once their effects are completely understood, the controlled use of valence-skipping elements in the prediction and synthesis of new superconductors may become possible.

A Matlab-Scripts

Those Matlab-codes potentially useful to anyone working on this or a similar project in the future are given in this section.

A.1 Fourier-Transformation

The following is the function used to Fourier transform the oscillation data. This version of the function builds on a code by Paula Giraldo-Gallo.

```
function FFTresult=FFT(oscillations,Bmin) %array 'oscillations' must contain
    %B in the first column and the oscillation data without background in
    %the second, Bmin is the smallest field value at which oscillations are
    %observable

oscillations(:,1)=1./oscillations(:,1); % inverts field column


[sizey,sizex]=size(oscillations);

array=[];
for i=1:1:sizey  %data below the specified minimum field is cut off
    if oscillations(i,1)<=1/Bmin
        array=[array; oscillations(i,1) oscillations(i,2)];
    end
end


minfieldtot=min(array(:,1));
maxfieldtot=max(array(:,1));

xi=transpose(minfieldtot:(maxfieldtot-minfieldtot)/(sizey*10):maxfieldtot);
    %produces equally spaced 1/B column, factor 10 serves to smooth output
[x1p, idxp]=unique(array(:,1));
yi1=interp1(array(idxp,1),array(idxp,2),xi); %interpolates data over this 1/B range

array=[];
array(:,1)=xi;
array(:,2)=yi1;


[sizey,sizex]=size(array);
fs=1/(array(2,1)-array(1,1)); % reads sampling frequency from prepared data

win=hann(sizey); % specifies window
xw = win(:).*array(:,2); % applies window to data

NFFT = 2^nextpow2(sizey*100); %chooses closest power of 2 to increase
    %algorithm efficiency, factor 100 smooths output

fftarray=fft(xw,NFFT); %discrete Fourier transformation

f = (fs/2)*linspace(0,1,NFFT/2+1); % generates new x-axis in frequency
    %domain with correct spacing

FFTresult(:,1)=f; %assigns x-axis to output
FFTresult(:,2)=2*abs(fftarray(1:NFFT/2+1)); %assigns single-sided amplitude
    %spectrum to output
```

A.2 Frequencies in the Ellipsoidal model

The following code allows to plot the expected oscillation frequencies as a function of θ in the ellipsoidal case. The first half of the code plots the lines for the ideal case, in the second part the misalignment parameters as introduced in section 5.1 can be specified as well.

```
%% basic parameters of ellipsoids

 Fmin=60;    % minimum frequency for L ellipsoids
 K=13;       % K for L ellipsoids

 Fmin2=18;   % minimum frequency fro \Sigma ellipsoids
 K2=22;      % K for \Sigma ellipsoids

 x=-12:1:105; %angle range

%% F(\theta) lines for K-ellipsoidal pockets at L and \Sigma with major
%axes along [111] and [100] respectively

% functions for L ellipsoid types A, B, C
fA=Fmin*sqrt(1./(cosd(acosd((sqrt(2)*sind(x)+cosd(x))/sqrt(3))).^2+1/K*...
    sind(acosd((sqrt(2)*sind(x)+cosd(x))/sqrt(3))).^2));
fB=Fmin*sqrt(1./(cosd(acosd((-sqrt(2)*sind(x)+cosd(x))/sqrt(3))).^2+1/K*...
    sind(acosd((-sqrt(2)*sind(x)+cosd(x))/sqrt(3))).^2));
fC=Fmin*sqrt(1./(cosd(acosd(cosd(x)/sqrt(3))).^2+1/K*...
    sind(acosd(cosd(x)/sqrt(3))).^2));

% funcions for \Sigma ellipsoid types 1 and 2
fS1=Fmin2*sqrt(1./(cosd(acosd(sind((x)./sqrt(2)))).^2+1/K2*...
    sind(acosd(sind((x)./sqrt(2)))).^2));
fS2=Fmin2*sqrt(1./(cosd(x).^2+1/K2*sind(x).^2));

% plot
figure
hold('on')
plot(x,fC,'g')
plot(x,fA,'r')
plot(x,fB,'b')
plot(x,fS1,'k')
plot(x,fS2,'m')


%% misalignment

% misalignment parameters as explained in main text
eoff=1;
e1=-6;
e2=2;

% functions for L ellipsoid types A, B, C1, C2
fAerr=Fmin*sqrt(1./(cosd(acosd((sqrt(2)*sind(x+eoff)*cosd(e1)+cosd(x+eoff)*...
    cosd(e2))./(sqrt(3).*sqrt(sind(x+eoff).^2+cosd(x+eoff).^2.*sind(e2)^2-...
    2.*sind(x+eoff).*cosd(x+eoff).*sind(e2).*sind(e1)+cosd(x+eoff).^2.*...
    cosd(e2).^2)))).^2+1/K*sind(acosd((sqrt(2)*sind(x+eoff)*cosd(e1)+...
    cosd(x+eoff)*cosd(e2))./(sqrt(3).*sqrt(sind(x+eoff).^2+cosd(x+eoff).^2.*...
    sind(e2)^2-2.*sind(x+eoff).*cosd(x+eoff).*sind(e2).*sind(e1)+cosd(x+eoff).^2.*...
    cosd(e2).^2)))).^2));
fBerr=Fmin*sqrt(1./(cosd(acosd((-sqrt(2)*sind(x+eoff)*cosd(e1)+cosd(x+eoff)*...
    cosd(e2))./(sqrt(3).*sqrt(sind(x+eoff).^2+cosd(x+eoff).^2.*sind(e2)^2-2.*...
    sind(x+eoff).*cosd(x+eoff).*sind(e2).*sind(e1)+cosd(x+eoff).^2.*...
    cosd(e2).^2)))).^2+1/K*sind(acosd((-sqrt(2)*sind(x+eoff)*cosd(e1)+...
    cosd(x+eoff)*cosd(e2))./(sqrt(3).*sqrt(sind(x+eoff).^2+cosd(x+eoff).^2.*...
    sind(e2)^2-2.*sind(x+eoff).*cosd(x+eoff).*sind(e2).*sind(e1)+cosd(x+eoff).^2.*...
    cosd(e2).^2)))).^2));
fC1err=Fmin*sqrt(1./(cosd(acosd((-sqrt(2).*sind(x+eoff).*sind(e1)+sqrt(2).*...
```

```
    cosd(x+eoff).*sind(e2)+cosd(x+eoff).*cosd(e2)).^2)./(sqrt(3).*sqrt(sind(x+eoff).^2+...
    cosd(x+eoff).^2.*sind(e2)^2-2.*sind(x+eoff).*cosd(x+eoff).*sind(e2).*sind(e1)+...
    cosd(x+eoff).^2.*cosd(e2).^2)))).^2+1/K*sind(acosd((-sqrt(2).*sind(x+eoff).*...
    sind(e1)+sqrt(2).*cosd(x+eoff).*sind(e2)+cosd(x+eoff).*cosd(e2)).^2)./(sqrt(3).*...
    sqrt(sind(x+eoff).^2+cosd(x+eoff).^2.*sind(e2)^2-2.*sind(x+eoff).*cosd(x+eoff).*...
    sind(e2).*sind(e1)+cosd(x+eoff).^2.*cosd(e2).^2)))).^2));
fC2err=Fmin*sqrt(1./(cosd(acosd((+sqrt(2).*sind(x+eoff).*sind(e1)-sqrt(2).*...
    cosd(x+eoff).*sind(e2)+cosd(x+eoff).*cosd(e2)).^2)./(sqrt(3).*sqrt(sind(x+eoff).^2+...
    cosd(x+eoff).^2.*sind(e2)^2-2.*sind(x+eoff).*cosd(x+eoff).*sind(e2).*sind(e1)+...
    cosd(x+eoff).^2.*cosd(e2).^2)))).^2+1/K*sind(acosd((+sqrt(2).*sind(x+eoff).*...
    sind(e1)-sqrt(2).*cosd(x+eoff).*sind(e2)+cosd(x+eoff).*cosd(e2)).^2)./(sqrt(3).*...
    sqrt(sind(x+eoff).^2+cosd(x+eoff).^2.*sind(e2)^2-2.*sind(x+eoff).*cosd(x+eoff).*...
    sind(e2).*sind(e1)+cosd(x+eoff).^2.*cosd(e2).^2)))).^2));

% functions for \Sigma ellipsoid types 1, 2, 3
fS1err=Fmin2*sqrt(1./(cosd(acosd(sind(x+eoff).*cosd(45+e1)+cosd(x+eoff).*...
    sind(e2)./sqrt(2))).^2+1/K2*sind(acosd(sind(x+eoff).*cosd(45+e1)+cosd(x+eoff).*...
    sind(e2)./sqrt(2))).^2));
fS2err=Fmin2*sqrt(1./(cosd(acosd(sind(x+eoff).*cosd(45-e1)-cosd(x+eoff).*...
    sind(e2)./sqrt(2))).^2+1/K2*sind(acosd(sind(x+eoff).*cosd(45-e1)-cosd(x+eoff).*...
    sind(e2)./sqrt(2))).^2));
fS3err=Fmin2*sqrt(1./(cosd(acosd(cosd(x+eoff).*cosd(e2))).^2+1/K2*...
    sind(acosd(cosd(x+eoff).*cosd(e2))).^2));

% plot
figure
hold('on')
plot(x,fAerr,'Color',[1 0.4 0],'linestyle','-')
plot(x,fBerr,'Color',[0 0 0.5])
plot(x,fC1err,'Color',[0.235 0.549 0.576])
plot(x,fC2err,'Color',[0.235 0.549 0.576],'linestyle','--')
plot(x,fS1err,'Color',[0 0 0],'linestyle','-')
plot(x,fS2err,'Color',[0.35 0.35 0.35],'linestyle','-')
plot(x,fS3err,'Color',[0.65 0.65 0.65],'linestyle','-')

legend('L-pocket A', 'L-pocket B', 'L-pocket C1', 'L-pocket C2',...
    '\Sigma-pocket [100]','\Sigma-pocket [010]','\Sigma-pocket [001]')
ylabel('frequency (T)');
xlabel('angle (deg)');
ylim([0 180])
```

B Additional figures

This chapter contains data not explicitly shown in the main part but used for the derivation of quantities given therein.

B.1 High-field quantum oscillation colourmaps

This chapter includes all colourmaps produced from measurements at the HFML in Nijmegen. As introduced in chapter 5, they are a 3D representation of SdH spectra. Inverse magnetic field is plotted over field angle θ, the colour scale shows the resistivity value after background substraction as explained in section 2.1. The scaling is chosen such that the red end of the spectrum corresponds to the highest peak in $\Delta\rho$ while the blue end corresponds to the lowest trough. These colourmaps are interpolated, but the actual angle-resolution is poorer than in the colourmaps shown in the main text and measured in PPMS. The angle-spacing is 5° for $x_{\mathrm{Tl}} = [0.3\%, 0.4\%, 0.55\%]$ and 7° for $x_{\mathrm{Tl}} = [0.2\%, 0.7\%]$.
The series of figures shows how the decreasing mobility reduces the number of visible oscillations for all angles and how the signature of the B- and C-pockets vanishes earlier with higher doping level. In the first sample, the signature of the A-pockets around $\mathbf{B} \parallel [111]$ is split in two due to the splitting of each Landau level into a spin-up and a spin-down half. This effect scales with magnetic field and hence only becomes visible in the HFML data.

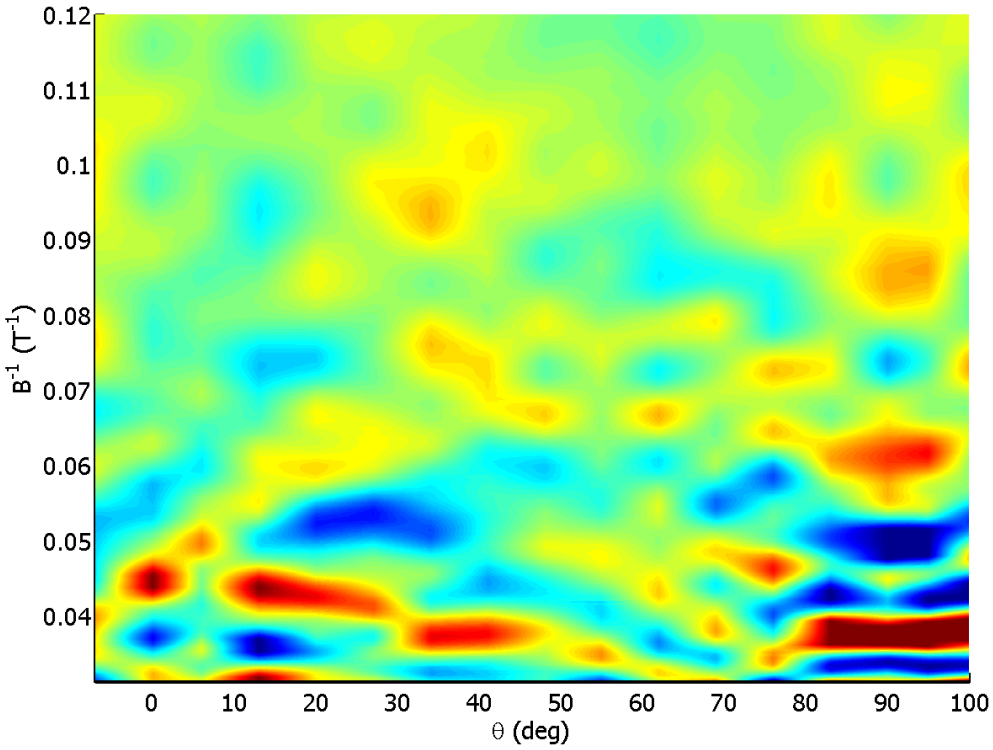

Figure B.1.: $x_{\mathrm{Tl}} = 0.2\%$

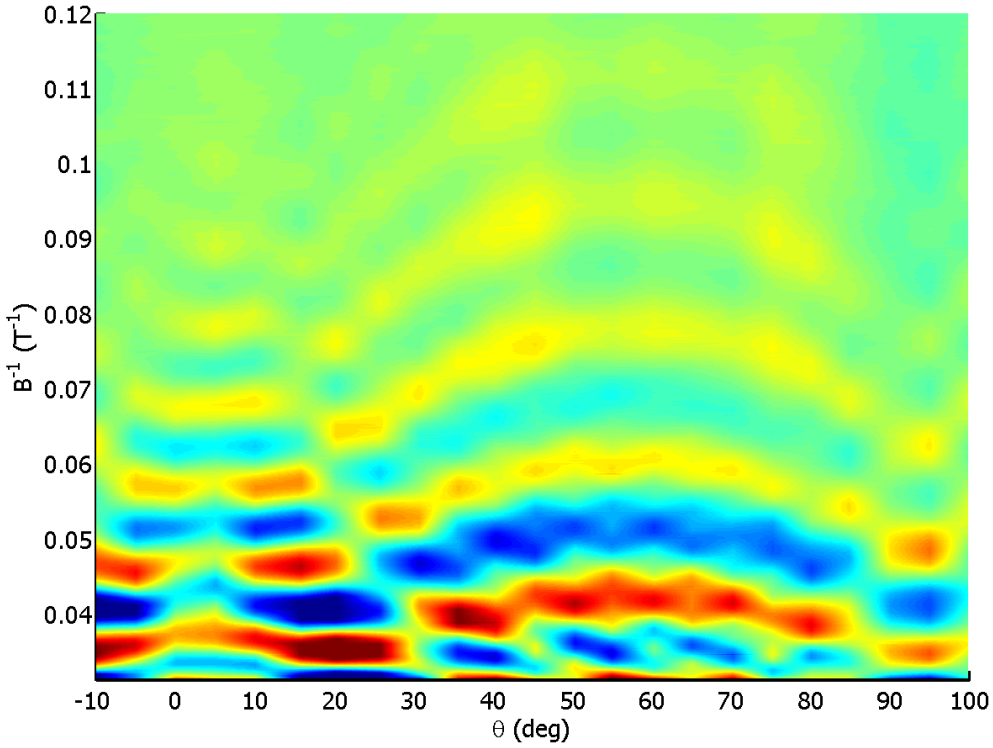

Figure B.2.: $x_{\mathrm{Tl}} = 0.3\%$

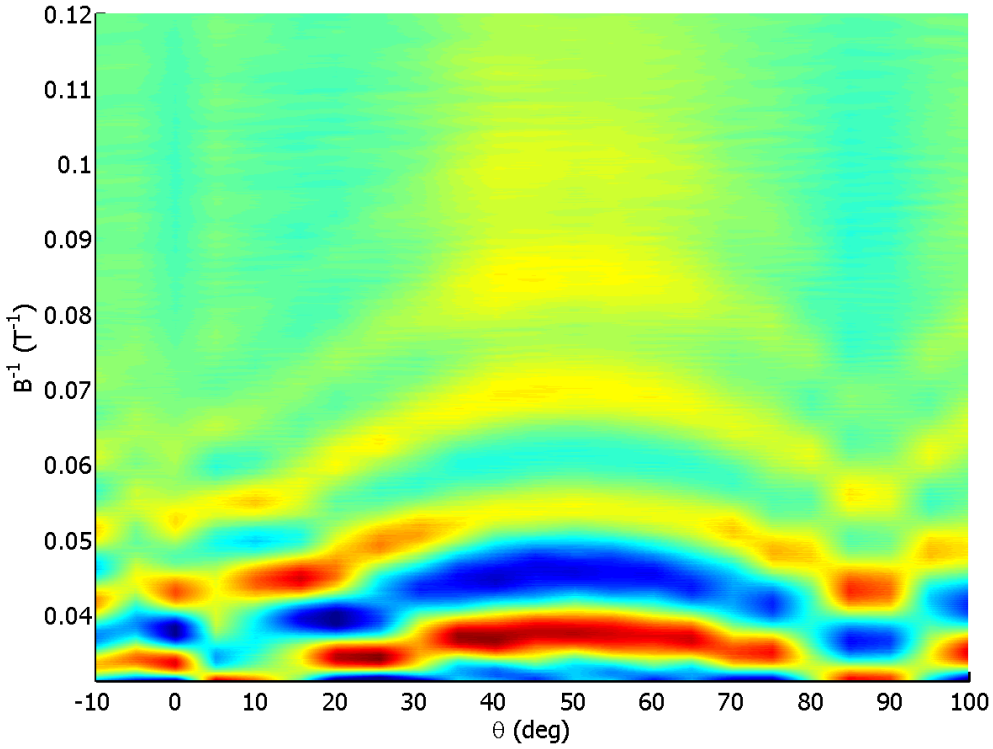

Figure B.3.: $x_{\mathrm{Tl}} = 0.4\%$

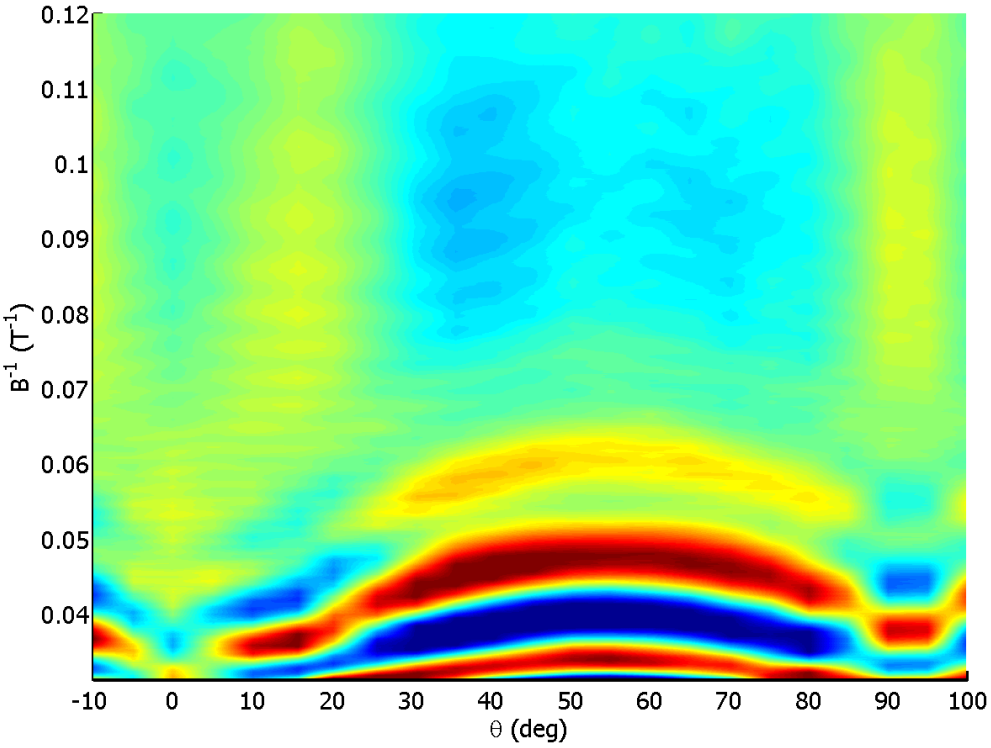

Figure B.4.: $x_{\mathrm{Tl}} = 0.55\%$

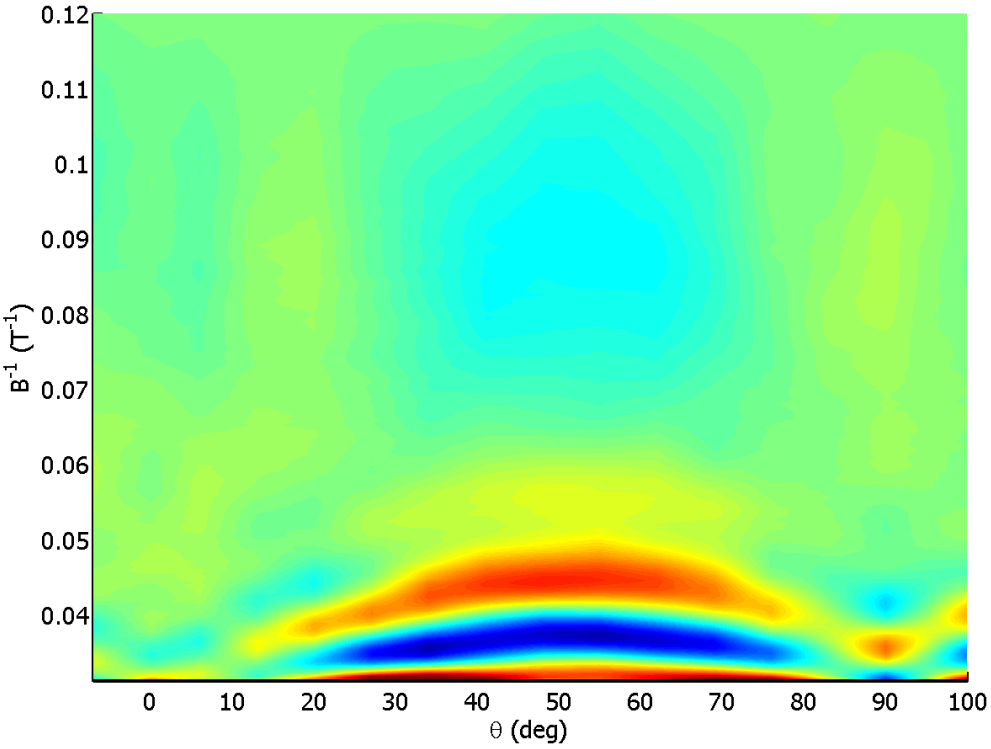

Figure B.5.: $x_{\mathrm{Tl}} = 0.7\%$

B.2 Mass determination

The following pages show temperature-dependent oscillations of **B** ∥ [111] for all samples analysed and the corresponding Lifshitz-Kosevich fits for extracting the effective mass of the L-carriers. The measurements on $x_{\mathrm{Tl}} = [0.2\%, 0.25\%, 0.3\%, 0.35\%]$ were performed in PPMS, the measurements on $x_{\mathrm{Tl}} = [0.4\%, 0.55\%, 0.7\%]$ at the HFML. For $x_{\mathrm{Tl}} = [0.25\%, 0.3\%, 0.3\%]$ the peak height of a chosen peak at fixed field was used for the fit, for $x_{\mathrm{Tl}} = [0.2\%, 0.4\%, 0.55\%, 0.7\%]$ the procedure of taking the difference between consecutive peaks and troughs as described in section 5.3 was employed.

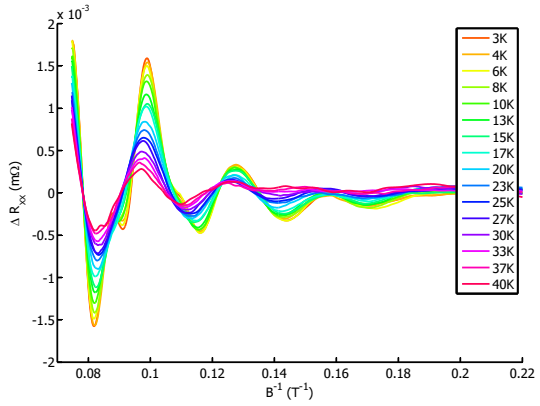

(a) $x_{\mathrm{Tl}} = 0.2\%$.

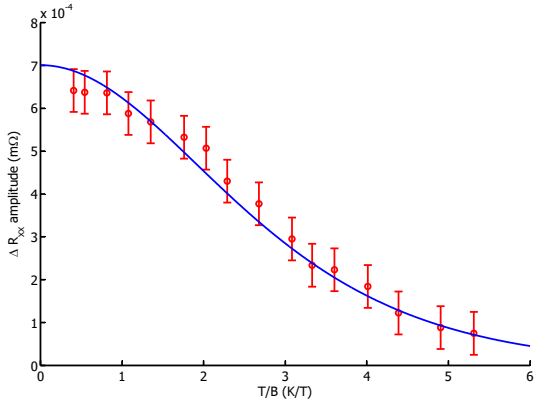

(b) $m^\star = (0.058 \pm 0.004) m_e$.

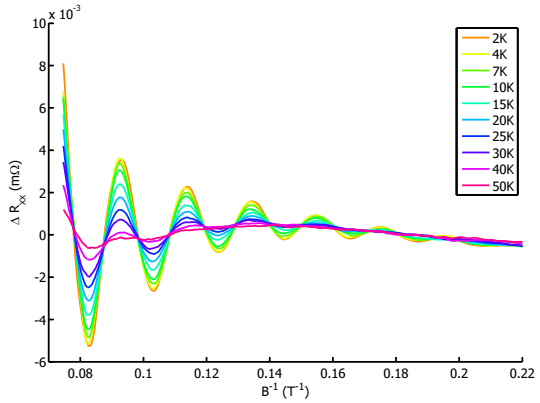

(c) $x_{\mathrm{Tl}} = 0.25\%$.

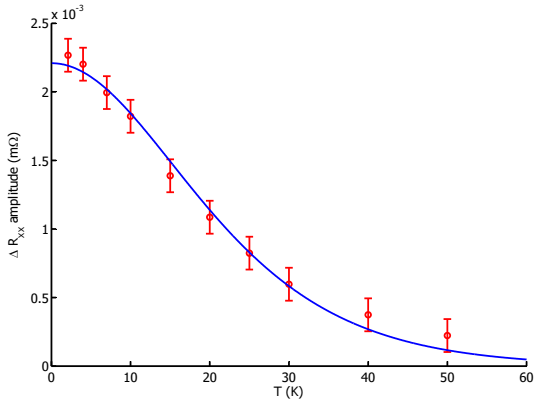

(d) $m^\star = (0.064 \pm 0.006) m_e$.

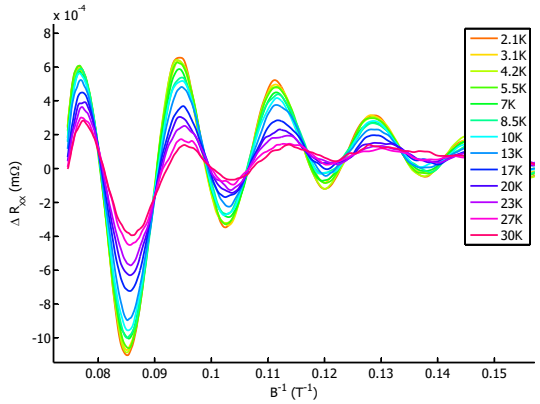

(e) $x_{\mathrm{Tl}} = 0.3\%$.

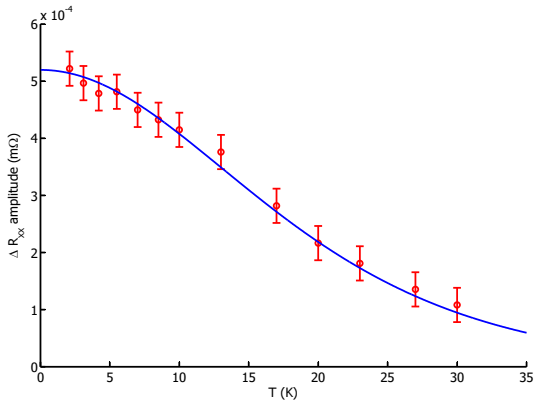

(f) $m^\star = (0.076 \pm 0.004) m_e$.

Figure B.6.: Mass evaluation for **B** ∥ [111] in $x_{\mathrm{Tl}} = [0.2\%, 0.25\%, 0.3\%]$.

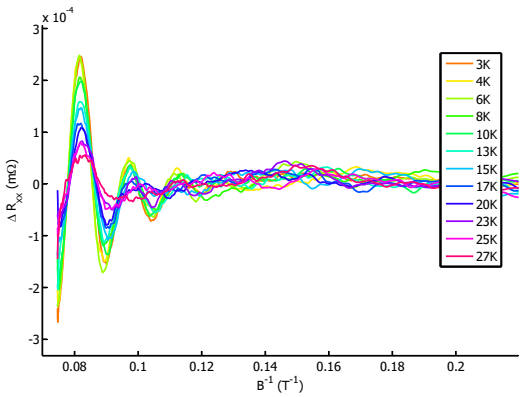

(a) $x_{\mathrm{Tl}} = 0.35\%$.

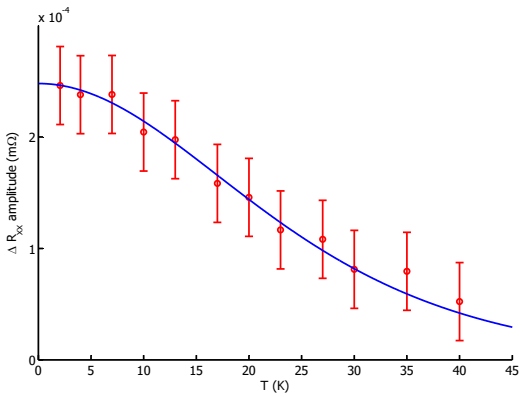

(b) $m^{\star} = (0.080 \pm 0.006) m_{\mathrm{e}}$.

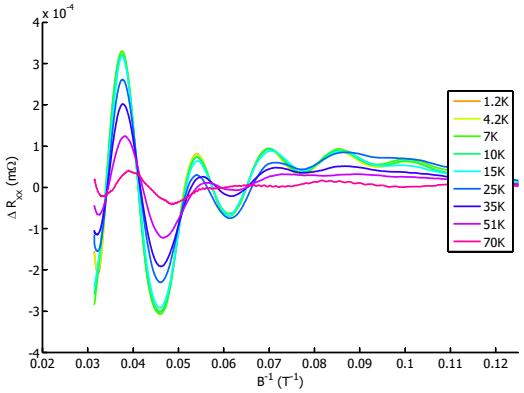

(c) $x_{\mathrm{Tl}} = 0.4\%$.

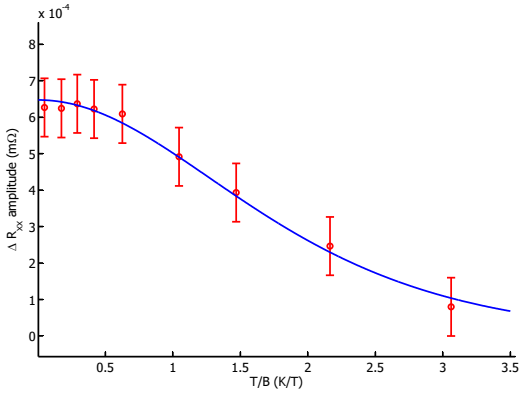

(d) $m^{\star} = (0.085 \pm 0.006) m_{\mathrm{e}}$.

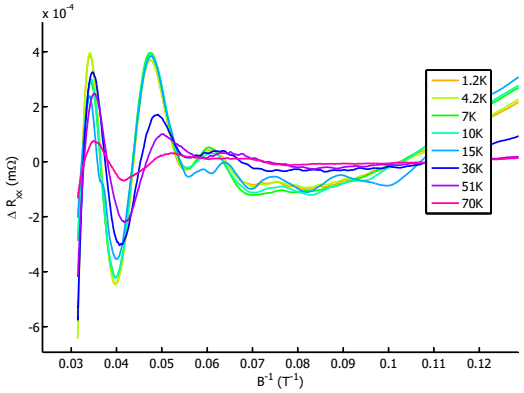

(e) $x_{\mathrm{Tl}} = 0.55\%$.

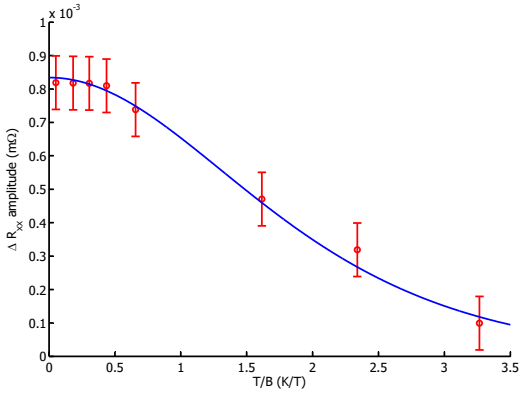

(f) $m^{\star} = (0.083 \pm 0.008) m_{\mathrm{e}}$.

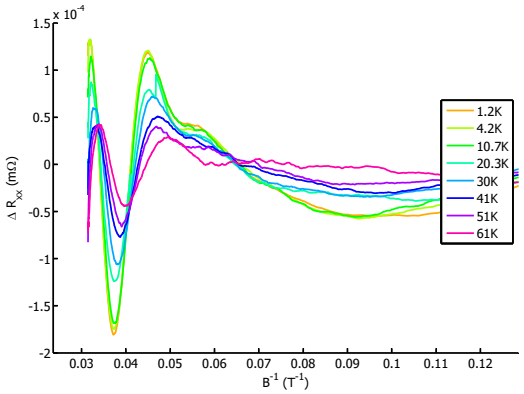

(g) $x_{\mathrm{Tl}} = 0.7\%$.

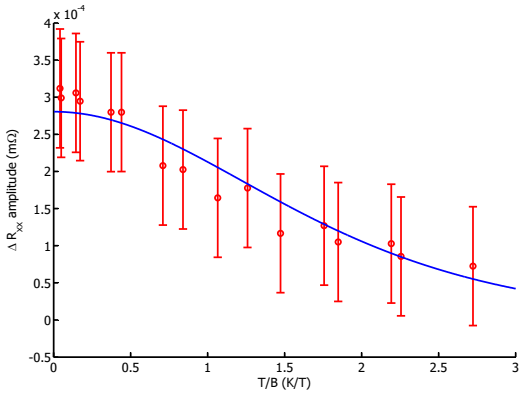

(h) $m^{\star} = (0.09 \pm 0.01) m_{\mathrm{e}}$.

Figure B.7.: Mass evaluation for $\mathbf{B} \parallel [111]$ in $x_{\mathrm{Tl}} = [0.35\%, 0.4\%, 0.55\%, 0.7\%]$.

Bibliography

[1] H. Kamerlingh Onnes. Further experiments with liquid helium. C. On the change of electric resistance of pure metals at very low temperatures etc. IV. The resistance of pure mercury at helium temperatures. *KNAW, Proceedings* **13 II**, 1274 (1911).

[2] H. Kamerlingh Onnes. Further experiments with liquid helium. H. On the electrical resistance of pure metals etc. (continued). VIII. The sudden disappearance of the ordinary resistance of tin, and the super-conductive state of lead. *Comm. Physical Lab. Leiden Suppl.* **133**, 51 (1913).

[3] W. Meissner, H. Franz. Messungen mit Hilfe von flüssigen Helium. VIII. Supraleitfähigkeit von Niobium. *Physikalisch-Technische Reichsanstalt, Mitteilung* **559-559** (1930).

[4] W. de Haas, E. van Aubel, J. Voogd. A superconductor consisting of two non-superconductors. *Akademie der Wetenschappen, Amsterdam, Proceedings* **32**, 730 (1929).

[5] W. Meissner. Messungen mit Hilfe von flüssigem Helium. V. Supraleitfähigkeit von Kupfersulfid. *Physikalisch-Technische Reichsanstalt, Mitteilung* **571** (1929).

[6] F. London, H. London. The electromagnetic equations of the supraconductor. *Proc. R. Soc. A, London* **149**, 71 (1935).

[7] V. L. Ginzburg, L. Landau. On the theory of superconductivity. *Zhurnal Eksperimental'noi I Teoreticheskoi Fiziki* **20**, 1064 (1950).

[8] J. Bobroff, F. Bouquet. http://www.supraconductivite.fr (2010).

[9] H. Kamerlingh Onnes. Report on the researches made in the Leiden cryogenics laboratory between the second and third international congress of refrigeration: Superconductivity. *Comm. Physical Lab. Leiden Suppl.* **34**, 55 (1913).

[10] G. B. Yntema. Superconducting winding for electromagnets. *Phys. Rev.* **98**, 74 (1955).

[11] J. R. Gavaler. Superconductivity in Nb–Ge films above 22 K. *Applied Physics Letters* **23**, 480 (1973).

[12] G. Bednorz, A. Müller. Possible high Tc superconductivity in the Ba-La-Cu system. *Z. Phys. B* **64**, 189 (1986).

[13] K. M. Wu, *et al.*. Superconductivity at 93 K in a new mixed-phase Y-Ba-Cu-O compound system at ambient pressure. *Phys. Rev. Lett.* **58**, 908 (1987).

[14] A. Schilling, M. Cantoni, J. D. Guo, H. R. Ott. Superconductivity above 130 K in the Hg-Ba-Ca-Cu-O system. *nature* **363**, 56 (1993).

[15] A. J. Leggett. What DO we know about high T_c. *nature physics* **2**, 134 (2006).

[16] S. L. Bud'ko, *et al.*. Boron Isotope Effect in Superconducting MgB_2. *Phys. Rev. Lett.* **86**, 1877 (2001).

[17] T. Yoshida, M. Hashimoto, I. M. Vishik, Z.-X. Shen, A. Fujimori. Pseudogap, Superconducting Gap, and Fermi Arc in High-Tc Cuprates Revealed by Angle-Resolved Photoemission Spectroscopy. *Journal of the Physical Society of Japan* **81**, 011006 (2012).

[18] K. M. Shen, J. C. D. Davis. Cuprate high-T_c superconductors. *materialstoday* **11**, 14 (2008).

[19] M. R. Norman. Fermi-surface reconstruction and the origin of high-temperature superconductivity. *Physics* **3** (2010).

[20] N. Doiron-Leyraud, *et al.*. Quantum oscillations and the Fermi surface in an underdoped high-T_c superconductor. *nature physics* **2**, 134 (2006).

[21] N. Doiron-Leyraud. The Fermi surface of cuprate superconductors. *La Physique au Canada* **67**, 89 (2011).

[22] J. Hulm, J. C.K.. Superconducting Interactions in Tin Telluride. *Physical Review* **169**, 388 (1969).

[23] J. E. Lewis. Heavy Holes and Superconductivity in GeTe and SnTe. *phys. stat. sol.* **42**, K97 (1970).

[24] S. Hunklinger. *Festkörperphysik* (Oldenbourg, München, 2007).

[25] W. J. de Haas, P. van Alphen. The dependence of the susceptibility of diamagnetic metals upon the field. *Proc. Netherlands Roy. Acad. Sci.* **35**, 1106 (1930).

[26] L. Schubnikow, W. J. de Haas. A New Phenomenon in the Change of Resistance in a Magnetic Field of Single Crystals of Bismuth. *Nature* **126**, 500 (1930).

[27] L. Landau. Diamagnetismus der Metalle. *Zeitschrift für Physik* **64**, 629 (1930).

[28] D. Shoenberg. *Magnetic oscillations in metals* (Cambridge University Press, Cambridge, 1984).

[29] J. Sólyom, A. Piróth. *Fundamentals of the Physics of Solids: Volume II: Electronic Properties*. Fundamentals of the Physics of Solids (Springer, Heidelberg, 2008).

[30] L. N. Cooper. Bound Electron Pairs in a Degenerate Fermi Gas. *Phys. Rev.* **104**, 1189 (1956).

[31] J. Bardeen, L. N. Cooper, J. R. Schriefer. Microscopic Theory of Superconductivity. *Phys. Rev.* **106**, 162 (1957).

[32] Y. Matsushita. Superconductivity and Mixed Valency in Thallium-Doped Lead Telluride. Ph.D. thesis. Stanford University (2007).

[33] A. LaLonde, Y. Pei, H. Wang, G. Snyder. Lead telluride alloy thermodynamics. *materialstoday* **14**, 526 (2011).

[34] J. Heremans, *et al.*. Enhancement of Thermoelectric Efficiency in PbTe by Distortion of the Electronic Density of States. *Science* **321**, 554 (2008).

[35] R. Allgeier. Magnetoresistance in PbS, PbSe and PbTe at 295°, 77.4° and 4.2° K. *Physical Review* **112**, 828 (1958).

[36] P. J. Stiles, E. Burstein, D. Langenberg. de Haas - van Alphen effect in p-type PbTe and n-type PbS. *Supplement to Journal of Applied Physics* **32**, 2174 (1961).

[37] J. Dimmock, G. Wright. Band Edge Structure of PbS, PbSe, and PbTe. *Physical Review* **135**, A821 (1964).

[38] J. Jochim. Die Messung der Temperaturabhängigkeit des Shubnikov-de Haas-Effektes am Bleiselenid zur Bestimmung der Absolutwerte der effektiven Masse. Master's thesis. Technische Universität Berlin (1975).

[39] R. Burke, B. Houston, H. Savage. Anisotropy of the Fermi Surface of p-type PbTe. *Physical Review B* **2**, 1977 (1972).

[40] J. Jensen, B. Houston, J. Burke. Fermi-surface parameters of p-type PbTe as a function of carrier density. *Physical Review B* **18**, 5567 (1978).

[41] O. Madelung, U. Rössler, M. Schulz, eds.. *Non-Tetrahedrally Bonded Elements and Binary Compounds I*. vol. 41C of *Landolt-Börnstein - Group III Condensed Matter* (Springer Berlin Heidelberg, 1998).

[42] Y. W. Tung, M. L. Cohen. Relativistic Band Structure and Electronic Properties of SnTe, GeTe, and PbTe. *Physical Review* **180**, 823 (1969).

[43] D. Singh. Doping-dependant thermopower of PbTe from Boltzmann transport calculations. *Physical Review B* **81**, 195217 (2010).

[44] H. Sitter, K. Lischka, H. Heinrich. Structure of the second valence band in PbTe. *Physical Review B* **16**, 680 (1977).

[45] K. Nakayama, T. Sato, T. Takahashi, H. Murakami. Doping Induced Evolution of Fermi Surface in Low Carrier Superconductor Tl-Doped PbTe. *Physical Review Letters* **100**, 227004 (2008).

[46] R. S. Allgaier, B. B. Houston. Hall Coefficient Behavior and the Second Valence Band in Lead Telluride. *Journal of Applied Physics* **37**, 302 (1966).

[47] J. R. Dixon, H. R. Riedl. Electric-Susceptibility Hole Mass of Lead Telluride. *Phys. Rev.* **138**, A873 (1965).

[48] K. Ueno, *et al.*. Discovery of superconductivity in $KTaO_3$ by electrostatic carrier doping. *Nature Nanotechnology* **6**, 408 (2011).

[49] X. Lin, Z. Zhu, B. Fauqué, K. Behnia. Fermi Surface of the Most Dilute Superconductor. *Physical Review X* **3**, 021002 (2013).

[50] Y. Takada. Theory of Superconductivity in Polar Semiconductors and its Application to N-type Semiconducting $SrTiO_3$. *J. Phys. Soc. Jpn.* **49**, 1267 (1980).

[51] J. Appel. Soft-Mode Superconductivity in $SrTiO_{3-x}$. *Physysical Review* **180**, 508 (1969).

[52] X. Lin, *et al.*. Critical dopings for the Onset of a Two-Band Superconducting Ground State in $SrTiO_{3-\delta}$. *Physical Review Letters* **112**, 207002 (2014).

[53] C. M. Varma. Missing valence states, diamagnetic insulators, and superconductors. *Phys. Rev. Lett.* **61**, 2713 (1988).

[54] P. W. Anderson. Model for the Electronic Structure of Amorphous Semiconductors. *Phys. Rev. Lett.* **34**, 953 (1975).

[55] M. Dzero, J. Schmalian. Superconductivity in Charge Kondo Systems. *Physical Review Letters* **94**, 157003 (2005).

[56] H. Murakami, W. Hattori, Y. a. A. R. Mizomata. Tunneling observation of Tl quasi-localized impurity states in superconductive semiconductor Pb(Tl)Te. *Physica C* **273**, 41 (1996).

[57] J. Kondo. Resistance Minimum in Dilute Magnetic Alloys. *Progress of Theoretical Physics* **32**, 37 (1964).

[58] W. de Haas, J. de Boer, G. van den Berg. The electrical resistance of gold, copper and lead at low temperatures. *Physica* **1**, 1115 (1934).

[59] T. A. Costi, V. Zlatić. Charge Kondo Anomalies in PbTe Doped with Tl Impurities. *Phys. Rev. Lett.* **108**, 036402 (2012).

[60] Y. Matsushita, H. Bluhm, T. Geballe, I. Fisher. Evidence for Charge Kondo Effect in Superconducting Tl-doped PbTe. *Physical Review Letters* **94**, 157002 (2005).

[61] H. T. Savage, B. Houston, J. R. Burke. Fermi-Surface Studies in SnTe. *Phys. Rev. B* **6**, 2292 (1972).

[62] P. Littlewood, *et al.*. Band Structure of SnTe Studied by Photoemission Spectroscopy. *Physical Review Letters* **105**, 086404 (2010).

[63] A. S. Erickson, J.-H. Chu, M. F. Toney, T. H. Geballe, I. R. Fisher. Enhanced superconducting pairing interaction in indium-doped tin telluride. *Phys. Rev. B* **79**, 024520 (2009).

[64] A. S. Erickson, T. H. Geballe, I. R. Fisher, Y. Q. Wu, M. J. Kramer. Anomalous scattering in superconducting indium-doped tin telluride. *arXiv:1009.0090* (2010).

[65] Y. Matsushita, P. Wianecki, A. Sommer, T. Geballe, I. Fisher. Type II superconducting parameters of Tl-doped PbTe determined from heat capacity and electronic transport measurements. *Physical Review B* **74**, 134512 (2006).

[66] D. L. Mitchell, R. F. Wallis. Theoretical Energy-Band Parameters for the Lead Salts. *Phys. Rev.* **151**, 581 (1966).

[67] M. H. Cohen. Energy Bands in the Bismuth Structure. I. A Nonellipsoidal Model for Electrons in Bi. *Phys. Rev.* **121**, 387 (1961).

[68] E. O. Kane. Band structure of indium antimonide. *Journal of Physics and Chemistry of Solids* **1**, 249 (1957).

[69] I. A. Chernik, S. N. Lykov. *Sov. Phys. Solid State* **23**, 1724 (1981).

[70] A. Erickson. Pairing Mechanisms in Superconductors with Valence-Skipping Dopants. Ph.D. thesis. Stanford University (2009).

[71] W. A. Fietz, W. W. Webb. Hysteresis in Superconducting Alloys—Temperature and Field Dependence of Dislocation Pinning in Niobium Alloys. *Phys. Rev.* **178**, 657 (1969).

[72] P. Rourke, S. Julian. Numerical extraction of de Haas–van Alphen frequencies from calculated band energies. *Computer Physics Communications* **183**, 324 (2012).

[73] M. Novak, S. Sasaki, M. Kriener, K. Segawa, Y. Ando. Unusual nature of fully gapped superconductivity in In-doped SnTe. *Physical Review B* **88**, 140502(R) (2013).

[74] B. Fauqué, *et al.*. Magnetothermoelectric properties of Bi_2Se_3. *Physical Review B* **87**, 035133 (2013).

[75] T. Geballe, B. Y. Moyzhes. Qualitative understanding of the highest Tc cuprates. *Physica C: Superconductivity* **341–348, Part 3**, 1821 (2000).

Thank you - Merci - Danke

I thank Kamran Behnia for giving me the opportunity to come to Paris and for always sharing his scientific and personal wisdom with me. I thank Benoît Fauqué for letting me profit from his sound understanding of Physics and his steady optimism. I thank Aurélie Collaudin for countless detailed explanations on French culture, politics, society, people and bureaucracy and support when dealing with the latter. I thank Benoît and Aurélie for always talking to me in their mother tongue and Kamran for opening his library to me. All this has done a great deal to improve my French. I thank Xiao Lin for teaching me a little bit of patience and precision in experiment and for his own patience in doing so.

I thank Rudolf Feile for his disinterested support of this project and for the straightforward and pleasant communication during its course.

I thank Ian Fisher and Paula Giraldo-Gallo for generously letting me take part in their project on Tl:PbTe. I especially thank Paula for growing the samples and for coming to Europe for a very enjoyable measurement campaign in Nijmegen. I also thank her for inspiring me to travel to her country, Colombia. Also, even tough we do not know each other, I wish to thank Yana Matsushita whose excellent PhD thesis on Tl:PbTe has served as my bible these past twelve months.

I thank Steffen Wiedmann for incredible technical and mental support during our measurements at the HFML.

I thank Alaska Subedi for sound calculations, the patience of a saint when explaining rudimentary bits of theory to me and for letting me use his results and beautiful figures in this work.

I thank Yuki Fuseya and his group for interesting exchanges on PbTe and for letting me catch glimpses of fascinating Japanese culture and the high-contrast megacity that is Tokyo.

I thank Benoît Fauqué, Axelle Girard, Christian Graf, Thomas Hugle, Alexis Jouan, Gianna Marschmann and Malte Probst for help with proofreading this thesis and the preceding project proposal.

Finally, I thank the Studienstiftung des Deutschen Volkes for the financial support during the majority of my studies and especially this last year in one of the world's most expensive cities.

Erklärung

Hiermit versichere ich, die vorliegende Arbeit ohne Hilfe Dritter nur mit den angegebenen Quellen und Hilfsmitteln angefertigt zu haben. Alle Stellen, die aus Quellen entnommen wurden, sind als solche kenntlich gemacht. Diese Arbeit hat in gleicher oder ähnlicher Form noch keiner Prüfungsbehörde vorgelegen.

Declaration

This work is a presentation of my original research. Wherever contributions of others are involved, this is indicated clearly. This work has not been presented to any examination authority before, neither in this nor in a similar form.

Darmstadt, 24^{th} of September 2014

Lisa Franziska Buchauer